UNIVERSITÀ
DEGLI STUDI
FIRENZE

PhD in Atomic and Molecular Photonics

CYCLE XXXVI

COORDINATOR Prof. Diederik S. Wiersma

Liquid crystalline networks: from reactive mesogen design to the development of artificial muscles and micrometric actuators

ACADEMIC DISCIPLINE (SSD) CHIM/04

Doctoral Candidate

Simone Donato

Supervisor

Prof. Camilla Parmeggiani

Co-Supervisor

Dr. Daniele Martella

Daniele Martella

Coordinator

Prof. Diederik S. Wiersma

Years 2020-2023

Abstract

Soft smart materials like Liquid Crystalline Networks (LCNs) attracted the attention of the scientific community for application in many fields, such as tissue engineering, robotics, and encryption. Indeed, their properties and response to stimuli can be tailored for the need of each specific application by a molecular approach, namely the copolymerization of different reactive monomers. In LCNs, for example, modulation of the phase behaviour of the mesogenic molecules is commonly addressed by structural modification at molecular level. Starting from a rigid rod-like core (containing 2 or more aromatic rings), reduction of molecular symmetry by increasing the steric hindrance with different substituents generally favours nematic phases instead of smectic ones and reduces the clearing temperature. The use of different reactive mesogens is also a powerful tool to adjust the polymer performances in terms of force development under stimulation, kinetics of actuation, elasticity, and resistance to specific loads. The first part of this study deals with the preparation of photo-responsive Liquid Crystalline Networks (LCNs) by acrylate photopolymerization, exploiting crosslinker modification at molecular level, towards the development of light-responsive artificial muscles. Mechanical properties and maximum tension developed under light actuation were deeply characterised to mimic the function of natural muscles. Furthermore, kinetics of activation and relaxation can be modulated and implemented, leading to a material able to produce optimised tensions and response kinetics. In the second part of the research Two-Photon Direct Laser Writing (TP-DLW) has been exploited for the fabrication of shape-changing LCN microstructures to be exploited in stimuli responsive microrobotics and photonics. These 3D micro-structures can contract anisotropically, along a specific direction in response to stimuli, such as temperature or light. Also in this case, the use of different reactive mesogens has been explored for the optimization of the responsive behaviour of the microstructures. We demonstrated the fabrication of free-standing microstructures as graphical units of a couvert tag for simple physical and optical encryption using an array of identical LCN pixels. Information can be hidden to the observer and revealed only upon application for a specific stimulus thanks to a specific shape-change of each pixel. Once the stimulus is removed and the pixels recover their original shape the message remains completely hidden. This achievement can be considered an opto-mechanical equivalent of an “invisible ink” and paves the way for introducing enhanced functionalities in micro-optomechanical systems within a single lithography step, spanning from storage devices with physical encryption to complex motion actuators.

Preface and objectives

Since the last century the study of new materials has proven to be crucial for human needs and the use of smart materials has attracted the attention of the whole scientific world. The first definition of smart material was given by Takagi [1], who defined them as "intelligent", or materials capable of reacting to external stimuli by changing one of their properties significantly. From this definition, in recent years, a great number of smart materials have been reported in the scientific literature, capable of responding to different types of activation (heat, light, chemical reactions, electric and magnetic fields, etc.) and performing different types of tasks. [2,3] The fields of applications of the smart materials are many, starting from actuators, opto-mechanical devices, biomedical engineering, anti-counterfeiting, robotics to aerospace applications. In particular, the class of soft actuators is one of the most promising for tissue engineering applications, such as for the development of artificial muscles.

Due to the possible tuning of the mechanical properties through a structural modification of the mechanical properties, these materials are compatible with biological tissues leading to significant advantages in their use, if compared with hard smart materials. In addition, this class of polymers or soft materials offer a new model of object manipulation allowed by the continuous modification and adaptability of deformation that is possible to be controlled by external and remote stimulus. This consideration moved the scientific community also to explore the miniaturisation of these materials and their possible application in the field of soft robotics or micrometric photonic devices.[4] Among smart materials, Liquid Crystalline Networks (LCNs) are one of the most promising. The main reason is their ability to transform their molecular motion, when triggered with a stimulus, into a large mechanical deformation. First theorised by De Gennes [5] in 1975 and defined as possible artificial muscles by Finkelmann in 2001[6], these materials turn out to be in between the best candidates to produce artificial cardiac muscles to replace or assist mechanically compromised hearth muscles. This is the goal of the European REPAIR Project, composed of 10 units in Europe. The project tackles many challenges in chemistry, fundamental for the preparation of photo-responsive materials mimicking biological muscle activity, as well as in physics and engineering of the processes involved. In the second part of the thesis, LCNs have been explored for micrometric actuations and the realisation of a micro-smart-tag for message encryption. This field of application assumes particular interest in recent decades due to the advent of increasingly advanced technologies for storing and protecting sensitive data. The miniaturisation of the LCNs was performed by Two-Photon Direct Laser Writing, a lithographic technique based on point-by-point polymerization induced by absorption of two photons in the focus of the laser beam. Only in this volume, a small voxel (volume pixel) is polymerized with sub-diffraction limited resolution. This project was conducted at Trinity College of Dublin and Ireland's Amber Institute of Science for the realisation of the handled materials.

The main objectives of this thesis can be summarised in:

1. Study how the introduction of sterically hindered crosslinkers can influence the chemical and physical properties and force development under illumination of the fabricated LCNs. This will be addressed in **Chapter 2** through the synthesis of new mesogenic crosslinkers that have been employed for LCNs preparation. In **Chapter 3**, the characterization of their light-responsiveness is reported.

2. Verify how the crosslinker amount (prepared in point 1) should influence the force development under light irradiation and the kinetic behaviour of the LCNs. This will be tackled in **Chapter 3** based on the results obtained in **Chapter 2**.

3. Study the possibility to 3D print microstructures starting from the new LCN mixtures and the effect of different molecular parameters (such as type of crosslinker and its amount) on the shape-changing behaviour. This will be addressed in **Chapter 4**.

4. Application of shape-changing microstructures (prepared in point 3) for the realisation of a responsive label capable of containing hidden information and revealing it upon certain stimuli. This application expands the use of LCN microstructures already described in our research group in the field of robotics and photonics. This will be discussed in **Chapter 4**.

Chapter 1 reports a brief introduction on Liquid Crystals (LCs), the different techniques to align them and an overview on shape-changing materials. Special attention is paid to the possible modification of various mesogenic components and the consequent changes in the chemical and physical properties of the LCNs obtained after photopolymerization. Relevant examples reported in the literature are shown.

Chapter 2 reports the synthesis and characterization of liquid-crystal diacrylates (crosslinkers) having different substituents in the central aromatic core. This small palette of crosslinkers turns out to be fundamental for the generation of new materials and for understanding the impact of molecular parameters on the mechanical properties of the obtained network.

Chapter 3 reports the production of LCNs from the crosslinker palette previously discussed and the understanding of the effect of steric clutter on the mechanical and photo-actuation properties of the obtained networks. Also, the effect of the variation in the amount of crosslinker in the liquid crystal mixture is reported. This extensive to thorough characterization was carried out by comparing data obtained with those preliminarily collected in our laboratories towards the fabrication of an LCN-based artificial cardiac muscle, and on which the European Union’s Horizon 2020 research project called REPAIR (under grant agreement No 95216) is focused.

Chapter 4 deals with LCN-based micro-structure fabrication by DLW, and on their complete characterization together with their activation by heat and light stimulation. Examples of different mixtures analysed for material optimization and a first demonstration of the possible production of a micro-smart tag with a double level of encryption and decryption of the contained message are also reported. The work featured in this chapter was carried out at Trinity College of Dublin under the supervision of Prof. Larisa Florea and Dr. Colm Delaney.

Chapter 1
Introduction

1.1 Liquid Crystals: General concepts

Liquid Crystal (LC) is a state of matter in which the molecular order has an intermediate behaviour between the three-dimensional, long range positional and orientational order held in a crystal and the disorder found in an isotropic liquid (**Figure 1.1**). [7-9]

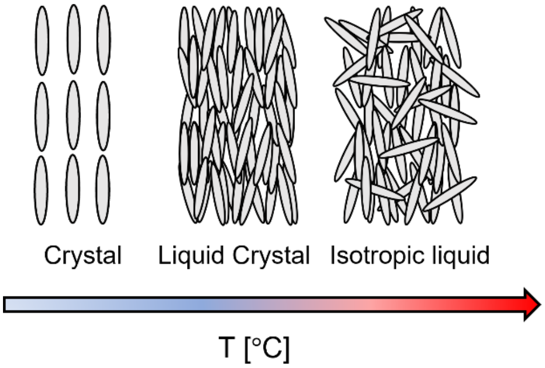

Figure 1.1: Different states of matter.

Like crystals, LCs present an anisotropic behaviour for their optical, mechanical, electrical and magnetic properties while they exhibit many features of the liquids, such as high fluidity and formation of droplets.[10] LCs can be classified in Lyotropic and Thermotropic depending on the condition needed to for the mesophase.[11]

- Lyotropic LCs: the mesophase formation and disruption is dependent on the solvent and its concentration in the environment. Typically, the crystalline order is disrupted by a solvent (commonly water) and the amphiphilic mesogens (composed by a hydrophilic polar head and a hydrophobic apolar tail) forms the mesophase at specific concentration.[12]
- Thermotropic LCs: formation of the mesophases is temperature dependent due to the specific composition of the mesogens. The LC phase can be formed by heating from the crystalline solid phase or by cooling from the isotropic liquid one. The mesophases are present in a temperature range between the melting temperature (T_m) and the liquid crystal to isotropic phase transition temperature (T_{LC-I}) on heating, or in between T_{I-LC} and the crystallisation temperature (T_{Cr}) on cooling. [13,15]

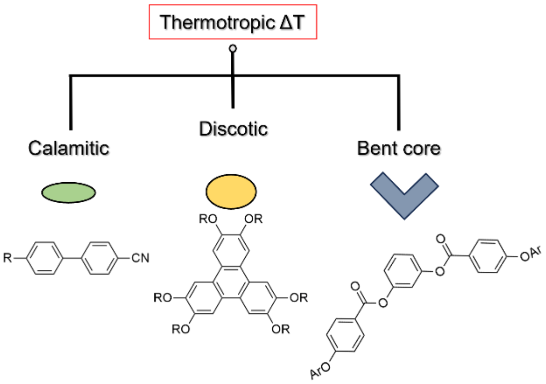

Figure 1.2: Classification of LC molecules. Classification of thermotropic LCs in calamitic, discotic and bent-core.

Generally, thermotropic mesogens are further classified according to their molecular shape, defining them as calamitic (or rod-like), discotic (or disk-like) or bent-core (commonly also known as “banana shape”) as shown in **Figure 1.2**. [13,16-19]

Calamitic thermotropic LCs, which will be the focus of the entire discussion throughout the thesis, commonly display in their molecular structure the presence of a rigid core (composed by phenyl or bisphenyl groups) followed by flexible ending units (alkyl or ether chains).[20] These characteristics of their molecular structure are responsible for the LC mesogens’ behaviour. Finally, common LC mesophases are the nematic, the cholesteric or the smectic ones shown in **Figure 1.3**. Nematic phases (N) possess only long orientational order (which is indicated by the molecular director ($\hat{n}$): the molecular order is preferentially in only one direction. [21,22] Cholesteric (or chiral nematic) phases (N*) have in addition to the nematic phase, also a helical nematic order deriving from the chirality on the mesogen or from the addition of a chiral dopant.

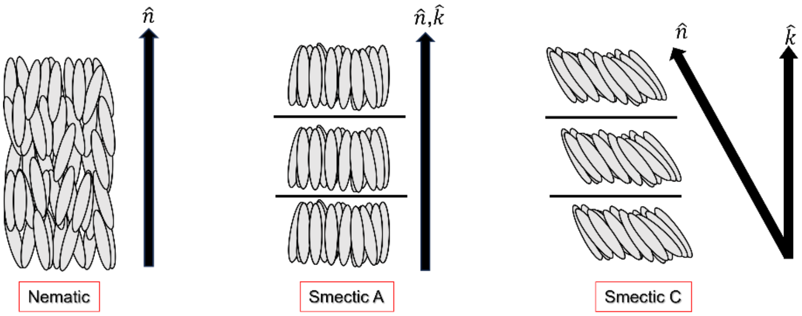

Figure 1.3: Liquid crystal mesophases.

The mesogens with chiral mesophase (N*), present a cholesteric phase in which a twisting of the mesogens is observed perpendicularly with respect to the molecular director (that is parallel to the major molecular axis). The result of this twisting results in a long-range order defined by a chiral pitch. The chiral Pitch (p) is the distance that elapses for a complete torsion (360°) of the considered mesogens (**Figure 1.4**).[23]

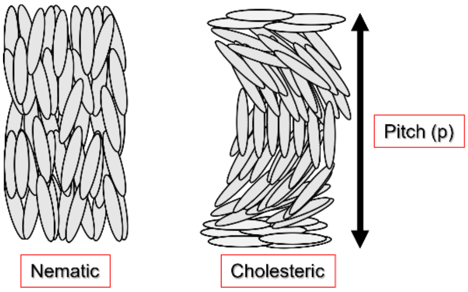

Figure 1.4: Comparison between nematic (N) and cholesteric (N*) mesophases.

Smectic phases (Sm) add to the long range orientational order the positional one due to the layering of molecules in the space. The molecules are laid parallel one to the others and organised in layers that can be parallel to the long axis (Smectic A) or tilted with respect to the layer plane (Smectic C). In addition, other kinds of Smectic mesophase were discovered and analysed. [24,25]

A thermotropic phase is also defined as enantiotropic or monotropic on the basis of the stability of the crystalline phase. An enantiotropic phase is a thermodynamically stable phase that can be formed above the melting temperature (T_m) in heating and below the isotropic liquid state on cooling. Otherwise, a monotropic phase is metastable and generated by hysteresis of the crystallisation process. The latter is observed on cooling from the isotropic liquid below the clearing temperature.

Polymeric materials exhibiting liquid crystalline properties have been termed with a variety of names including polymeric LCs, Liquid Crystalline Elastomers (LCEs), and Liquid Crystalline Networks (LCNs).

We can say that LCEs, like LCNs, consist in a liquid crystal side and/or main chain mesogenic units but its thermo mechanical behaviour can be referred to an elastomer.
LCNs notably contain a moderate to densely crosslinked network architecture associated with their preparation (acrylate-based monomers).[3]

1.2 Liquid Crystalline Elastomer: from the surface anchoring to elasticity

Liquid crystalline Elastomers (LCEs) combine the unique properties of the entropy elasticity of polymeric networks from elastomers, with the ability to self-organise molecules in liquid crystalline mesophases from LCs.[26]

These materials present a peculiar anisotropic molecular structure, which is dependent on the mesogenic molecules that are attached to a crosslinked polymeric backbone. This provides specific features that are difficult to find in other soft materials. First, LCs are intrinsically responsive to temperature variations. Temperature enables molecular order change (as for all the LC materials) that can be reflected macroscopically in a shape-change of the material (as a unique behaviour). The deformation is completely reversible (e.g., by cooling down) thanks to the elastomeric properties of the system. This behaviour can be also accompanied by the optical (colour) change due to thickness variation, if observed by polarised light (the colour is given by the birefringence property of the LCEs).[27] LCEs were theorised by De Gennes in 1975 and were immediately regarded as potential candidates to design artificial muscles.[5,28] First synthesis attempts were carried out between the late 1970s and the 1980s. In all the proposed methodologies, the key step is the alignment of the mesogen inside the final material, a molecular property that has a great impact on the mechanical and actuating properties of the polymers. The next paragraphs briefly discuss different techniques and materials suitable to align the LCs in the preferred way.

1.2.1 Alignment in Liquid Crystalline Elastomers

LCs, when unconstrained, typically organise in different domains, showing different molecular directors. This behaviour produces lattice defects and reduces their applicability in many fields. Obtaining a monodomain assembly (all the LC molecules aligned following the same director, results fundamental for some LC features, such as the peculiar optical and mechanical properties,[29] and is essential in LCN to maximise the deformation and force produced during the actuation, since it occurs along the nematic director. Interestingly, the direction of the molecular director can be pre-programmed to obtain a monodomain material that possesses a defined long-range alignment. The first attempt foresees the use of paper to rub the surface of a glass obtaining a partial planar alignment,[30] later on, other materials were demonstrated to rub glasses in order to create groves that can promote the alignment.[24,31] However, a wide range of unique procedures to achieve the appropriate alignment were described only when the commercial application of liquid crystals in display devices became feasible. Mechanical anchoring of LCs molecules on a surface is one of the simplest ways to align the material instead of the use of magnetic or electric field (that will be discussed in the next paragraphs).[32]

General molecular arrangement can be seen in **Figure 1.5** in which the alignment director and the angle formed between the alignment director and the molecular orientation can help to identify it. For the homogenous planar orientation of a nematic LC, the angle (named as θ) described is at 0° with respect to the surface plane, while for the homeotropic one the molecules are perpendicular to the surface plane describing an angle of 90° as depicted in **Figure 1.5A-B**. When the angle is between 0° and 90°, LC molecules assume a tilted orientation with respect to the surface plane (**Figure 1.5C**).

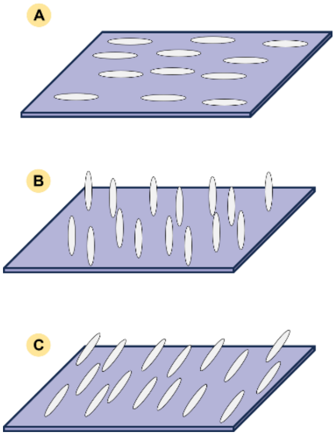

Figure 1.5: Anchoring of LCs. A) Homogeneous planar; B) Homeotropic; C) Tilted.

The most common method to reach a planar alignment for a nematic phase involves the use of rubbing on a polymer layer deposited over a glass substrate. This mechanical treatment allows to create anisotropic surfaces able to direct the molecule alignment along the rubbing direction. Common layers that are used for this purpose include polyvinyl alcohol aqueous solution or polyimide coating. [33]

These polymers can be deposited as a thin layer over a glass surface using the spin coating method and then the rubbing treatment is done by a velvet cloth (usually fixed on a rotating cylinder). The final alignment is the result of three main contributions. The first one is the surface topology of the polymer layer, the second is the rubbing process which leads to force the LC molecules to follow the direction of the layer, and the third is the electrostatic effect created by the rubbing process, which leaves charge on the surface of the polymer layer. There are many alternatives that were studied to induce a planar alignment of a nematic LC, among them to be mentioned the deposition of oxides films (e.g SiOx) on the surface of a glass substrate and the photoalignment.[34] The former method also allows tilted alignment, meaning the LC molecules change their direction from the homogenous to the homeotropic one, by varying the evaporation condition. On the other hand, the latter represents one of the most used techniques to align LCs molecules for the production of Liquid Crystal Displays (LCDs).[35] The first demonstration on the use of polarised light to align LCs molecules concerns the use of azobenzene monolayer. Azobenzene isomerisation triggers the nearest LCs molecules changing the direction of the alignment.[36] Furthermore, also the application of electric or magnetic fields can be used to reorient and align nematic LCs. This technique is based on the positive dielectric anisotropy of the LCs. Applying an electric field, depending on the sign of this dielectric anisotropy, it is possible to obtain different kinds of configurations (e.g., homeotropic and planar).[37] Moreover, magnetic fields reorient the LC molecules in one selected direction thanks to the variable induced magnetic dipole in the LC molecules resulting from the application of the magnetic field itself. [38] Among the described techniques, currently, the use of patterned surfaces, based on nano-grooved polymer, is the most common one to obtain homogeneous alignment,[39] while the use of monolayer deposition on glass substrates is the most used technique to obtain homeotropic alignment, also in the field of display manufacturing. In this case, material used in the monolayer can be surfactants (e.g., amphiphilic molecules) which possess a polar hydrophilic head and a hydrophobic tail such as lecithin or stearic acid. They are easily dissolved in organic solvents (e.g., chloroform or dichloromethane) and subsequently deposited on the glass substrate. After the evaporation of the solvent the result is a monolayer, a thin film, exposing specific organic groups on the surface able to link and reorient the LCs molecules. The crucial parameter to obtain a good alignment is the molecular density of the monolayer deposited. If it is too low or too high the interaction between the LCs molecules and the hydrophobic tail should be reduced, not leading to monodomain alignments. To overcome this issue, the preferred material is made by polyimide formulations. The interaction between LCs molecules and the hydrophobic moiety of the polyimide enhances their orientation in only one direction.[40] The use of two aligned substrates separated by a spacer (such as silica beads or Mylar films) with known thickness is one of the most common approaches for making LC cells. The LC material can be aligned in the hollow space between the two substrates in the direction imposed by the anchoring conditions.

Different alignment can be achieved by using two aligning substrates and the four more common configurations of nematic LCs are shown in **Figure 1.6**.

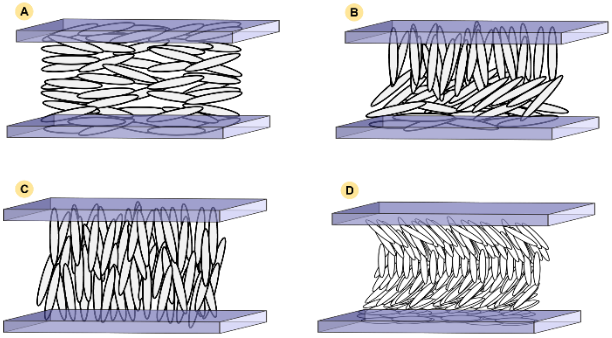

Figure 1.6: Alignments of LCs molecules in LC cells. A) Homogeneous planar; B) Splayed; C) Homeotropic; D) Twisted.

1) Homogeneous planar alignment, obtained by uniaxially rubbed surfaces presenting the rubbing directions parallel one to another;

2) Splayed alignment, obtained by one homeotropic and one planar substrate: this way, the molecular director changes its direction continuously from one plane to the other, describing a fan and going from 0° to 90° in the plane perpendicular to the two substrates.
3) Homeotropic alignment, obtained by two homeotropically-aligning substrates;

4) Twisted alignment, obtained by two planarly-aligning substrates presenting non-parallel alignment directions.

LCs are intrinsically sensible to temperature variation. In LCNs this stimulus provides a macroscopic shape-change, a process that is completely reversible under cooling thanks to the crosslinked structure of the polymer network. In general, a contraction is observed along the nematic director upon stimulation, with a consequent expansion in the perpendicular plane. Therefore, LCNs with homogeneous planar alignment can contract along a specific direction (imposed during the rubbing) as well as samples with homeotropic alignment, while engineering more complex alignment, such as twisted and splayed ones, that induce a distortion of the director throughout the whole volume of the LC substance, gives the chance to obtain more complex movement. A schematic representation of the shape-changing property of LCN is depicted in **Figure 1.7A.** LCNs which have splayed and twisted alignment show, respectively, bending and twisting movements upon the transition from nematic to isotropic phase (**Figure 1.7B-C**). In this thesis work the LC samples discussed were aligned mostly with PVA and polyimide coatings resulting in macroscopic contraction along the director in response to external triggering.

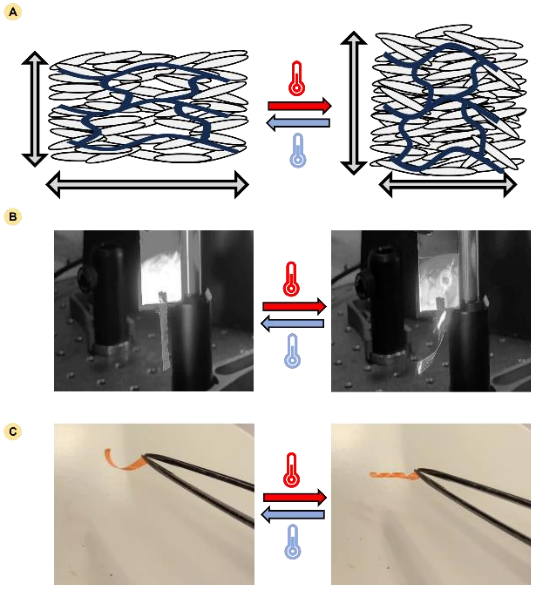

Figure 1.7: Shape-changing property of nematic LCN with different alignment. A) General scheme of the shape-changing property of LCs reacting to temperature; B) Splayed aligned LCN reacting to green light (534 nm); C) Twisted aligned LCN driven by temperature.

1.3 Chemistry of LCNs: General synthetical procedure enabling different polymeric architectures

De Gennes first discussed LCEs in 1969,[41] when he investigated the potential functionalities of polymer networks including molecules able to form liquid-crystalline phases. He theorised these concepts to the unique condition of a crosslinked liquid-crystalline polymer in 1975.[42] Four alternative material architectures can be produced using different monomers and crosslinkers during the production of an LC polymer (**Figure 1.8**).

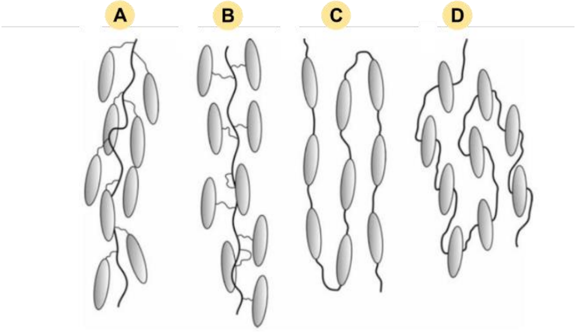

Figure 1.8: LC polymers architectures. A) Side-chain "end-on"; B) Side-chain "side-on"; C) Main-chain "end-on"; D) Main-chain "side-on".

LC polymers can be built by chemically linking mesogenic groups to polymer chains. Different structures can be obtained depending on how the mesogens are linked to the backbone: either the mesogens can be attached with a flexible spacer to the network (side-chain polymers, **Figure 1.8A** and **B**) or directly linked together within the chain (main-chain polymers, **Figure 1.8C** and **D**). Another structural modification is given connecting the mesogenic groups in different geometries: for example, rod-like mesogens could be attached via their long axis ("end-on" type polymers, **Figure 1.8A** and **C**) or via their short axis ("side-on" type polymers, **Figure 1.8B** and **D**).[43]

Finally, it is possible to combine the two structural principles to create mixed main-chain/side-chain polymers (referred to as "combined" LC polymers.[44]

Finkelman provided an important contribution to the study of LCEs and their synthesis [43], demonstrating how to produce LCE starting from a linear polyhydrosiloxane chain, that was coupled with mesogenic groups and a crosslinking agent with functional vinyl- and methacryloyl- groups. The creation of a liquid crystalline polymer and its crosslinking are two key steps in LCE synthesis. For this reason, the material was produced in a two-step reaction by a Pt-catalysed hydrosilylation reaction.[45] This technique produced a wide range of LCE samples, and a general scheme of the reaction is reported in **Figure 1.9**. The advantage of this technique is that it allows the preparation of samples of any size because the mesogen alignment is accomplished by the mechanical stretching of the final polymer. Additionally, main-chain polymers have been produced via silicone chemistry by a polycondensation reaction with di-vinylic monomers and tetramethyldisiloxane.[46] However, the mechanical alignment presents main limitations such as the impossibility to use it for small and micro-structures, and the possibility to obtain only homogeneous planar LC alignment.

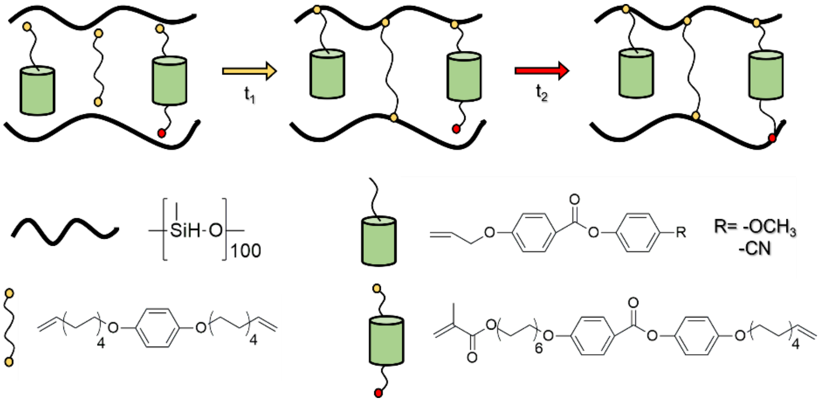

Figure 1.9: General scheme synthesis of LCEs concerning hydrosilylation.

These issues can be solved by using free-radical polymerization (a general scheme is reported in **Figure 10)**.

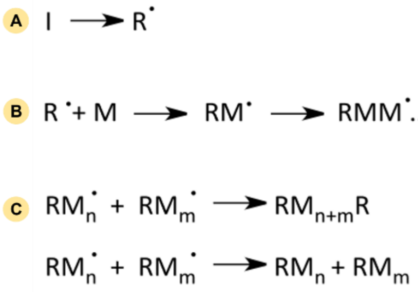

Figure 1.10: General scheme of free radical polymerization process.

Through **Figure 1.10**, it is possible to highlight the three different steps of free radical polymerization. The first one is the initiation in which the first radical is formed by the homolytic cleavage of a bond in a molecule of the initiator (by light irradiation or temperature) (**Figure 1.10 A**). Stimuli commonly used to form radicals are heat, light, redox reactions or electrical stimulus. By using light (UV and visible) it is possible to obtain free radicals at specific temperatures. The second step (chain propagation step) involves the reaction of the first free radical with the monomer (mesogenic monomer) producing other radicals until the monomer is fully consumed (**Figure 1.10 B**). The last one, defined as termination step (**Figure 1.10 C)**, occurs for combination of two radicals or for disproportionation, where a hydrogen atom is abstracted from one chain end to another. For the production of LCNs by this strategy, functionalized mesogens (monomer and crosslinker) with polymerizable groups, such as acrylate, are needed, and polymerization occurs (commonly using UV-light of 365 nm) following the mesogen alignment in the nematic phase. This technology is compatible with various alignment techniques, well known from low-molecular-weight LCs, because the alignment is performed at mesogen and not polymer level and allows the production of LCNs at various length scales.

Of fundamental importance is the possibility to conduct the polymerization reaction in the nematic range temperature of the mesogen mixture, to obtain well aligned and therefore functional LCNs. A general scheme for the preparation of acrylate-based LCN is shown in **Figure 1.11.** In this example, both monomer and crosslinker are functionalized with one or two acrylate groups, respectively.

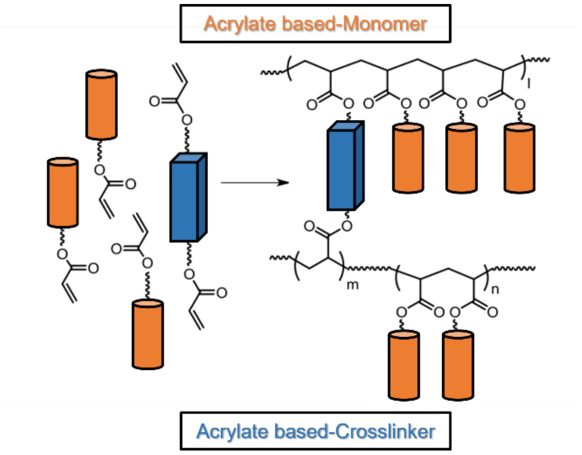

Figure 1.11: Free radical polymerization for the realisation for acrylate based LCNs.

The mesogenic monomer is responsible for the LC properties of the materials and for the alignment of the LCN, while the crosslinker (not necessarily showing LC behaviour) is responsible for the mechanical properties of the final material. Finally, also an initiator is needed to control in space and time the polymerization reaction, which can be started via heat or light. The versatility of acrylate chemistry also allows access to non-conventional fabrication methods. Replica moulding was used to produce patterned LCNs with great reproducibility and over centimetre scale distances in 2D geometries [47]; while Direct Laser

Writing approach was shown to be a helpful tool to build LCN structures in arbitrary forms with high resolution (approximately 200 nm) for micro-fabrication of 3D structures.[48]

1.4 Photo-responsive Liquid Crystalline Networks

The shape-change property of LCNs, discussed in section 1.2, is the result of the progressive disordering of the nematic order induced by heating. In some cases, a phase transition, from the nematic to the isotropic one can be observed also for LCNs. Cooling down the system, it is possible to restore the original molecular alignment and the macroscopic shape of the sample. To develop different applications, other stimuli are more convenient rather than the temperature control and, between them, we can cite the use of light, electric or magnetic fields. Among these stimuli, light was the first stimulus taken into consideration by the scientific community [49] and also the stimulus of choice in this thesis. Light has a low environmental impact, is inexpensive and leads to actuators with possible remote control and short response time (up to millisecond time scale).The functionalization of LCNs with photo-responsive units can follow two different approaches: i) the dispersion of molecules or nanostructures after the formation of the LCN within the polymeric structure; and ii) the use of photochromic molecules directly linked to the polymer structure of the LCNs.

Many examples of the former method are reported in the literature. The first and valid demonstration of this approach involves the use of carbon nanotubes dispersed within the LCN after its preparation. The formed thin film is a composite material that exhibits significant reversible contraction when irradiated by light in the IR field. Carbon nanotubes act as nano-heaters. The interaction with the electromagnetic radiation, of appropriate wavelength (comparable to the size of the inserted nanotubes), causes electronic excitation that is released in the form of heat causing the nematic to isotropic transition of the liquid crystal.[50] The same approach can be exploited also with different dyes and other inorganic nanoparticles [51], such as gold nanorods.

On the other hand, the second light activation mechanism takes advantage of the use of photochromic molecules, such as azobenzene or spiropyrans, and their molecular changes in response to light. These molecules, under appropriate irradiation, cause the transition from the nematic to the isotropic phase at constant temperature (isothermally). Among them, azobenzenes are the most widely explored, and respond to specific wavelength with a reversible isomerization between two geometric isomers (*trans* and *cis*). The *trans* isomer is more stable than the *cis* isomer (energetically disadvantaged), so is the most favoured and more present (99.9%) at room temperature.[52] It is planar, and it does not present a dipolar moment, while the *cis* conformation, not being planar, presents a moment of dipole. The structure of the two geometric isomers and the UV-visible absorption spectrum are shown in **Figure 1.12**.[53]

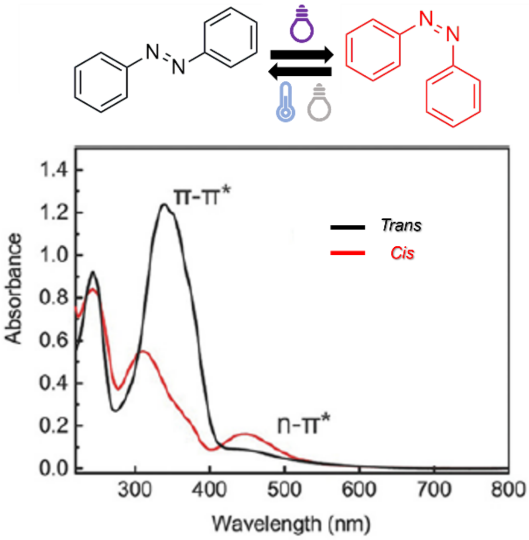

Figure 1.12: Molecular structure and UV-Vis spectra of azobenzene isomers.[54] Copyright Wiley-VCH Verlag GmbH & Co. KGaA. Adapted with permission.

As evident from the absorption spectrum, the *trans* isomer has a strong transition near 320 nm and a weak transition at 440 nm. Whereas the *cis* isomer, which overlaps in part with the previous spectrum, has a strong absorption at about 440 nm in the ultraviolet (UV) region. Photo-isomerization can be caused by radiation with UV-light, while for the *cis* to *trans* conversion, visible light is needed, or it can occur spontaneously in the dark. Such thermal relaxation has a kinetics that can falls in very different time scales (from days versus picoseconds) depending on the substituent on the aromatic rings of the azobenzene.[55] Being planar, the *trans* isomer can easily stabilise the nematic liquid crystals order and it align along the mesogenic director. On the other hand, the *cis* isomer formation leads to perturbation of the molecular order with a consequent reduction of the isotropic nematic temperature (T_{N-I}), and, in specific conditions, to a phase transition. However in most cases, light driven deformation of LCN is given by a combination of the two effects, namely the isomerization of azobenzene (photo-chemical effect) and a photo-thermal effect.[56] Patrick Keller and his collaborators proposed the first photo-actuated side-on side-chain LCN prepared by photopolymerization[57] using an azo-dye substituted with a reactive group suitable for direct bonding within the molecular structure of the LCN. In between, the first examples of dye dispersion within the LCN, we can find a work presented by Finkelmann and coworkers using Disperse Orange I. [58] The LCN film is soaked in a dye solution in toluene and then left to dry. The actuation kinetics are really fast, showing 20 ms for the activation, and 74 ms for the relaxation, demonstrating that not only the manner of insertion but also the dye molecular structure have a great impact on the actuation properties of the material. [59,60] The mechanism of this light response has not been clarified in the article. More recently, Da Cunha and co-workers reported a detailed work on the photo-actuation mechanism in air and water.[61] Several LCNs were compared containing the dye linked to the structure in different ways: i) a pendant monoacrylate dye, ii) a pendant monoacrylate dye with a nitro group (similar case shown by Finkelmann), iii) diacrylate dye used as crosslinker agent For all the examples, the temperature increase due to light irradiation was considered, both in air and water. All the films activated rapidly and qualitatively in a similar manner, showing a linear increase in temperature with light intensity. Interestingly, in water, all the films stopped responding except for the one which presents the dye as a crosslinker agent in the network which can implement the effect of shape-changing of the LCN. So, in LCNs the azobenzene cross-linker provides photomechanical actuation via the isomerization mechanism whereas the pendant azobenzenes can predominantly act via the photothermal effect which amplifies the actuation properties of the material.

1.5 Engineering of the properties of the mesogen: new liquid crystalline crosslinker

Understanding the relation between chemical structure and liquid crystalline mesophases properties becomes fundamental can be only partially rationalised by an empirical approach.[7] For example, Vorlander has investigated the influence of the length of the polymeric molecules on the material thermal and optical properties, obtaining the first oligomeric liquid crystalline polymer.[62]

The evidence of the dependence of the mesomorphic features on the geometrical shape of the mesogen has prompted the research to interpret possible correlations, linking the variation of the mesomorphic properties, dependent on the geometry of the mesogen analysed, with two elements: the molecular anisotropy and the intermolecular interaction.[7]The majority of the calamitic LCs molecules, commonly identified as rod-like molecules, can be represented by the general formula reported in **Figure 1.13**. They are composed by two or more rings (R, R’) named as stiff central core, which are bonded directly or connected by linking groups (X) and may be extended by a chain extender (Y, Z) possessing terminal groups (W, K) and lateral (A, B) substituents.

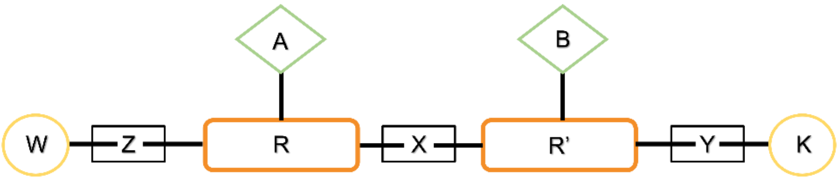

Figure 1.13: General structure of calamitic LCs.

Each part is discussed below.

- Calamitic core: usually is composed by phenyl systems formed by one or more benzene rings (or at list rings). These molecules provide anisotropy to the system imparting the aforementioned rod-like shape. Being formed, mainly by a multi ring system, they are mechanically stiff. In addition, the presence of rings does not affect only the mechanical properties of the mesogen but also the mesomorphic ones. In fact, by increasing the number of rings present in the core it is possible to observe an increase in the clearing temperature (the temperature needed to pass from the LC to the isotropic phase). If the temperature is too high it is possible to have an experimental limit to observe it, and the clearing temperature (T_{N-I}) cannot be determined. For example, 6-benzene systems are rod-like prototypes in which high clearing temperatures are justified by the presence of diffuse intermolecular forces between the rings and aromatic π-π stacking.[7] Substituting benzenes ring with heterocyclic systems, in which one or more carbon atoms of the benzene ring are replaced with nitrogen (e.g., pyridine, pyrazine, pyrimidine and pyridazine), instead lowered mesophase formation temperatures.[63]The replacement of aromatic rings with aliphatic rings (cyclohexane, cyclohexene etc.), on the other hand, causes a rapid lowering of the intermolecular forces of the system and a lower packing fraction which causes a rise in clearing temperatures (T_{N-I}). In the case of hetero substituted saturated rings (piperidine, piperazine or dioxane) polarity of the present substituent and the molecular arrangement can negatively influence the mesogenic properties of the considered molecule, breaking into the molecular symmetry.

- Linker: chemical groups that connect the rings of the liquid crystal mesogen. These increase the molecular length while maintaining its linearity. The most common include alkyl, alkoxy, amine, thiocyanate and so on. The stability of the LC mesophase in this case is not only related to linearity but also to the polarity of the linker and to the possibility of forming *trans* or *cis* conformers. As for the unsaturated linkers, the focus should be on the possible electronic and aromatic conjugation of the rings with the linker itself.[64] In the case of alkoxy linkers, given the increased molecular mobility and through electronic coupling between oxygen and the core can lead to a lowering of the clearing temperature.

- Terminal substituents: The most used are alkyl and alkoxy substituents but may be cyano, nitro, halogenated and isothiocyanates groups. Alkyls and alkoxy groups lower the melting temperature thanks to the increased mobility of the system and the possibility of conformational variation of the chain from the *trans* to the *cis* one. Important to note that, reducing the length of the alkyl chain, a change in the molecular behaviour from enantiotropic to monotropic was highlighted, considering the same homologous series. When polar groups are present instead, the interactions between polar groups of different molecules create a rod-like structure that is more compact, predicting an increase in the clearing temperature.

- Lateral substituent: commonly we can find halogens (F,Cl,Br), alkyl chain, cyano groups (-CN) and some others. They have the role to reduce the ratio between length and breadth named as X and shown in **Figure 1.14**.

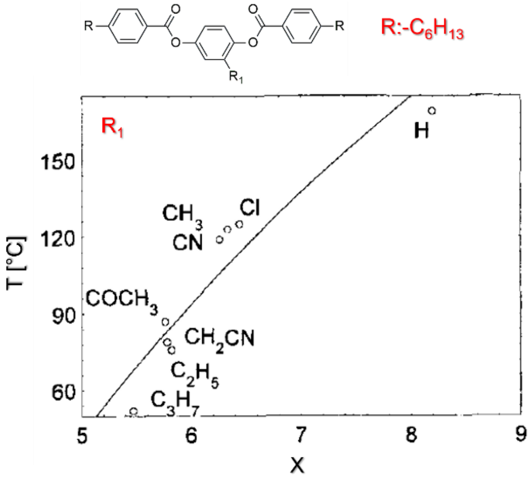

Figure 1.14: Behaviour of the clearing temperature reported on the length to breadth ratio (X) in the case of homologous series taken by 2-substituted hydroquinone-bis-[4-n-hexylbenzoates].[7] Copyright Wiley-VCH Verlag GmbH & Co. KGaA. Adapted with permission.

As reported in the graph shown, reducing X calls for a reduction in the clearing temperature of the mesogen. Polar groups can have a huge impact in the reduction of the $T_{N\text{-}I}$. This is due to the polar attraction and the increasing of the density and the respective decreasing in the symmetry of the system. As an example, the use of fluorinated substitution on the aromatic central core of rod-like mesogen also demonstrates the possibility to generate, beyond the nematic phase, also smectic phases (A and C).[65,66] Moreover, these features are not limited only to the substitution on the central aromatic core, but they can be applied in all the previous parts discussed, to enhance the mesophase properties, thus creating a fascinating tool to be used for different purposes.[67] Considering the realisation of LCNs, most reports employ materials prepared by mesogenic diacrylates having a rigid core with 3 aromatic rings (some of them also commercially available) used directly for photopolymerization and crosslinking[68,69] or firstly oligomerized by Michael addition (by adding amine or dithiols) and then cross-linked, to obtain main-chain elastomers.[70,71] A great challenge remains the LCN optimization in terms of mesomorphic, elasticity and strength toward their real application. In this regard, all the molecular parameters have a great importance in determining the LCN performance. Among them, the link of the liquid crystal unit to the polymers (from main-chain to side-chain polymers with different conformations) affects the maximum deformation under stimuli,[72,73] while increasing the spacer length led to an increase of the order parameter[74] and to an improved deformation at lower temperatures.[75] Playing with the crosslinking degree, the material rigidity can be adjusted to allow the 3D printing[74,76] or to modulate the extent of deformation.[77] An alternative strategy to improve the LCN mesomorphic and mechanical properties consists in creating a double interpenetrating network[78,79] which however requires extra steps during the fabrication, and that is difficult to apply for patterned materials or in microfabrication. An easier method to tune the polymer properties consists in mixing monomers with different mesogenic cores with the aim to decrease the interaction energy in between the cores, thus improving the mesogenic features. Mixing LCs with 2 and 3 aromatic rings in the rigid core was demonstrated as a successful way to decrease the actuation temperature in main-chain LCNs prepared both by acrylate units[80,81] or thiol-yne click chemistry.[82] In a similar way, the use of a mixture of mesogens based on both aromatic and cyclohexyl rings has been described to decrease the energy needed to obtain the phase transition.[72] Recently, for main-chain LCNs, it was also observed that dilution of the mesogenic parts with other co-monomers without LC properties (e.g. ethylene glycol based monomers) allows to decrease the actuation temperatures.[83,84] For that reason, the evaluation and the possibility to tune the properties of the entire polymer network by appropriate selection of the mesogenic molecular structure, is one of the most powerful tools nowadays.

1.6 LCNs applications

Due to the peculiar properties of LCNs, discussed in the previous sections, these materials have long been discussed for applications in different fields. In particular, the impulse in the study of thermotropic calamitic liquid crystals has taken place in the development of electro-optical displays called liquid crystals displays (LCDs). [7,85] Liquid crystals, in this case, are used as a moderating medium for transmitted light due to their physical properties of birefringence. Unlike their predecessors, they allow chemical stability, a wide temperature range in which they can operate (e.g., by simply changing the formulation of the mixture used), dielectric anisotropy, and viscosity.

Thanks to these chemical-physical properties, liquid crystals in general have distinguished themselves as possible promising materials in the field of actuators, sensors, microvalves, pumps for microfluidics, artificial muscles, and biological aligning surfaces. Given the property of shape change, the first application for LCNs was as actuators. From an applicative point of view, the main characteristic of an actuator is the movement related to the actuation, but also its direction and the combination of movement in relation with the force generated by the material. These parameters are crucial and should be modulated through the chemical structure of mesogens, as shown in the previous paragraph. In general, LCNs can have a very wide range of optical, thermal and mechanical properties. Designing a different architecture, the mechanical and thermal properties of the LCN vary drastically (elastic modules can vary from Gigapascal to Megapascal comparing side-chain LCN and main-chain LCN). This is identically reflected in the actuation property. These actuator properties immediately found their way into the field of tissue engineering, particularly with the aim to build artificial muscles, [6,86] as predicted by De Gennes in 1975,[41] theorising the possibility to use nematic LCEs, showing contraction or extension along one direction, to mimic the activity of a muscle. The question that remains open concerns the relative conversion of energy into mechanical work. Various approaches have been attempted and molecular modifications to the structure of LCNs are of fundamental importance to adapt and modulate the mechanical energy. In addition, the kinetic activity must be respected. These parameters are discussed in detail in **Chapter 3** of this thesis for the realisation of a cardiac contractile unit based on photo-responsive side-chain LCNs, which can mechanically assist cardiac muscles.

In the field of actuators, Yamada et al. [87] produced a light-driven motor using a side-chain LCN with a photo-responsive azo-dye, as depicted in **Figure 1.15A.**

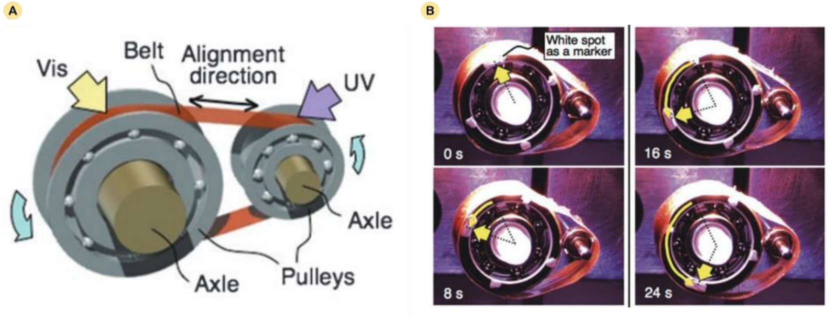

Figure 1.15: Light-driven motor produced by LCN films. A) General scheme of the light driven motor. B) Series of images of the illumination provided to the sample and the movement of the belt. Copyright Wiley-VCH Verlag GmbH & Co. KGaA. Adapted with permission.[87]

On one side, irradiation with UV light causes the *trans-cis* isomerisation of the material and consequent contraction, while on the opposite side, the application of visible light causes the reverse isomerisation and the consequent expansion of the material (**Figure 1.15B**). The combination of these actuations makes the belt move, effectively constituting a motor.

Similarly, Ikeda et al. [71] demonstrated the bending of a non-responsive material when it is coated with a photo responsive LCN film. By different illumination cycles, it is possible to guide the sample towards more complex movements, depending on the size of the edges (**Figure 1.16A**). In fact, an azo-dye doped LCN has been observed to have worm-like movements under UV and visible cyclic illumination if its edges are rounded on one side and sharp on the other. The resulted bending is controlled by the isomerisation of the dye, while the direction is controlled by the edge shape as depicted in **Figure 1.16B**.

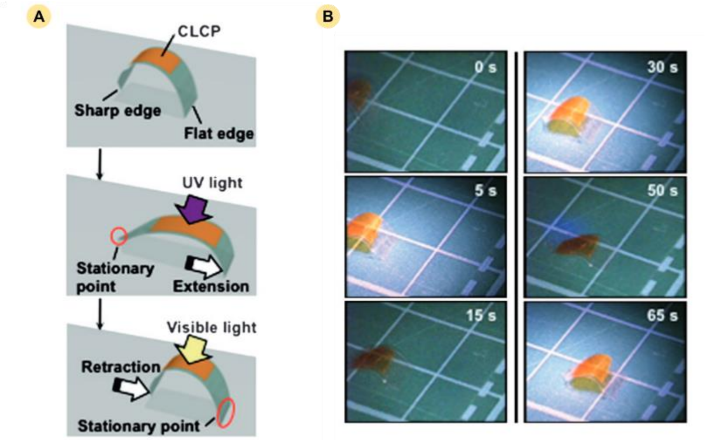

Figure 1.16: Light-responsive worm-like actuators made by LCN. A) Scheme of the complex movements reached by combination of light and edges. B) Frames of the video recorder for the actuation of the LCN strip.[71] Reproduced by permission of the Royal Society of Chemistry.

Due to their ability to respond to different types of external stimuli (light, temperature, magnetic fields, electric fields, vapours, etc.) LCNs are also interesting as sensors.[88] Sanchez-Ferrer et al. combined the sensor concept with the realisation of an LCN-based micro-valve for microfluidic applications.[89] The first hybrid system demonstrated to control the flow of fluids through its contraction and relaxation. The development of such micro-valve and micro-pump opened for further investigations, among them of certain interest are micromechanical systems (MEMS) or lab-on-a-chip based on LCNs reported by Broer and coworker.[90] By multi-inkjet printing, they described LCN-based photo-responsive cilia able to simulate the movement of the natural ones (**Figure 1.17A**).

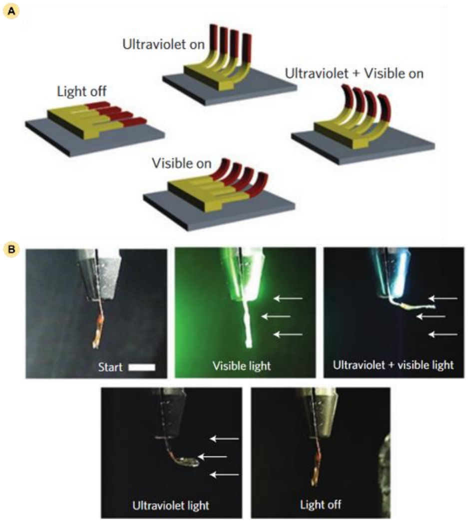

Figure 1.17: Artificial cilia made by LCN and produced by multi-inkjet printing. A) Scheme of the light -responsiveness of the cilia. B) Pictures depicting the complex movements realisable with the artificial cilia. Reprinted by permission of Nature Materials.[90]

Photo-mobility of the system is ensured by using different wavelengths, even allowing for complex movements (**Figure 1.17B**), and demonstrating the possible use of such a micro propulsion system for creating flow and mixing fluids in wet environments (lab-on-a-chip).

More recently, thanks to their micro-patterning and alignment properties, LCNs have also emerged as promising materials for cell contact guidance. The self-assembly capabilities of liquid crystalline mixtures allow for different topography, suitable to create cell scaffolds with pre-determined morphology that can guide the organisation of different cell lines.[91] It is evident how tuning the LCNs properties by different approaches (e.g. molecular modification, insertion of responsive molecules, miniaturisation of the materials and so on) open the via to a plethora of applications spanning from the biomedical application over to the robotic field. In the next chapters we will focus our attention on describing materials ale to be used in the fields of cardiac tissue engineering and of encryption.

Chapter 2

Synthesis of new mesogenic crosslinkers

2.1 Introduction: New Liquid Crystalline diacrylate mesogen

Phase behaviour modulation of liquid crystalline mesogens can be addressed by structural modification at molecular level. Starting from a rigid rod-like core – e.g., composed by aromatic rings – reduction of the symmetry or increase of the steric hindrance by different substituents generally reduces the clearing temperature. Similar approaches can be explored to modulate the properties of Liquid Crystalline Networks (LCNs). Photopolymerizable crosslinkers, bearing different lateral groups on the aromatic core, are reported. They were able to strongly modulate the material thermal, optical and mechanical properties.

To improve the LCN performance, we prepared and characterised new liquid crystalline acylate based crosslinkers taking into account the ease of their synthesis and their possible scaling up. Starting from a commonly used benzoic acid derivative (presenting and acrylate group), we prepared a small library of crosslinkers by esterification with hydroquinones presenting different bulky substituents, shown in **Figure 2.1**.

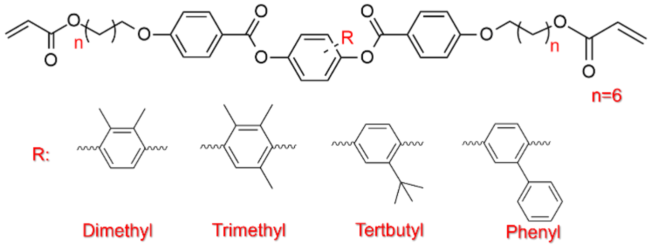

Figure 2.1: General formula of the diacrylate mesogen evaluated and possible substitution on the aromatic central core investigated.

The LC behaviour of this new palette of crosslinkers was carefully evaluated thanks to the use of Optical Polarised Microscopy (POM) and Differential Scanning Calorimetry (DSC). Optical Polarised Microscopy is an essential technique that can be used in combination with DSC to reach information about the mesomorphic properties of the mesogenic materials analysed. Mesogenic units, as defined in **Chapter 1**, can form molecular organisation that is between a liquid and a crystal. Not owing the perfect order of a crystal they can have defects. These defects, when observed with an optical polarised microscope, give rise to classical textures that are characteristic for each liquid crystalline phase evaluated. For this reason, POM represents a powerful tool for the identification of the type of mesophase and to provide the phase transition temperatures of the mesogen, like with DSC.

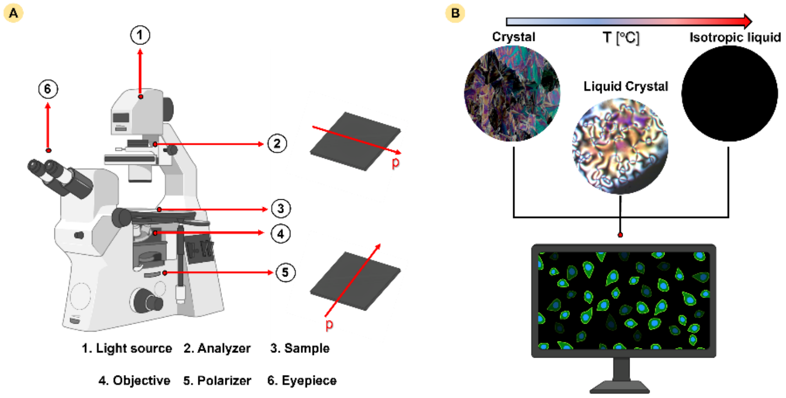

Figure 2.2: General scheme of Optical Polarised Microscope (POM). A) Components of an optical polarised microscope. B) Investigation scheme of the texture mesophase of a LC under temperature.

Briefly, as depicted in **Figure 2.2A,** an optical polarised microscope is equipped with a light source (which should be a white lamp **1**) two polarisers called analyser and polarizer (**2** and **5**), the sample stage (**3**), an objective (**4**) and an eyepiece (**6**). Commonly, for the analysis of LC mesophases this kind of instrumentation is also equipped with a digital camera (projecting on screen), a hot stage to study the transition temperatures and a routable stage for the sample. To underline the difference with a common microscope, in this case the lenses (analyzer and polarizer) are polarised, which means that when the light source hits the first lens, the direction of the light is cut in only one direction. Most important is that the second lens is cross-polarised with respect to the first, which means that the two lenses are at 90° to each other. This is depicted in **Figure 2.2A** where “p” is the polariser vector of the lenses. In between the two lenses there is the LC sample, which possesses birefringence properties. When the polarised light hits a birefringent sample, the rays will be splitted in two rays. The first one (ordinary ray) has a linear polarisation parallel to the incoming polarisation of the light and, consequently, perpendicular to the analyzer. This light is then completely extinguished and does not contribute to the image observed by the analyser. The second ray (extraordinary ray) is tilted at an angle, called phi (φ). This ray can pass through the analyzer forming a characteristic image during the observation. It produces the typical colourful images displayed commonly by liquid crystals (**Figure 2.2B**). In case of no birefringent material the field of view is always black. A common methodology to study the presence of mesophases is based on the POM observation during a temperature scan of the sample from room temperature, or even sub room temperature, to the melting temperature. For an enantiotropic LC phase, this should be possible observed both over heating and cooling down the system in between the melting temperature (transition from crystal to LC) and $T_{N\text{-}I}$. On cooling, the system passes from the isotropic liquid to the liquid crystal mesophase ($T_{I\text{-}N}$) and should crystallise (T_{Cr}) again or remain in the liquid crystal phase. If the liquid crystal mesophase was observed only cooling down the isotropic melt, we can define the LC as monotropic. The defects possessed by the specific LC organisation come out with textures that are characteristics for each mesophase. Nematics LCs that are confined between two cover slides and are oriented commonly with the director parallel to the substrate. When this orientation is presented, it is sometimes possible to observe the so-called "Schlieren texture" by POM.

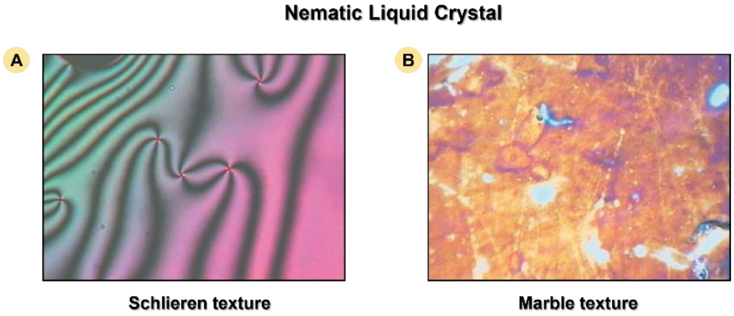

Figure 2.3: Nematic LCs textures. A) "Schlieren texture" observed by POM. B) "Marble texture" observed by POM. [24] Copyright Wiley-VCH Verlag GmbH & Co. KGaA. Adapted with permission.

Schlieren texture, depicted in **Figure 2.3A**, is based on a characteristic set of dark brushes that correspond to the extinction points of the nematic director with the light incident. From this point, named as defect, it is possible to observe two or four brushes and, in this case, we can define the LC as nematic. Furthermore, there are other classical textures that can define a LC as nematic. One of them is the so-called "Marble texture", depicted in **Figure 2.3B**, showing in different areas of the sample, that appear uniform, colour changes depending on the different transmission of the light and the birefringence behaviour from the plane of the director. However, only the Schlieren texture is generally used as diagnostic for the nematic phase.

A more precise determination of the phase transition temperature can be described by Differential Scanning Calorimetry (DSC) measurements. Such technique determines the heat flow generated from the sample analysed if compared to a reference (an empty pan of aluminium). This difference can be positive or negative, is measured from thermo-couples (platinum wires) and is reported with respect to the temperature. Standard thermograms need to specify the heat flow direction reporting if the exothermic peaks are down and the endothermic up or vice versa.

From this analysis it is possible to identify the melting temperature (T_m), the crystallisation temperature (T_{Cr}) and the LC-to isotropic phase transitions temperature (T_{LC-I}) while to understand the nature of the LC phase (nematic, smectic, etc.) POM and X-ray diffraction analysis are needed.

Furthermore, DSC allows us to better understand if the mesogenic material analysed has enantiotropic or monotropic behaviour. **Figure 2.4** shows an example of a trace of a second heating and cooling ramp for a diacrylate mesogen. It shows the enantiotropic behaviour of the molecule as the phase transition temperature peak of the liquid crystal phase is present both in heating and cooling. This peak has a low value of enthalpy, as commonly this transition appears between 5 and 10 times smaller if compared to melting or crystallisation processes on the trace. In contrast, the main transitions like the melting and the crystallisation phase are intense peaks that can be broad or narrow.

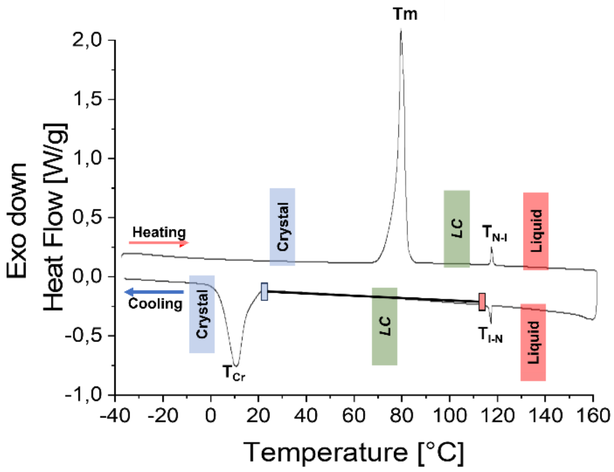

Figure 2.4: General DSC trace for the second heating and cooling cycle.

Another information from the DSC traces is the range of temperature in which the liquid crystalline phase is stable, which is fundamental for the application of these materials. Lastly, from the peak integral, it is possible to calculate the enthalpy involved in the transition (**ΔH**). In the next sections, the effect of the introduction of different substituents on the central aromatic core in liquid crystalline crosslinkers is evaluated by combining both POM and DSC analyses. The modification of the lateral groups of the mesogen core should be an efficient strategy to modulate the phase transition temperatures at least of low molecular weight LC.[92] Introduction of sterically hindered groups or reduction of symmetry can lead to a decrease in the clearing temperature thanks to a controlled reduction of the side-by-side intermolecular interactions, up to a critical point where the LC properties are lost.

2.2 Result and discussion

In this chapter, crosslinkers reported are called CLn-m, where n is the number of carbon atoms in the alkyl chain spacer and m is the substituents on the central phenyl ring of the LC core. For example, the reference crosslinker RM257 is called here CL3-Me, where 3 indicate the presence of a propyl spacer in between the core and the acrylate group, and Me indicate a methyl substituent in the central aromatic ring. Accordingly, the monomer mixture and the LCNs are called LCNn-m.

Both CL3-Me and CL6-Me are commercially available molecules (called RM257 and RM82, respectively) and differ only for the spacer length (3 or 6 atoms of carbons in both terminal flexible spacers), while the other crosslinkers were synthesised to increase the steric hindrance of the mesogenic core. This is expected to destabilise the weak interaction among LC cores inside the material, also affecting the actuation performances of the polymeric systems. In particular, the modification of the central hydroquinone derived core was performed by increasing the number of methyl groups (2 and 3 for CL6-diMe and CL6-triMe, respectively) or changing the substituent on it (a phenyl ring for CL6-Ph or a *tert*-butyl group for CL6-tBu).Crosslinkers were prepared in 3 steps according to **Scheme 2.1** (all the informations for the reagents used are contained in **Table 2.3** in the **Experimental**

Section), and a complete Nuclear Magnetic Resonance (NMR) characterization of the compounds is reported in **Figures 2.7-2.18.**

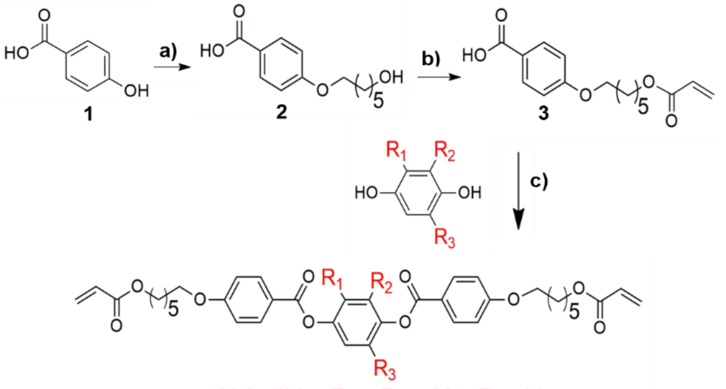

CL6-diMe: R$_1$ = R$_2$ = Me; R$_3$= H.
CL6-triMe: R$_1$ = R$_2$ = R$_3$ = Me.
CL6-tBu: R$_1$ = R$_2$ = H; R$_3$=tBu.
CL6-Ph: R$_1$ = R$_2$ = H; R$_3$ = Ph.

Scheme 2.1: Synthesis of the steric hindered LC-crosslinkers. Reagents and conditions: a) 6-chloro-1-hexanol, KOH, KI, EtOH, H_2O, reflux, 18 h, 86%; b) acryloyl chloride, NMP, RT, 3 h, 100%; c) DCC, DPTS, CH_2Cl_2, hydroquinone derivative, 50 °C, 72 h. Yields: 63% for CL6-diMe, 56%, for CL6-triMe, 49% for CL6-tBu, 54% for CL6-Ph.

In all cases, the same building block **3** was esterified with different hydroquinones to get the final products. [93,94] Briefly, starting from the 4-hydroxy benzoic acid (**1**), the alkyl spacer was introduced by the Williamson reaction using a chloro-alcohol. The appropriate chemo-selectivity was guaranteed by using a combination of water and ethanol as solvent and obtaining the substitution only on the phenolic group. Molecule **2** was then treated by acryloyl chloride to introduce the polymerizable group leading to the common building block **3**.[95] The most critical step was the third one, since the Steglich esterification with sterically hindered hydroquinone should lead to slow reactions and low yields. After the screening of different conditions, the best synthetic approaches were based on the use of the DCC (N,N'-dicyclohexylcarbodiimide) or EDC (1-Ethyl-3-(3-dimethylaminopropyl)carbodiimide) as the coupling agent, and DPTS (4-(dimethylamino) pyridinium p-toluenesulfonate),[96] even if only moderate yield were obtained. See **Table 2.1** for a comparison on the esterification conditions.

Table 2.1. Comparison of different esterification conditions synthesis of crosslinkers. Conditions A: DCC, DPTS, CH_2Cl_2, 50 °C, 72 h; Conditions B: EDC·HCl, DPTS, CH_2Cl_2, 30 °C, 16 h.

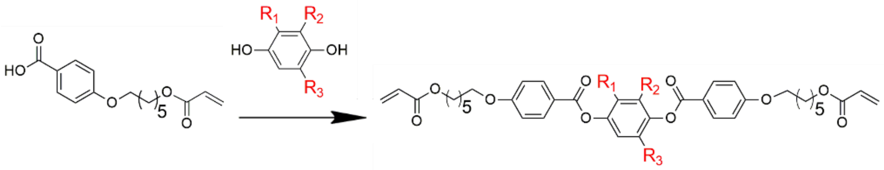

Substituent (R)	Yield for condition A [%]	Yield for condition B [%]
R_1=R_2: -Me; R_3: -H.	65	-
R_1=R_2=R_3: -Me.	59	72
R_1=R_2: -H; R_3: -tBu.	49	36
R_1=R_2: -H; R_3: -Ph.	54	57

However, such a moderate yield was balanced by the opportunity to purify all the intermediates and the products by crystallisation processes, thus avoiding chromatographic columns that usually limit the scale up of the synthetic procedures. The mesomorphic properties of the molecules have been studied by Differential Scanning Calorimetry (DSC) and Polarised Optical Microscopy (POM). Combining the results from both techniques, we were able to determine the phase transition temperatures and the type of LC phases as representatively shown in **Figure 2.5** for the crosslinker CL6-triMe. In this case, during the calorimetric analysis (**Figure 2.5A**), the molecule presented only one endothermic peak during heating due to the melting in the isotropic phase, while on cooling, two exothermic peaks were present. The first peak indicated an isotropic to liquid phase transition which can be attributed to a nematic phase thanks to the observation of its typical texture by POM (**Figure 2.5B**, Schlieren texture with typical 4- and 2-branches defects).[24]

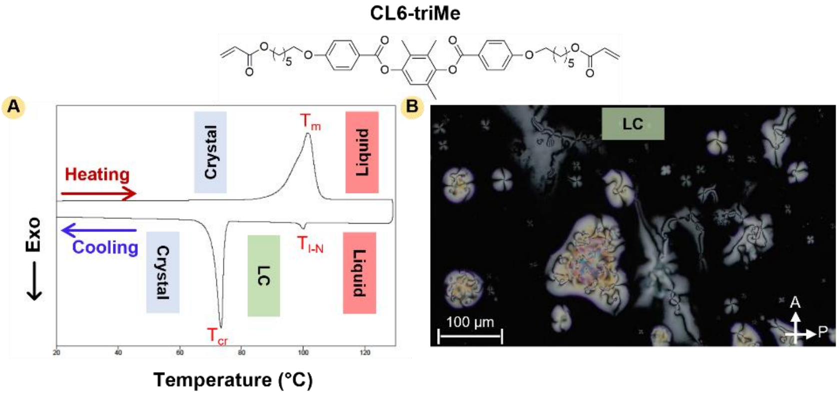

Figure 2.5: Mesomorphic properties of CL6-triMe LC crosslinker. A) DSC trace of the second heating-cooling (20°C/min) cycle; B) Representative POM images of the nematic phase.

The same analysis for the other molecules is reported in the Appendix while the transition temperatures are summarised in **Figure 2.6** and **Table 2.2**.

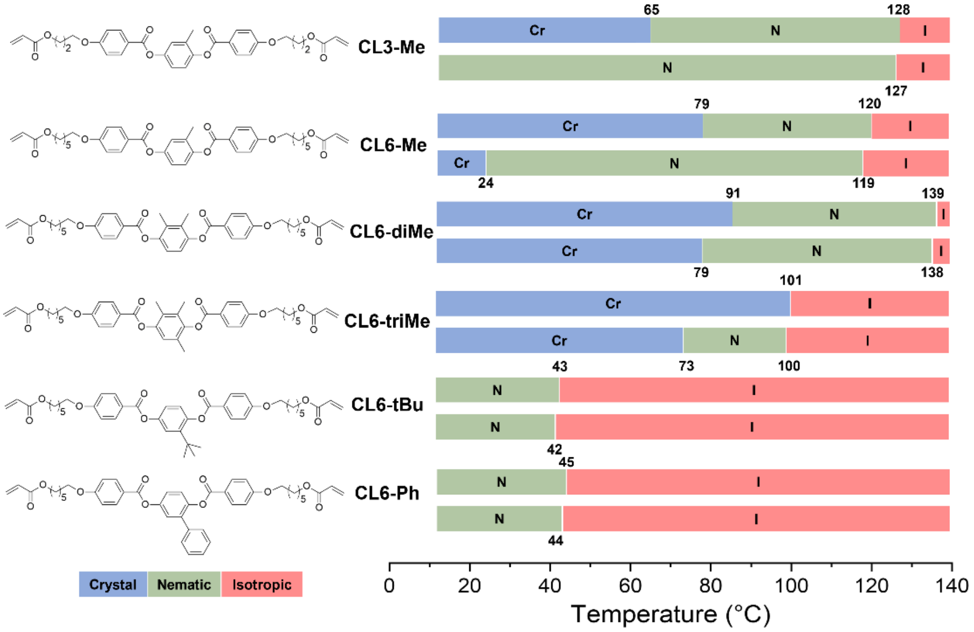

Figure 2.6: Thermal properties of crosslinkers obtained during the second heating (h) – cooling (c) cycle of DSC experiments (20 °C/min); Cr: crystalline phase; N: nematic phase; I: isotropic phase. All Temperatures are taken at the maximum of the transition peak.

All the molecules exhibited enantiotropic behaviour, with nematic phase observed both on heating and cooling, except for CL6-triMe, which displays the LC phase only during the cooling step (monotropic behaviour). Within the series of methyl substituted crosslinkers, we observed that melting temperature decreases as the number of methyl substituents increases while clearing temperature does not follow a trend with the substituent number. This behaviour was already observed with similar molecules but containing different polymerizable groups.[49]

Table 2.2: Thermal properties of crosslinkers obtained during the second heating (h) – cooling (c) cycle of DSC experiments (20 °C/min). Cr: crystalline phase; N: nematic phase; I: isotropic phase. All Temperatures are taken at the maximum of the transition peak. *After the first cycle of heating and cooling a cold crystallisation was observed at 47 °C.

Crosslinker	Phase transition temperature [°C]
CL3-Me	h: Cr_1 62 Cr_2 65 N 128 I c: I 127 N *
CL6-Me	h: Cr 85 N 120 I c: I 119 N 24 Cr
CL6-diMe	h: Cr 91 N 139 I c: I 138 N 79 Cr
CL6-triMe	h: Cr 101 I c: I 100 N 73 Cr
CL6-tBu	h: N 45 I c: I 44 N
CL6-Ph	h: N 43 I c: I 42 N

By insertion of the bulkier phenyl and *tert*-butyl substituents, a further clearing temperature reduction is achieved and, very interestingly, both crosslinkers maintain the LC phase even at room temperature with suppression of the crystallisation process for several days. On the contrary, all methyl substituted molecules with 6 carbon atoms exhibit an exothermic crystallisation process during cooling. This overall characterization demonstrates our initial hypothesis: the introduction of bulky substituents reduces the clearing temperatures and prevents the crystallisation processes. Both requirements allow for an easier material manipulation and fabrication process. Indeed, it is well known how room temperature LCs are preferred for processing by 3D printers or lithographic techniques.[97]

2.3 Conclusion

In this chapter the synthesis of new liquid crystalline crosslinkers, possessing bulky substituent in their LC core was described. Starting from previous research, such molecular modification provides a powerful tool to modulate the thermal and liquid crystalline properties of the final material produced. The insertion of this substituent (e.g. dimethyl, trimethyl, tert-butyl and phenyl group) was carried out in two different reaction pathways and a complete study on the yield of different pathways was reported. The molecular structure of this palette of acrylate based liquid crystalline crosslinkers was pinpointed using magnetic nuclear resonance characterization, while the thermal and optical (LC behaviours) properties were analysed contemporary to demonstrate the LC features of the new palette, together with their transition temperatures. As previously supported and demonstrated, the molecular modification of the LC core of calamitic crosslinkers can be used to tune the LC properties (e.g., optical and thermal). Moreover, these aspects were deeply analysed in the realisation of different LCNs for the production of smart actuators to be applied in the field of artificial muscles on one hand and on the other hand in innovative application for micro-mechanical actuators. These aspects will be presented in the next Chapters of the manuscript.

2.4 Experimental section

All reagents and solvents were commercially available, used as received and listed in **Table 2.3** All reactions were carried out under magnetic stirring and monitored by TLC on 0.25 mm silica gel plates (Merck F254). Chromatographic purifications were carried out on silica gel (230–400 mesh, Sigma-Aldrich) or on alumina (Brockman I, 58 Å pore size, Sigma-Aldrich). NMR spectra were recorded with a Varian Gemini 200 MHz or with a Varian Mercury 400 MHz at 25 °C. The chemical shift values (δ) are reported in ppm and are relative to the TMS signal (δ = 0.00 ppm); the notations s, d, t, m, Ar indicate respectively: singlet, doublet, triplet, multiplet, aromatics.

Table 2.3: Data information for the reagents used for the synthesis of diacrylate substituted crosslinkers.

Product	Cas number	Supplier
6-chloro-1-hexanol	2009-83-8	Sigma-Aldrich
acryloyl chloride	814-68-6	Sigma-Aldrich
N-Methyl-2-pyrrolidone (NMP)	872-50-4	Sigma-Aldrich
N,N'-dicyclohexyilcarbodiimide (DCC)	538-75-0	Sigma-Aldrich
1-Ethyl-3-(3-dimethylaminopropyl)carbodiimide (EDC)	25952-53-8	Sigma-Aldrich
RM257 (CL3-Me)	174063-87-7	Sigma-Aldrich
RM82 (CL6-Me)	125248-71-7	Sigma-Aldrich

Mesomorphic properties characterization: phase transition temperature of monomers were measured using a DSC TA Instruments Calorimeter Q-2000 (TA Instruments, Milan, Italy) in a nitrogen atmosphere (heating and cooling rate: 20 °C/min). Polarised Optical microscopy was performed with an inverted microscope (Zeiss Axio Observer A1) in cross-polarized mode equipped with a Linkam PE120 hot stage and an Axio camera to obtain pictures of the LC textures. More information can be found in the appendix.

Synthesis of 4-[(6-hydroxyhexyl)oxy]benzoic acid (2)

4-hydroxy benzoic acid (**1,** 5.0 g, 37 mmol) was dissolved in a mixture of ethanol (35 mL) and water (7 mL) in a 250 mL flask. Then, 6-chlorohexanol (7.6 g, 55 mmol), potassium iodide (4.0 g, 24 mmol) and potassium hydroxide (6.22 g, 111 mmol) were added, and the reaction was left at reflux for 18 h. After evaporation under reduced pressure, the resulting white solid was dissolved in water and impurities extracted with diethyl ether (50 mL). The aqueous phase was acidified with 10 mL of hydrochloric acid (1 M) to give a white precipitate. After filtration and drying, product **2** was obtained with a 86% yield (7.6 g, 32 mmol) and used for the next step without further purification.

^{1}H-NMR of **2** (400 MHz, CD$_3$OD): δ= 7.95-7.93 (m, 2H, Ar-**H**), 6.96-6.94 (m, 2H, Ar-**H**), 4.04 (t, J = 6.4 Hz Hz, 2H, -ArOC**H**$_2$-), 3.56 (t, J=6.5 Hz, 2H, C**H**$_2$OH), 1.84-1.77 (m, 2H, -C**H**$_2$- aliphatic), 1.59-1.41 (m, 6H, -C**H**$_2$-aliphatic) ppm.

^{13}C-NMR of **2** (400 MHz, CD$_3$OD): δ= 168.36 (-**C**OOH), 163.11(1C, Ar), 134.45 (2C, Ar), 124.76 (1C, Ar), 113.71 (2C, Ar), 67.77 (-**C**H$_2$OAr-), 61.44 (-**C**H$_2$OH-), 32.16 (-**C**H$_2$ aliphatic), 28.81 (-C**H**$_2$ aliphatic), 25.52 (-**C**H$_2$ aliphatic), 25.26 (-**C**H$_2$ aliphatic) ppm.

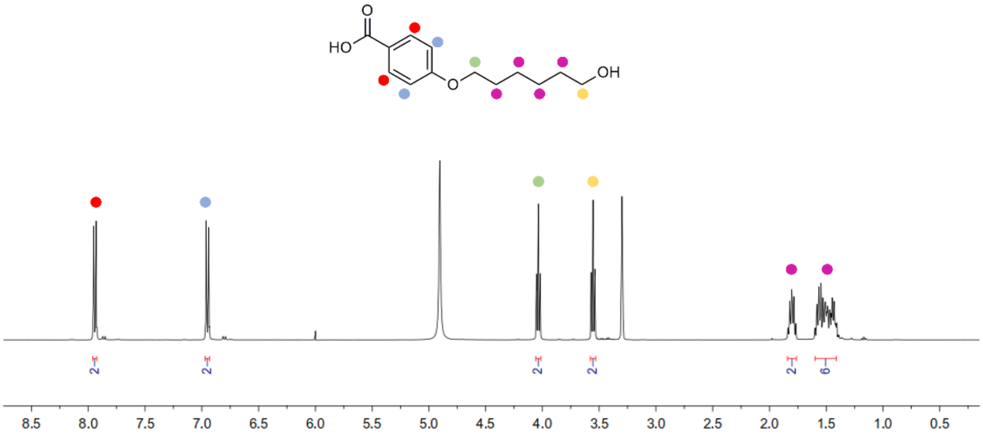

Figure 2.7: ^{1}H-NMR of 2.

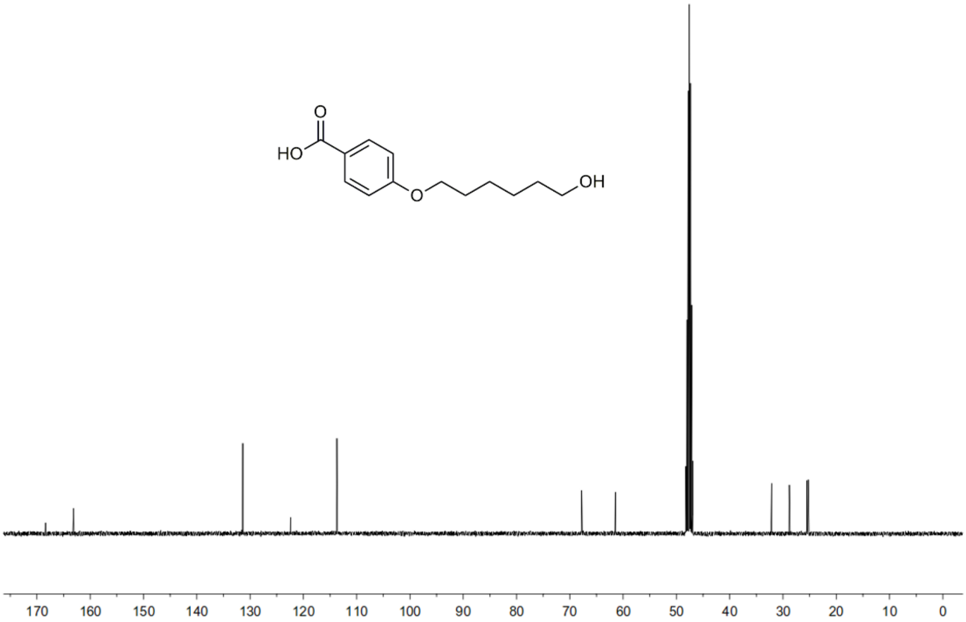

Figure 2.8: ^{13}C-NMR of 2.

Synthesis of 4-((6-(acryloyloxy) hexyl)oxy)benzoic acid (3)

To a solution of **2** (4.1 g, 20.9 mmol) in 40 mL of N-Methyl-2-pyrrolidone (NMP), acryloyl chloride (2.27 g, 25.1 mmol) was added dropwise and the mixture was stirred at room temperature for 3 h. Then, water was added to give a white precipitate that was filtered and washed thoroughly with water to afford the pure product in quantitative yield (5.2 g, 20.9 mmol)

^{1}H-NMR of **3** (400 MHz, $CDCl_3$): δ = 8.06-8.04 (m, 2H, Ar-**H**), 6.94-6.92 (m, 2H, Ar-**H**), 6.39 (dd, J=17.4, 1.5 Hz, 1H, CH=C$\mathbf{H_2}$), 6.12 (dd, J= 17.3, 10.4 Hz , 1H, C**H**=CH_2), 5.82 (dd, J= 10.4, 1.5 Hz, 1H, CH=C$\mathbf{H_2}$), 4.18 (t, J= 6.6 Hz, 2H, -ArOC$\mathbf{H_2}$-), 4.03 (t, J= 6.4 Hz, 2H, -C$\mathbf{H_2}$OCO-) 1.86-1.79 (m, 2H, -C$\mathbf{H_2}$- aliphatic), 1.76-1.69 (m, 2H, -C$\mathbf{H_2}$- aliphatic), 1.56-1.42 (m, 4H,-C$\mathbf{H_2}$- aliphatic) ppm.

^{13}C-NMR of **3** (400 MHz, $CDCl_3$): δ = 166.30 (**C**OCH=CH_2), 163.55 (Ar), 132.31 (CH=**C**H_2), 130.53 (2C, Ar), 128.54 (**C**H=CH_2), 121.37 (1C, Ar), 114.16 (2C, Ar), 68.02 (**C**H_2OAr), 64.45 (-**C**H_2OCO-), 28.96 (-**C**H_2- aliphatic), 28.53 (-**C**H_2- aliphatic), 25.70 (-**C**H_2- aliphatic), 25.65 (-**C**H_2-aliphatic) ppm.

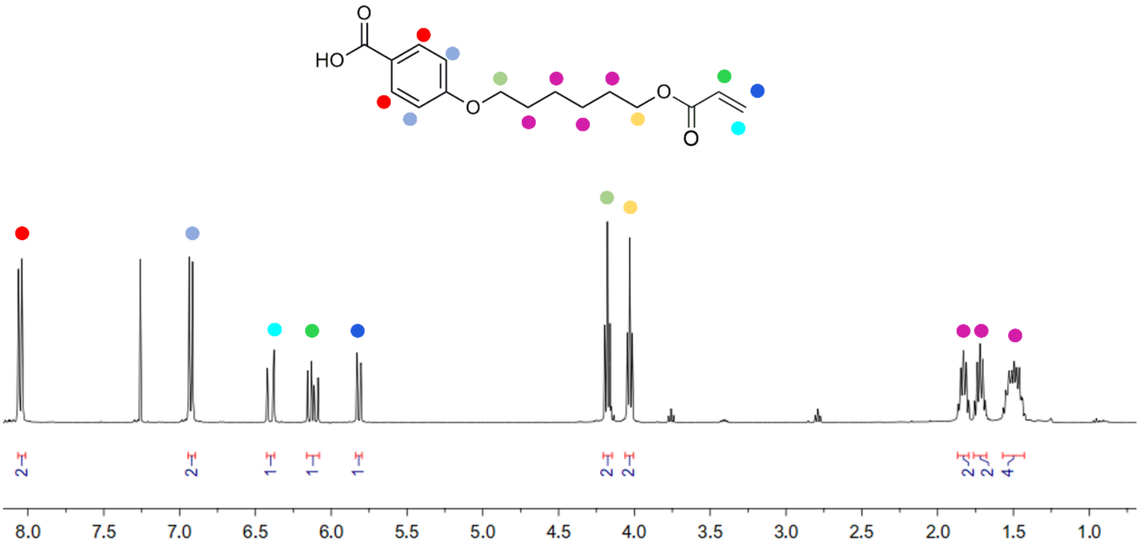

Figure 2.9: ^{1}H-NMR of 3.

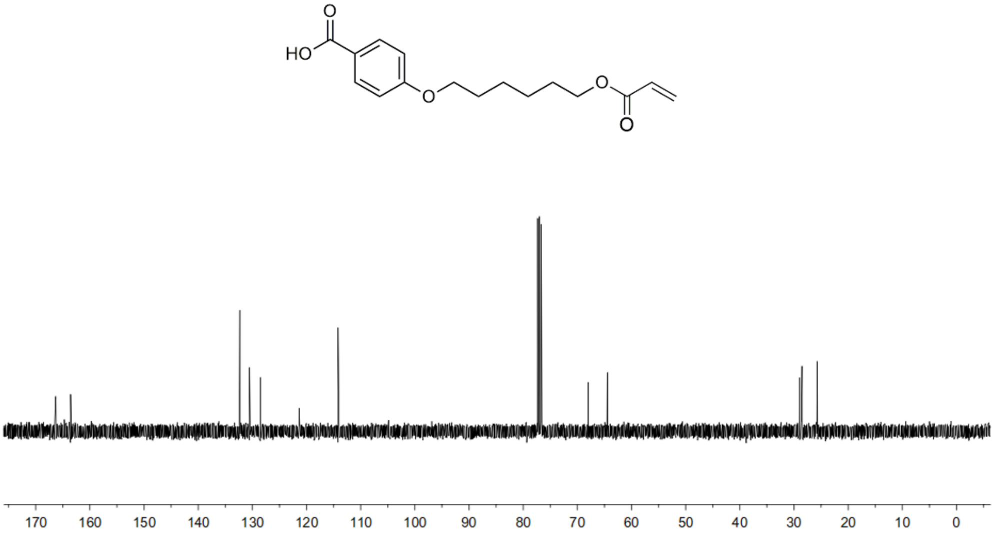

Figure 2.10: ^{13}C-NMR of 3.

Synthesis of 2,3-dimethyl-1,4-phenylene bis(4-((6-(acryloyloxy)hexyl)oxy)benzoate) (CL6-diMe)

In a 250 mL flask, **3** (2.0 g, 6.85 mmol), 2,3-dimethylhydroquinone (0.48 g, 3.42 mmol), DCC (1.55 g, 7.53 mmol) and DPTS (4 g, 13.70 mmol) were dissolved in anhydrous dichloromethane (50 mL). The reaction was stirred at 50 °C for 72 h. After filtering the crude, the organic phase was washed with 12 mL of water, 12 mL of a 5% wt solution of acetic acid and then 12 mL of water. The combined organic layers were dried on Na_2SO_4 and evaporated under reduced pressure. The crude was crystallised in ethanol providing **CL6-diMe** (3.26 g, 2.18 mmol) as powder white solid with a 63% yield.

^{1}H-NMR of **CL6-diMe** (400 MHz, $CDCl_3$): δ = 8.18-8.16 (m, 4H, Ar-**H**), 7.03 (s, 2H, Ar-**H**), 6.99-6.97 (m, 4H, Ar-**H**), 6.41 (dd, J= 17.3, 1.5 Hz, 2H, CH=C**H**$_2$), 6.13 (dd, J= 17.3, 10.4 Hz, 2H, C**H**=CH$_2$), 5.83 (dd, J= 10.4, 1.5 Hz, 2H,CH=C**H**$_2$), 4.19 (t, J= 6.6 Hz, 4H, ArOC**H**$_2$), 4.06 (t, J= 6.4 Hz, 4H, C**H**$_2$COCH=CH$_2$), 2.16 (s, 6H, -C**H**$_3$), 1.88-1.81 (m, 4H, -C**H**$_2$ - aliphatic), 1.77-170 (m, 4H, -C**H**$_2$ - aliphatic), 1.54-1.43 (m, 8H, -C**H**$_2$ - aliphatic) ppm.

^{13}C-NMR of **CL6-diMe** (400 MHz, $CDCl_3$): δ = 166.31 (2C, **C**OCH=CH$_2$), 164.76 (2C, Ar**C**OO), 163.43 (2C, Ar), 147.01 (2C, Ar), 132.28 (2C, CH=**C**H$_2$), 130.62 (6C, Ar), 128.53 (2C, **C**H=CH$_2$), 121.48 (2C, Ar), 120.08 (2C, Ar), 114.30 (4C, Ar), 68.06 (2C, **C**H$_2$OAr), 64.46 (2C, **C**H$_2$OCO-), 28.97 (2C, -**C**H$_2$- aliphatic), 28.53 (2C, -**C**H$_2$- aliphatic), 25.70 (4C, -**C**H$_2$- aliphatic), 13.14 (2C, -CH$_3$).

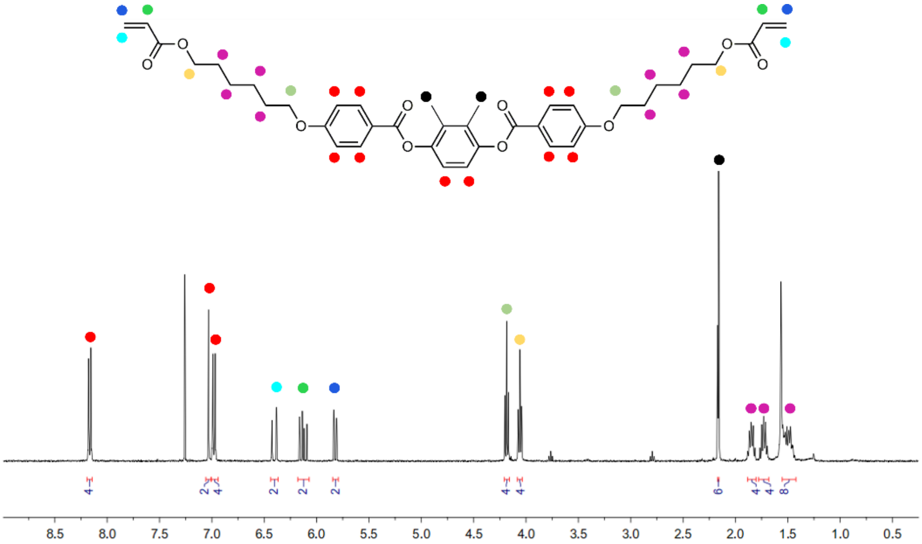

Figure 2.11: ^{1}H-NMR of CL6-diMe.

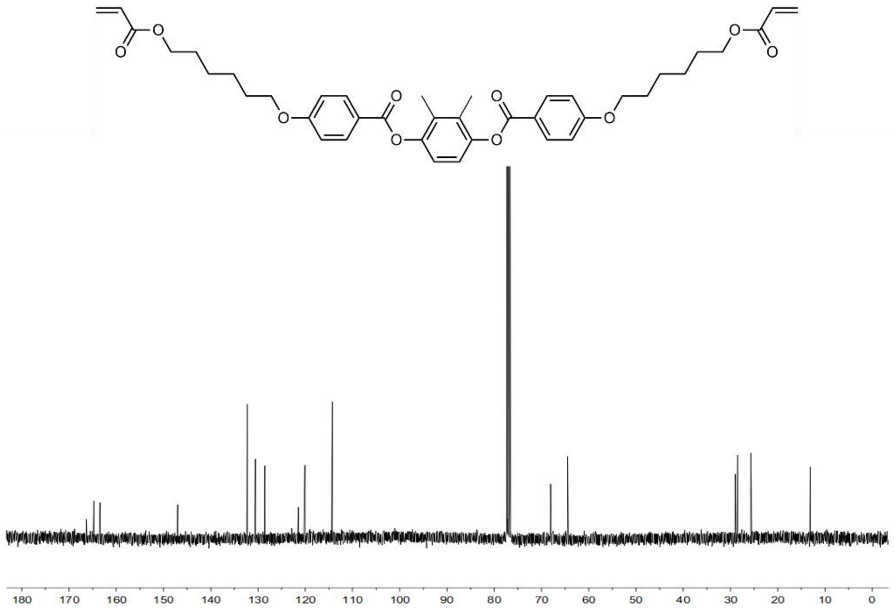

Figure 2.12: ^{13}C-NMR of CL6-diMe.

Synthesis of 2,3,5-trimethyl-1,4-phenylene bis(4-((6-(acryloyloxy)hexyl)oxy)benzoate) (CL6-triMe)

In a 100 mL flask, **3** (1.2 g 4.10 mmol), 2,3,5-trimethylhydroquinone (0.31 g, 2 mmol), DCC (0.93 g, 4.50 mmol) and DPTS (2.4, 8.2 mmol) were dissolved in in anhydrous DCM (25 mL). The reaction was stirred at 50 °C for 72 h. After filtering the crude, the organic mixture was washed with 12 mL of water, 12 mL of a 5% wt solution of acetic acid and then 12 mL of water. The combined organic layers were dried on Na_2SO_4, evaporated under reduced pressure and the crude crystallised in ethanol providing **CL6-triMe** (0.78 g, 1.12 mmol) as powder white solid with a 56% yield.

^{1}H-NMR of **CL6-triMe** (400 MHz, $CDCl_3$): δ = 8.20-8.15 (m, 4H, Ar-**H**), 7.00-6.96 (m, 4H, Ar-**H**), 6.91 (s, 1H, Ar-**H**), 6.40 (dd, J= 17.3, 1.1 Hz, 2H, CH=C**H**$_2$), 6.12 (dd, J= 17.3, 10.4 Hz, 2H, C**H**=CH$_2$), 5.82 (dd, J= 10.4, 1.1 Hz, 2H, CH=C**H**$_2$), 4.18 (t, J= 6.6 Hz, 4H, ArOC**H**$_2$), 4.06 (t, J= 6.2, 4.7 Hz,4H, C**H**$_2$OCOCH=CH$_2$), 2.16 (s, 3H, -C**H**$_3$), 2.12 (s, 6H, -C**H**$_3$), 1.86-1.81 (m, 4H, C**H**$_2$- aliphatic), 1.76-1.69 (m, 4H, C**H**$_2$- aliphatic), 1.58-1.43 (m, 8H, C**H**$_2$- aliphatic) ppm.

^{13}C-NMR of **CL6-triMe** (400 MHz, $CDCl_3$): δ = 166.30 (2C, **C**OCH=CH$_2$), 164.87 (2C, Ar**C**OO), 164.22 (2C, Ar), 163.39 (2C, Ar), 146.73 (2C, CH=**C**H$_2$), 145.87 (4C, Ar), 132.29 (1C,Ar), 130.57 (2C, **C**H=CH$_2$), 128.53 (1C, Ar), 127.72 (1C, Ar), 123.96 (2C**,** Ar), 121.42 (1C, Ar), 114.28 (4C, Ar), 68.06 (2C, **C**H$_2$OAr), 64.46 (2C, **C**H$_2$OCOCH=CH$_2$), 28.97 (2C, -**C**H$_2$-aliphatic), 28.53 (2C, -**C**H$_2$-aliphatic), 25.69 (4C, -**C**H$_2$-aliphatic), 16.40 (1C, -**C**H$_3$), 13.28 (1C, -**C**H$_3$-), 12.92 (1C, -**C**H$_3$-).

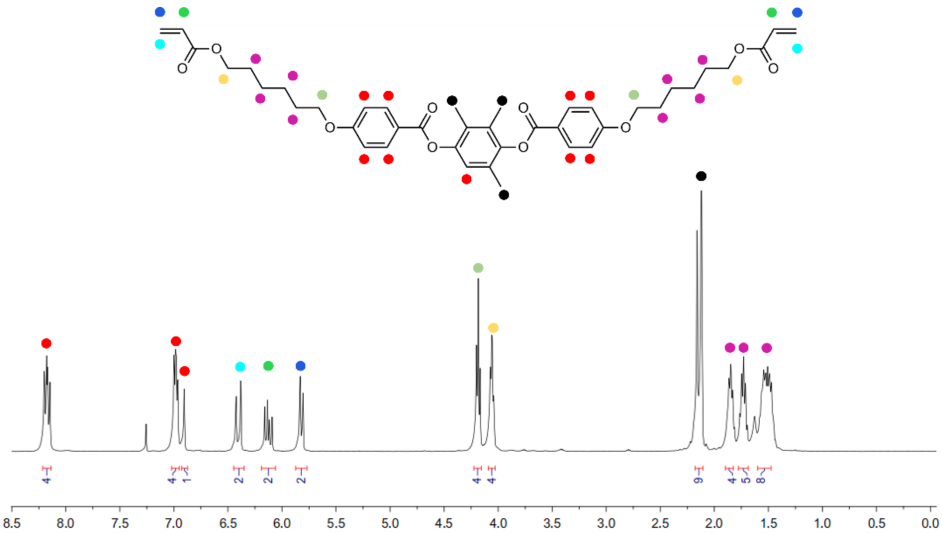

Figure 2.13: ^{1}H-NMR of CL6-triMe.

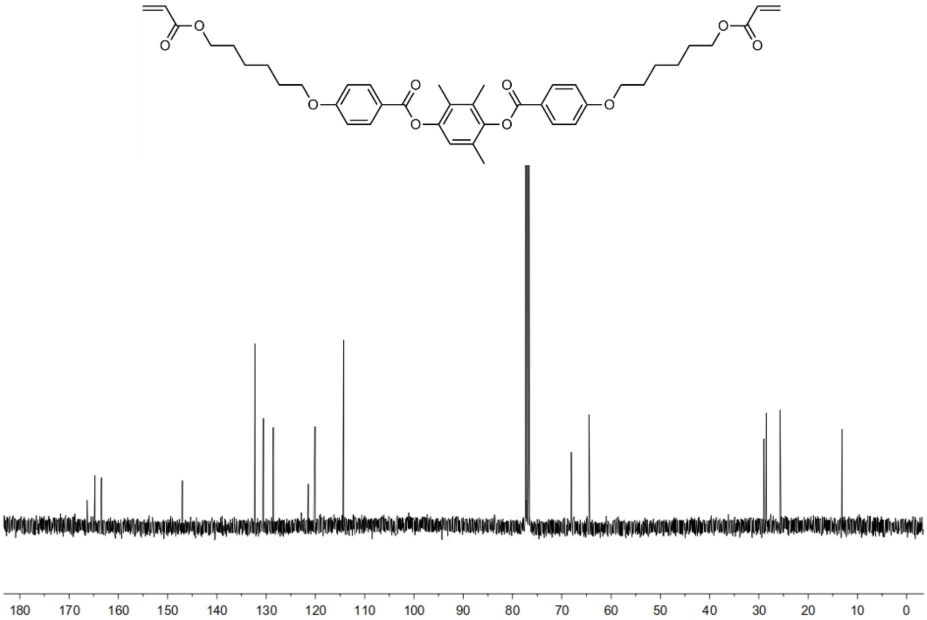

Figure 2.14: ^{13}C-NMR of CL6-triMe.

Synthesis of 2-(tert-butyl)-1,4-phenylene bis(4-((6-(acryloyloxy)hexyl)oxy)benzoate) (CL6-tBu)

In a 25mL flask **3** (0.50 g,1.70 mmol), 2-(*tert*-butyl)hydroquinone (0.14 g, 0.86 mmol), DCC (0.39 g, 1.89 mmol), DPTS (1 g, 3.45 mmol) were dissolved anhydrous DCM (10 mL). The reaction was stirred at 50°C for 72 h. After filtering the crude, the organic mixture was washed with 12 mL of water, 12 mL of a 5% wt solution of acetic acid and then 12 mL of water was extracted. The combined organic layers were dried on Na_2SO_4, evaporated under reduced pressure and the crude crystallised in ethanol providing **CL6-tBu** (0.30 g, 0,42 mmol) as powder white solid with a 49% yield.

^{1}H-NMR of **CL6-tBu** (400 MHz, DMSO-d_6): δ = 8.08-8.04 (m, 4H, Ar-**H**), 7.23-7.07 (m, 7H, Ar-**H**), 6.30 (dd, J = 17.3, 1.5 Hz, 2H, CH=C**H**$_2$), 6.14 (dd, J =17.3,10.3 Hz, 2H, C**H**=CH$_2$), 5.90 (dd, J = 10.3,1.2 Hz, 2H, CH=C**H**$_2$), 4.09 (s, 8H, -C**H**$_2$O-), 1.86–1.38 (m, 16H, ,-**C**H$_2$- aliphatic), 1.28 (s, 9H, -**C**H$_3$) ppm.

^{13}C-NMR of **CL6-tBu** (400 MHz, DMSO-d_6): δ = 165.95 (2C, **C**OCH=CH$_2$), 164.80 (2C, Ar**C**OO), 163.74 (2C, Ar), 148.29 (2C, Ar), 146.82 (1C, Ar), 142.74 (1C, Ar), 132.46 (1C, Ar), 131.78 (2C, CH=**C**H$_2$), 128.83 (2C, **C**H=CH$_2$), 125.87 (3C, Ar), 121.32 (1C, Ar), 121.03 (1C, Ar), 115.36 (4C, Ar), 115.19 (1C, Ar), 110.48 (1C, Ar), 68.35 (2C, **C**H$_2$OAr), 64.46 (2C, **C**H$_2$OCOCH=CH$_2$), 30.22 (s, 4C, tert-butyl), 28.81 (2C, -**C**H$_2$-aliphatic), 28.47 (2C, -**C**H$_2$-aliphatic), 25.57 (4C, -**C**H$_2$-aliphatic).

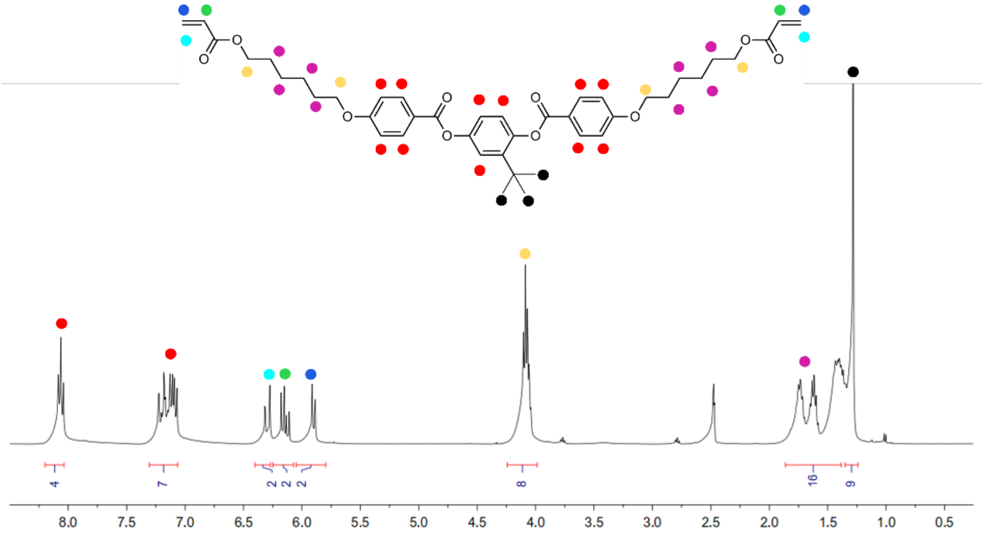

Figure 2.15: ^{1}H-NMR of CL6-tBu.

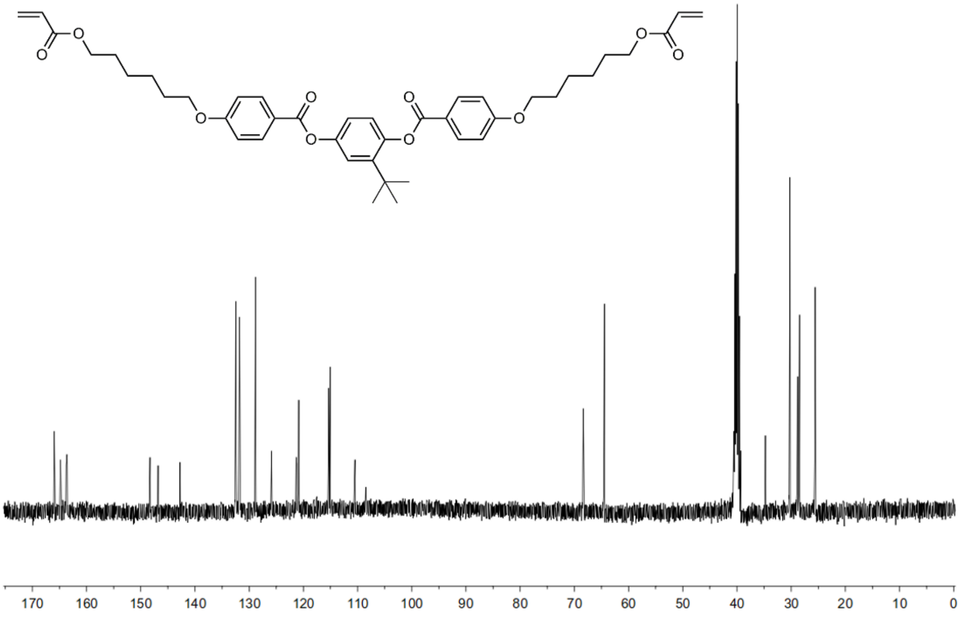

Figure 2.16: ^{13}C-NMR of CL6-tBu.

Synthesis of [1,1'-biphenyl]-2,5-diyl bis(4-((6-(acryloyloxy) hexyl) oxy) benzoate) (CL6-Ph).

In a 25mL flask **3** (0.50 g, 1.7 mmol), 2-phenylhydroquinone (0.16 g, 0.85 mmol), DCC (0.39 g, 1.87 mmol), DPTS (1 g, 3.45 mmol) were dissolved anhydrous DCM (8 mL). The reaction was stirred at 50 °C for 72 hours. After filtering the crude, the organic mixture was washed with 12 mL of water, 12 mL of a 5% wt solution of acetic acid and then 12 mL of water was extracted. The combined organic layers were dried on Na_2SO_4, evaporated under reduced pressure and the crude crystallised in ethanol providing **CL6-Ph** (0.34 g, 0.46 mmol) as powder white solid with a 54% yield.

^{1}H-NMR of **CL6-Ph** (400 MHz, DMSO-d_6): δ = 8.08-8.06 (m, 2H, Ar-**H**), 7.93-7.91 (m, 2H, Ar-**H**), 7.48-7.46 (m, 2H, Ar-**H**), 7.42-7.40 (m, 2H, Ar-**H**), 7.36-7.34 (m, 1H, Ar-**H**), 7.34-7.30 (m, 2H, Ar-**H**), 7.29-7.26 (m, 1H, Ar-**H**), 7.10-7.08 (m, 2H, Ar-**H**), 7.02-7.00 (m, 2H, Ar-**H**), 6.29 (dd, *J* = 17.3, 1.7 Hz, 2H, CH=C**H**$_2$), 6.14 (dd, *J* = 17.3, 1.7 Hz, 2H, C**H**=CH$_2$), 5.90 (dd *J* = 10.3, 1.7 Hz, 2H, CH=C**H**$_2$), 4.11-4.07 (m, 4H, ArOC**H**$_2$), 4.07–4.00 (m, 4H, C**H**$_2$COCH=CH$_2$), 1.77-1.68 (m, 4H, -C**H**$_2$ - aliphatic), 1.66-1.57 (m, 4H, , -C**H**$_2$ - aliphatic), 1.46-1.32 (m, 8H, -C**H**$_2$ - aliphatic).

^{13}C-NMR of **CL6-Ph** (400 MHz, DMSO-d_6): δ = 165.97 (s, **C**OCH=CH$_2$), 164.42 (s, Ar**C**OO), 163.67 (2C, Ar), 148.90 (2C, Ar), 145.46 (s, 1C, Ar), 136.49 (s, 1C, Ar), 135.71 (2C, CH=**C**H$_2$), 132.38 (4C, Ar), 131.80 (2C, Ar), 129.03 (2C, Ar), 128.82 (1C, Ar), 128.30, 124.96 (2C, **C**H=CH$_2$), 124.17 (1C, Ar), 122.53 (2C, Ar), 121.10 (1C, Ar), 120.85 (1C, Ar), 115.10 (4C, Ar), 68.29 (2C, **C**H$_2$OAr), 64.46 (2C, **C**H$_2$OCOCH=CH$_2$), 28.80 (2C, -**C**H$_2$-aliphatic), 28.46 (2C, -**C**H$_2$-aliphatic), 25.64 (4C, -**C**H$_2$-aliphatic).

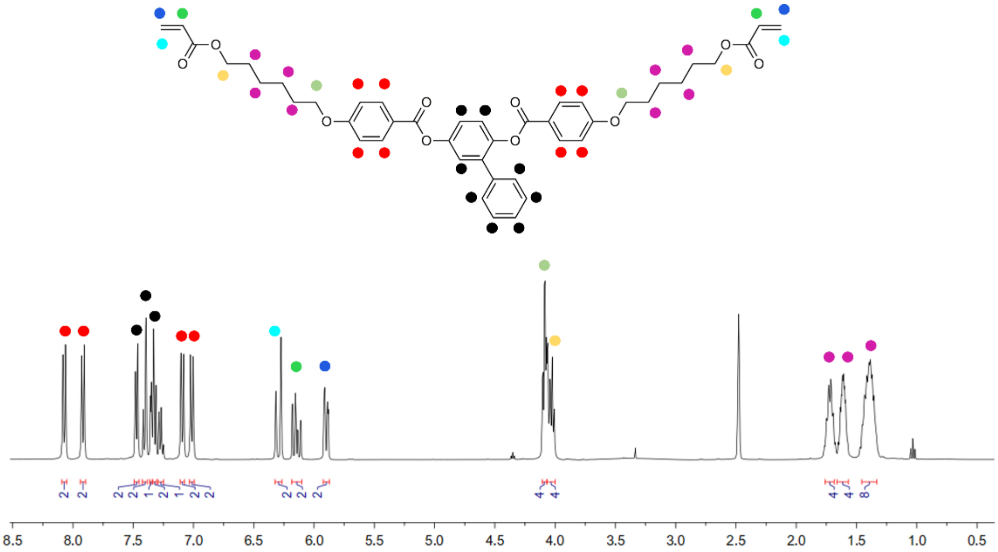

Figure 2.17: ^{1}H-NMR of CL6-Ph.

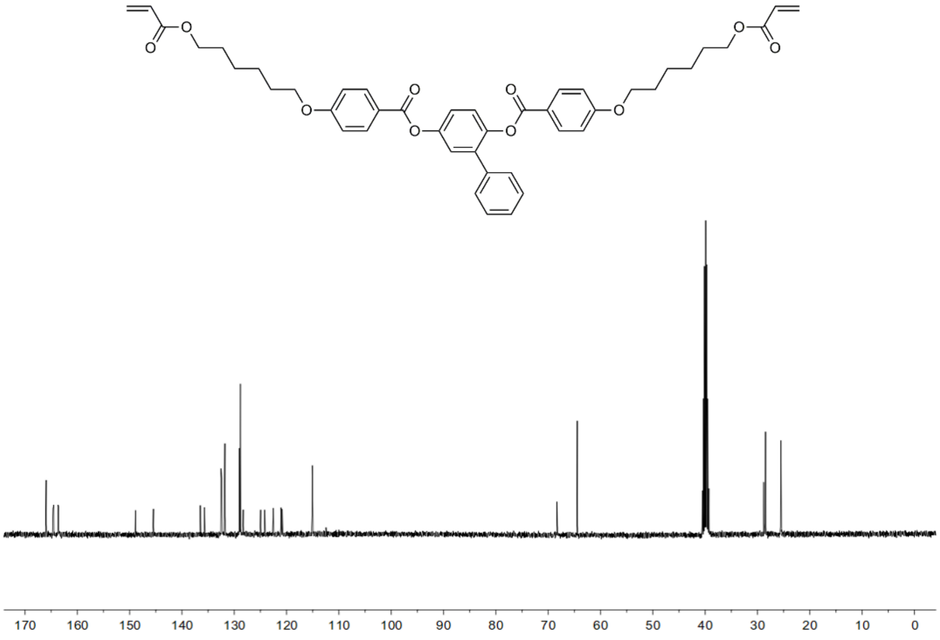

Figure 2.18: ^{13}C-NMR of CL6-Ph.

Chapter 3

Liquid Crystalline Networks as artificial muscles

3.1 Introduction

3.1.1 Cardiovascular diseases and Ventricular assist devices (VADs)

Cardiovascular diseases are still one of the leading causes of mortality worldwide. Among cardiovascular diseases, particular attention should be paid to heart failure (HF) defined as the failure of the heart to pump blood properly, and thus the inability to supply the correct balance of oxygen and nutrients to the rest of the human body.[98] HF can be a consequence of Myocardial Infarction (MI) which is the sudden stop of blood flow to a part of the heart, accompanied by the damage of the heart tissue, and necrosis. Over the last century, several studies have been carried out to collect data on heart failure causes, the so-called risk factors, the public costs for their treatment, and the difficulties of healthcare facilities. HF is a complex clinical syndrome resulting from malfunctions that can be determined by any structural and functional malfunction of blood pumping. It reduces life expectancy in affected patients and provides for the inability to live a healthy life contributing to the onset of other diseases.[99] In Italy, cardiovascular disease accounts for 44% of the causes of death as well as 23% of the national health care expenditure to care for those with heart disease, which remains chronic even though it can be alleviated.[100] As a general statistic, more than 65 million people in the world are still affected by chronic cardiovascular diseases, and unlike other diseases, the road to a total resolution of these has not yet been found.

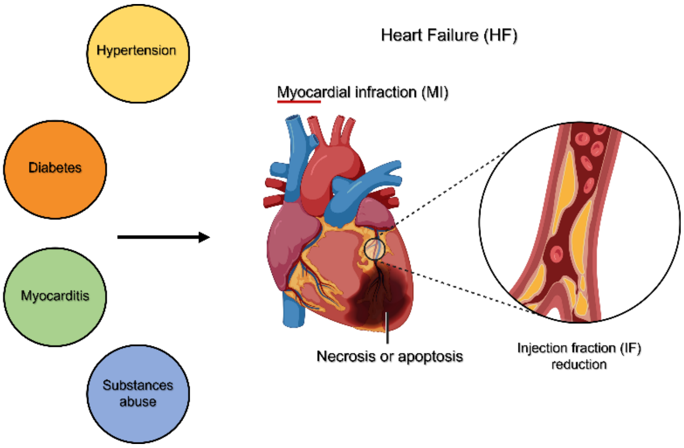

Figure 3.1: Physiological causes of Heart failure and necrosis of myocardial tissue.

Heart failure (HF), represented schematically in **Figure 3.1** is the final clinical presentation of a variety of cardiovascular diseases, such as coronary artery disease, hypertension, valvular heart disease, myocarditis, diabetes, or substance abuse (e.g. alcohol and drugs).[100] It includes an increase in the size of cardiomyocytes, loss of their contractile properties in both the systolic (i.e. contracting) and diastolic phases (which is the phase of cardiac tension), and expression of proteins normally observed in the embryonic phase.[101] Given the chronic, pathological and deadly state of heart failure to date, heart transplantation remains the only therapy capable of 'solving' this chronic condition. Differently, the conduction disease for the electrical potential developed by the heartbeat, which is the waveguide of the injection fraction (IF) of the blood to the muscles, can be managed using a common electrical assist device. The most used device is the pacemaker as represented in **Figure 3.2**.

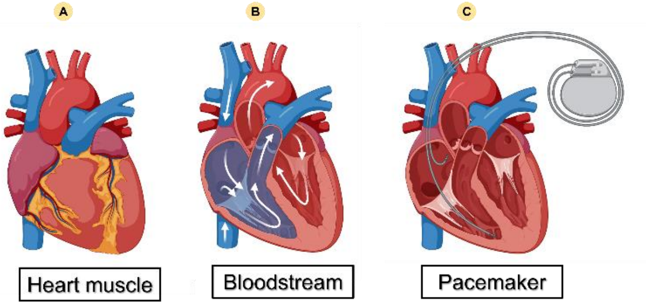

Figure 3.2: Heart schemes. A) Human heart muscle; B) Bloodstream pumped by the heart during the heartbeat cycle; C) Common example of assist device used for heart treatment.

Since the first heart transplantation performed 60 years ago by Dr. Christiaan Barnard, to date the progress made in the technique was incredible: innovative experiments to long-term clinical success have married prescient insights with discipline and organisation in the domains of surgical techniques, organ preservation, immunosuppression, organ donation and transplantation logistics, infection control, and long-term graft surveillance. More than 5000 successful heart transplants were performed worldwide in 2015. [102,103] But despite this, there are still difficulties to be solved. First of all, the number of transplants that can be performed is largely limited. The number of patients with advanced cardiovascular disease greatly exceeds the number of possible transplantable hearts. Moreover, the narrow exclusion criteria do not make transplantation a solution for all patients.[104] Given the difficulties in heart transplantation, many efforts have been made to produce alternative mechanical support technologies, included in the field of the so-called engineered heart tissues (EHTs) in which particular attention was done on ventricular assist devices (VADs). These can be implanted to one or both ventricular systems and their mechanical function is to pump the blood more easily. Ideally an assist device has to comply with three most relevant requirements [105]:

- Generation of tension to assist the cardiac contraction (20-50mN/mm^2);
- Material thickness (~ 1cm);
- Propagation of electrical pulses (with a rate of 25 cm s^{-1}).

Even with the technological development and evolution in the field of these systems, the disadvantages and risks associated with their use are not beneficial for cardiac assistance in many cases. Possible risks, all contributing to VAD failure in the clinical setting, can be bleeding and infections,[106] device malfunction, haemorrhage, thrombosis, and insufficient aftercare. Moreover, percutaneous driveline infection (PDI) is one of the most common causes of death with these devices, accounting for 47% of all left ventricular assist device (LVAD) unplanned readmissions.[107]

Based on the pros and cons in the use of VADs for cardiac mechanical assistance, the research concentrated on usable alternatives.

3.1.2 Artificial muscles able to mimic biological tissues

Starting from the base and analysing the heart muscle, this can be defined as a biological actuator. In fact, the heart muscle can perform movements, such as contraction and relaxation, together with physiological functions. Natural muscles in general, can provide billions of work cycles involving tension development movement and can change their strength and stiffness in response to several mechanical needs. Based on this assumption, scientific research has focused on the possibility, by means of tissue engineering and the production of artificial muscles, of replicating the properties of the human heart muscle in such a way as to be able to simulate the performance obtained by a biological muscle.[108]

Artificial muscles are soft materials able to perform actuations (e.g., movements) by converting external energy into mechanical motion. This movement can be produced externally thanks to the response of the material to an applied stimulus. [109,110] Ideally, actuators able to simulate or assist the heart muscle could also be used for valve assistance, fluid transport, and to increase the blood IF. [111] Producing artificial muscles that mimic heart function is not easy since there are many parameters to be reproduced by a synthetic material.[112] **Table 3.1** shows the typical mechanical parameters obtained for the cardiac muscle.[113]

Table 3.1: Physiological parameter of the human heart muscle.[113]

Cardiac tissue	
Strain [%]	5-20
Stress [KPa]	50-100
Work density [J Kg^{-1}]	4-7
Strain rate [% s^{-1}]	>80
Bandwith [Hz]	<10
Current [mA]	2

Myocardial strain is a principle for quantification of left ventricular (LV) function which is now feasible with echocardiography (ECG). [114] Stress, on the other hand, can vary between 60 and 100 KPa measured as the maximum of the systolic work, i.e., cardiac contraction, for the expulsion of blood from the ventricle.[115] The work density was related both to stress and strain curve obtained and is expressed in J Kg^{-1} which means that is the work produced for a unit of weight. Most important parameter that we have to consider is the response time. In the case of an actuator, it is the time needed to reach the desired actuation level or configuration. In the case of the heart, considering it as a purely blood pump, two kinetic parameters have to been analysed:

i) Systolic heartbeat (contraction): which is reached in 250 ms approximately;
ii) while the Diastolic heartbeat (expansion) is reached in 350 ms approximately.[116]

All the above-mentioned parameters have to be reproduced in the smart material to be used as artificial cardiac muscle. Among smart materials, LCNs are the most promising ones to mimic the natural behaviour of the human tissues and in the next paragraph their application in the biomedical field will be discussed.

3.1.3 Liquid crystalline networks as smart actuators for the diseased heart muscle

It has been pinpointed in the previous sections how, to mimic the human heart muscle, it is necessary to replicate its strength development, kinetic and stiffness. Therefore, this property has to be remotely modulable to fit the different conditions under which physiological muscles are involved. Thanks to their difference in the thermal expansion coefficient in parallel and perpendicular direction, with respect to the LC alignment, Liquid Crystalline Network (LCNs) present a reversible shape-change in response to stimuli once a specific molecular arrangement is set up in the materials.[117,118] By engineering the LC alignment, it is possible to obtain 3D deformations under different stimuli, while responsiveness to different stimuli can be induced by inserting specific molecules, and the material modification at molecular level allows to modulate important properties such as stiffness and kinetics of activation and relaxation.

In this section, the crosslinker modification at the molecular level described in the previous Chapter is further exploited towards the optimization of the LCN properties, and the development of light-responsive artificial muscles. The photopolymerizable crosslinkers reported in the previous Chapter were demonstrated able to strongly modulate the material mechanical properties, such as kinetics and maximum tension under light actuation, opening up to interesting materials for biomedical applications. In particular, this experimental work is part of the REPAIR project (granted by EU) aiming at developing devices able to support the mechanical function of diseased hearts. To this aim, LCN materials showing appropriate features are needed, and the understanding of the correspondence in between LCN composition and material behaviour has to be assessed. The first thing to do is to develop a protocol to understand if the artificial material actually responds as the natural muscle. In this view home-made set-ups were built up reproducing the one used to study natural muscles. [119,120] It consists of a force transducer and a motor coupled with the light source (**Figure 3.3**). The LCN strips under evaluation, cut to have dimensions typical of cardiac trabeculae (i.e., 8 mm in length x 1.6 mm in width x 0.01 mm in thickness), are mounted between a force transducer on top and a fixed end on the bottom to measure the force under isometric conditions setting different illumination patterns. Having demonstrated the possibility to modulate the tension by changing the light intensity, and the dependence of the dynamics of tension generation on the illumination pattern and the photo-responsive molecules used, two different illumination systems were settled. The first one is based on a wide illumination pattern using a LED lamp working at 540 nm (**Figure 3.3A**). The second one is based on a local illumination pattern, composed of an array of 4 mLEDs (470 nm and 540 nm for the two cases) (**Figure 3.3B**). To be noticed that all measurements are collected in isometric conditions by using on one end of the strip a weight much heavier than the material can lift up. Also, having a camera in the set-up, this easily allows to collect data in isotonic conditions (by changing the weight) and therefore to record the displacement produced by the strip in response to the illumination (contractile response). An assessment using different mesogen, crosslinkers and dyes allowed us to optimise a material able to produce approximately 385 mN/mm^2 of tension under a light power >100 mW/mm^2 [119]. Of particular interest was the comparison between two different dyes (D6 and Dispersed Red 1 acrylate named as DR1), which are responsible for the photo-actuation properties of the LCN.[121] Differently from Dye 6, which has an absorption in the green region (maximum absorption peak at 535 nm), DR1 has a strong absorption peak in the blue region at 470 nm, as shown by the UV-visible absorption spectrum shown in **Figure 3.3C** and is widely used in the literature for the production of photo-responsive LCNs.[122] In **Figure 3.3D** was proposed the comparison between the different illumination patterns using such two dyes. The efficiency (η) shown in **Equation 3.1** is the ratio of the mechanical work (product of the force (F) required to suspend the LCN strip and the strip displacement (ΔL) to the product of the light power (P) and illumination time defined as t_{ON}.

Equation 3.1

$$\eta = \frac{F * \Delta L}{P * t_{ON}}$$

In case of local illumination, the efficiency is ten times greater than using wide illumination. This effect can be determined by a focalisation of the stimulus which increases the contractile state of the material, as much as by a concurrent photo-thermal effect developed by the material which increases its mobility and thus actuation. The discriminating factor shown in the use of the local set-up is the possible and easier insertion into the cardiac muscle compared to common activation sources (LED lamps or lasers). Moreover, DR1 acrylate shows, in the same conditions of analysis, to increase the properties of actuation of the LCN.[121]

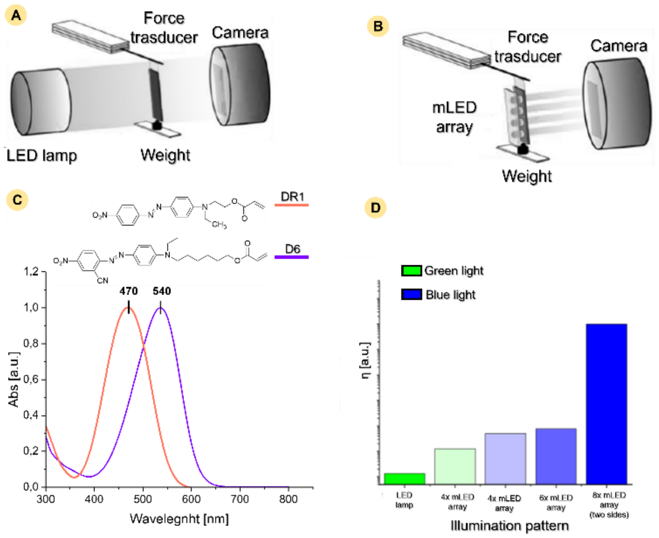

Figure 3.3: Illumination pattern general schemes, dye absorbance spectrum and determination of the efficiency. A) LED-lamp custom set-up B) mLED array customised set up C) UV-Vis spectra for the absorption of the two different dyes and relative maximum peaks of absorption D) Graph of the efficiency in different illumination patterns.

Following these recent achievements, in this chapter, we expand such research focussing on the optimization of side-chain LCNs prepared by acrylate polymerization, to understand how the introduction of different mesogenic cores in the crosslinker affects their mechanical properties and response to light irradiation.

3.2 Result and discussions

The LCNs analysed in this study are prepared with a monodomain homogeneous planar alignment which leads to a contraction along the alignment direction during the actuation (**Figure 3.4A**). The materials are easily synthesised in one step by photopolymerization starting from a mixture of acrylate-based mesogens, as described in **Chapter 2**. A typical composition used in previous studies [119,121] and taken here as reference is reported in **Figure 3.4B**. It includes a monoacrylate mesogens (C6BP), a diacrylate LC crosslinker (RM257, here called as CL3-Me to have a quicker understanding of the results) and an azobenzene dye Dispersed Red 1 acrylate (DR1-A). Starting from this formulation, we investigated the effect of the introduction of the new liquid crystalline crosslinkers described in **Chapter 2**, with the aim to modulate the phase transition temperatures and therefore the material efficiency.

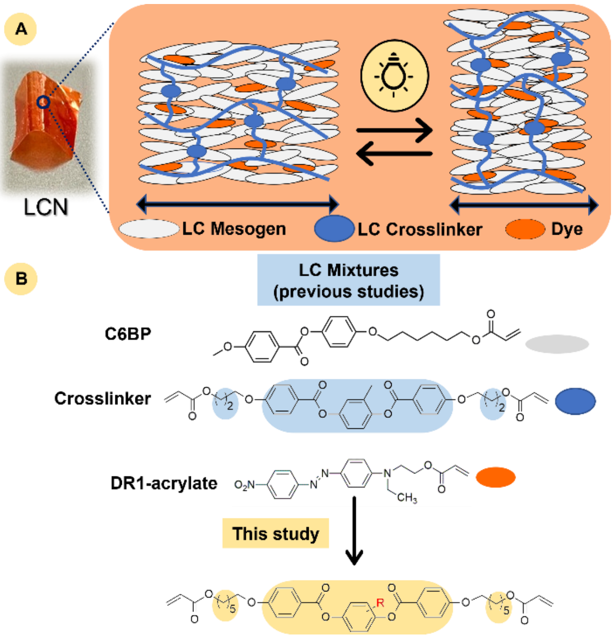

Figure 3.4: Structure of the LCNs. A) A photo-responsive LCN and a scheme of its molecular structure under actuation; B) Structure of the acrylate monomers used to prepare the materials.

3.2.1 LCN fabrication, optical and thermal properties

LCN films were prepared by photopolymerization of the monomeric mixture following the steps depicted in **Figure 3.5**. Briefly, the monomer mixtures were melted in the isotropic phase and infiltrated in LC cells assembled with glue by two glasses coated by polyvinyl alcohol (PVA) and rubbed in one direction with a velvet cloth (**Figure 3.5A-D**). This way, upon cooling the molecules down to the isotropic to nematic transition temperature, we obtained the formation of monodomain homogeneous planar alignments, and by irradiation with UV light, the simultaneous growth of the polymeric chain and their crosslinking were triggered. The so-prepared films were removed from the cell and used for the characterizations without other purification steps (**Figure 3.5G**).

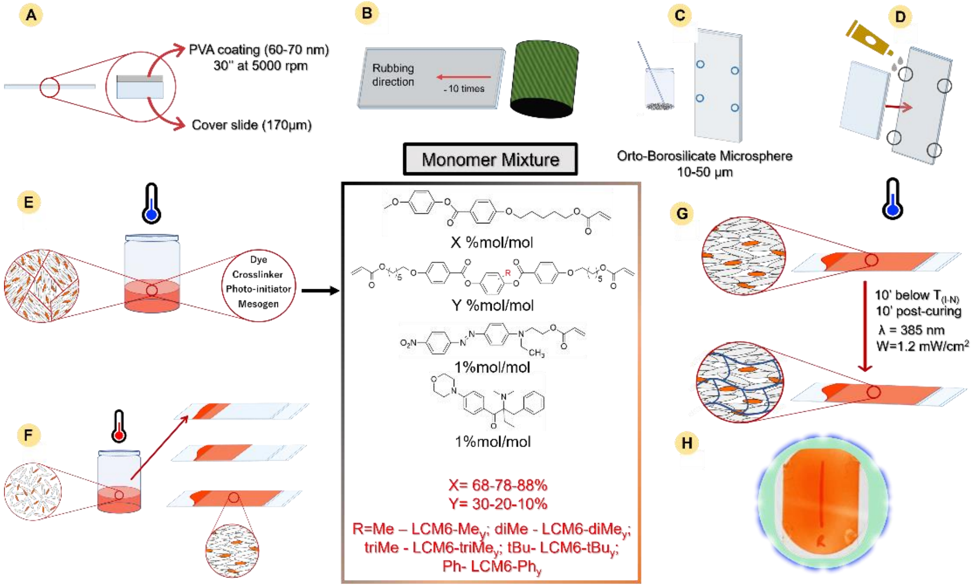

Figure 3.5: General scheme to produce thin film based on acrylate-LCNs. A) Glass slide coating with a sacrificial layer made with an aqueous solution of PVA. B) unidirectional mechanical rubbing with a velvet cloth on the coated slides; C) Deposition of the microspheres (10 µm in diameter) as spacers; D) Assembly of the cell with two glasses and glue deposition at the borders. E) Mix of monomers dissolved in solvent and dried under vacuum. F) Infiltration of the mixture in the LC cells. G) Photopolymerization process (UV lamp with λ= 385 nm and W= 1.2 mW/cm^2) of the material after having reached the nematic state of cooling. E) Example of the final LCN obtained after polymerization.

To highlight the role of the crosslinker structure, we prepared several mixtures having the same ratio (in mol/mol) for the different components but different crosslinker structure and then the formulations were increased in the content of the crosslinker (20 and 30%) to enhance the mechanical properties of the LCNs thin films only in the case of the methyl substituent and the phenyl one (since they were demonstrated to be the most performing ones). The presence of the DR1-A allows to control the material deformation by light. [97,123] Once the stimulus is switched off, the material returns in its initial state proving that the process is perfectly reversible for at least 20 days of alternated irradiation.[119] Transition temperatures of each mixture is reported in **Table 3.2** studied by DSC and POM. More information can be found in the Appendix. All mixtures showed a nematic phase on cooling and no crystallisation processes at room temperature for different days.

Table 3.2: Composition and thermal properties of the monomeric mixtures. All mixture contains 1% mol/mol of Irgacure 369 and 1% mol/mol or DR1 acrylate. Transition temperatures are determined during the second heating (h)–cooling (c) cycle of DSC experiments (20 °C/min) and taken at the maximum of the transition peak. Cr: crystalline phase; N: nematic phase; I: isotropic phase. *Percentage of crosslinker in the mixture, n=number of carbon atoms in the aliphatic spacer and m= substituent in the LC core of the crosslinker. **crystallisation was observed after the first cycle of heating-cooling (20°C/min).

Crosslinker (CLn-m$_y$)	Phase transition temperature [°C]
CL6-Me$_{10}$	h: Cr 40 N 54 I c: I 53 N
CL6-Me$_{20}$	h: Cr 29 N 66 I c: I 64 N 20 Cr**
CL6-Me$_{30}$	h: Cr 30 N 76 I c: I 75 N 23 Cr**
CL6-diMe$_{10}$	h: Cr 40 N 49 I c: I 48 N
CL6-triMe$_{10}$	h: Cr 40 N 50 I c: I 49 N
CL6-tBu$_{10}$	h: N 44 I c: I 42 N
CL6-Ph$_{10}$	h: N 43 I c: I 41 N
CL6-Ph$_{20}$	h: N 40 I c: I 40 N
CL6-Ph$_{30}$	h: N 43 I c: I 42 N

It is evident how the different molecular structure of the crosslinker can tune the thermal properties of the LC mixture realised. Even though it is difficult to obtain a linear trend for the different series of substituent utilised, it is evident that using the phenyl and the tert-butyl group as substituent can lead to a decrease of the nematic-to-isotropic phase transition temperature. Moreover, In the methyl and phenyl series, in which the content of the mesogenic crosslinker was increased, it is observable how only in the case of the methyl series the $T_{N\text{-}I}$ increase with the enhancement of the crosslinking degree.

To exclusively highlight the effect of the crosslinker structure, all the materials were photopolymerized in the same conditions: at 25 °C for 10 minutes, followed by a post-curing exposure at 45 °C to obtain a complete acrylate conversion.[124] Some POM images of a monodomain material at the end of the preparation process are shown in **Figure 3.6**, demonstrating the absence of optical defects and a transmittance dependence by the angle in between the polarizers and the nematic directors, as expected for a homogeneous planar alignment.

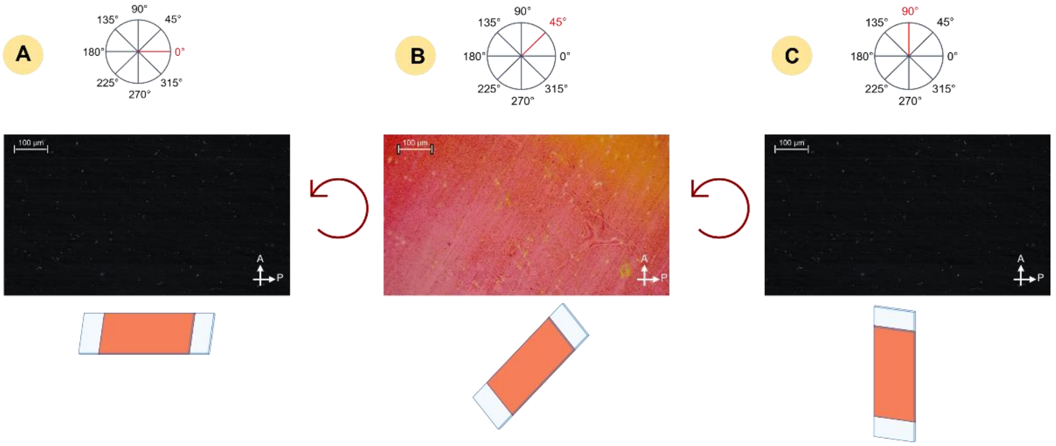

Figure 3.6: POM images of a LCN with homogenous planar alignment. A) image when the director is parallel to one polarizer showing light extinction; B) image when the director is at 45° angle with respect to one polarizer showing great enhancement of transmission; c) image when the director is perpendicular to one polarizer. Another time, light extinction was obtained.

The alignment degree of the materials was monitored by polarised absorption measurement to determine the order parameter (S) as reported in **Figure 3.7** and **Table 3.3**. Order parameter (S) was estimated by polarised absorption measurement on planar homogeneous films. Absorption spectra were recorded on a Varian Cary 400 instrument equipped with a linear polarizer and the dichroic ratio (R) was evaluated at the dye absorption maximum wavelength according to **Equation 3.2**:

Equation 3.2

$$R = \frac{A_{||}}{A_{\perp}}$$

where $A_{\parallel}$ and $A_{\perp}$ represent the parallel and perpendicular absorbance with respect to the director. **Figure 3.12** reported an example of polarised absorption spectra for a selected polymeric film (LCN6-tBu).

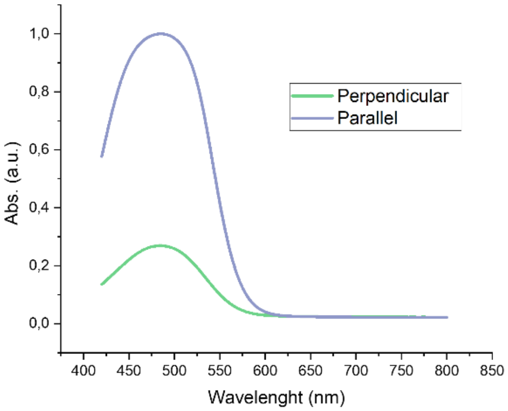

Figure 3.7: Example of polarised UV-vis absorption spectra for a LCN6-tBu film. The spectra are recorded respectively in parallel and perpendicular directions with respect to the nematic director.

The order parameter (S) was defined by **Equation 3.3**:

Equation 3.3

$$S = \frac{(R-1)}{(R+2)}$$

The values of S are reported in **Table 3.3** as a medium of 3 samples for each composition.

Table 3.3: Order parameter of different LCNs.

LCN	S
LCN3-Me$_{10}$	0.40 ± 0.04
LCN6-Me$_{10}$	0.49 ±0.08
LCN6-diMe$_{10}$	0.49± 0.02
LCN6-triMe$_{10}$	0.34 ± 0.05
LCN6-tBu$_{10}$	0.46 ± 0.02
LCN6-Ph$_{10}$	0.46 ± 0.01

In general, we observed similar good S values, with the exception for the material having trimethyl substitution that resulted in the less aligned of the series (S=0.34).

LCNs with the tert-butyl and the phenyl group in the crosslinker presented a slightly higher alignment degree (S=0.46) than the others. This was tested only for the mixture containing the lowest percentage of crosslinker. The order parameter generally is not affected by the increasing the content of one of the mesogenic reactives.

The glass transition temperatures (T$_g$) measured by DSC analysis for the different films were reported in **Figure 3.8**. Starting from our reference material, LCN3-Me (T$_g$ = 29 °C), the use of sterically hindered crosslinker led to a moderate decrease of T$_g$ up to 10 °C. Except for LCN3-Me, all the materials are in their rubbery state at room temperature while, as expected, no other peaks are present in the DSC traces. This observation is in agreement with the well-known behaviour of acrylate based LCNs, not presenting real nematic to isotropic transitions. Generally, a gradual decrease of order is obtained by heating up to generate a paranematic state, more disordered than the initial one but never completely isotropic.[124]

The increase of the flexible spacer length (from 3 to 6 -CH_2- groups) led to a moderate T_g decrease (from 29 to 20 °C), while no further changes were observed by introduction of an additional methyl group (also LCN6-diMe showed a T_g of 20 °C). Further increasing the steric hindrance on the central aromatic rings reduced the T_g with the lowest value observed in case of the phenyl group as the substituent (LCN6-Ph, T_g of 10 °C).

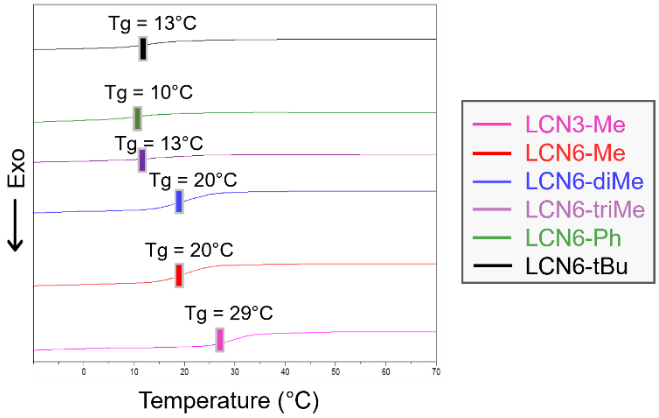

Figure 3.8: DSC traces of LCNs (10% of crosslinker). Heating cycle at 20 °C/min.

While increasing the content of the crosslinker in the mixture can lead us to obtain a partial increase in the glass transition temperature (Tg). LCN6-Me does not show a linear trend and the maximum difference of increase collected was 4°C. In the case of LCN6-Ph it is possible to obtain a difference of 9°C increasing the content of crosslinker by 10% to 30% as shown in **Figure 3.9.**

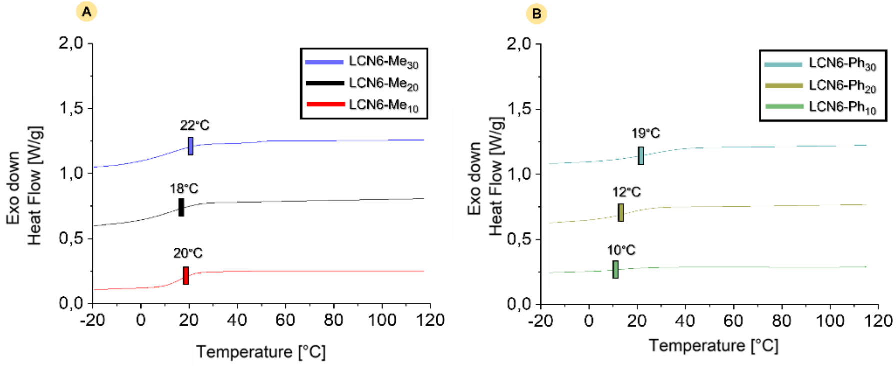

Figure 3.9: DSC traces of LCN6-Me and LCN6-Ph with different crosslinker %mol/mol. Heating cycle at 20 °C/min.

A more detailed mechanical characterization has been performed using a tensiometer for quasi static tensile measurements. For each composition, several tests (at least five replicates) have been performed on films having a thickness of 10 µm and a width and a length of about 7 and 15 mm, respectively. For each composition, the film was analysed in two directions, either parallel or perpendicular to the nematic director, as reported in **Figure 3.10A**.

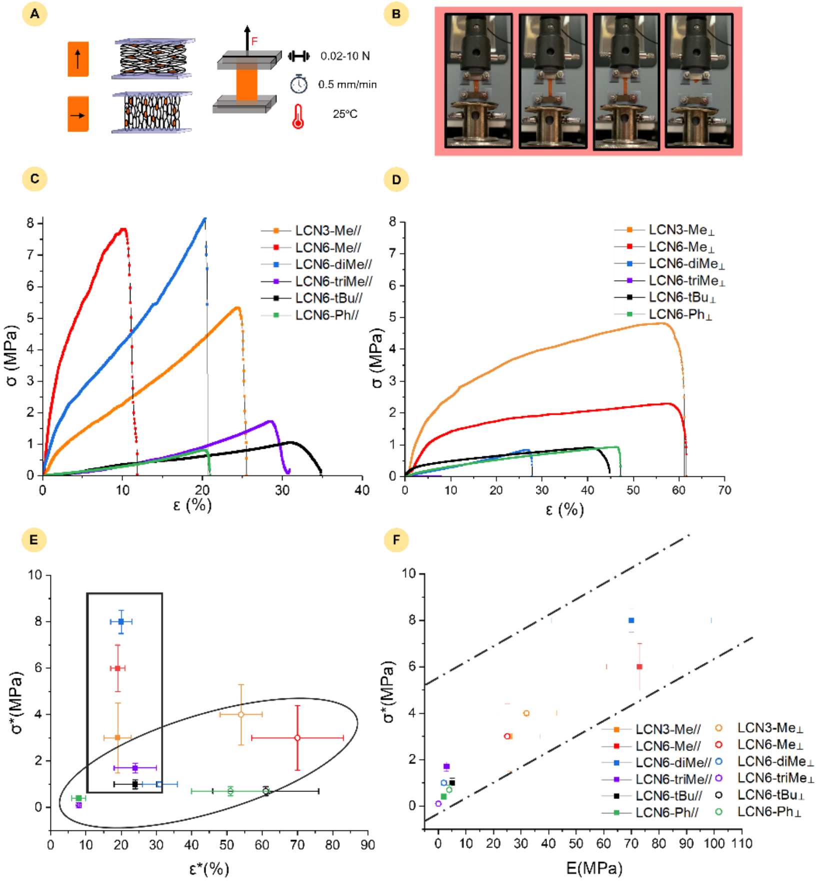

Figure 3.10: Tensile tests on LCNs (10% of crosslinker). A) Summary of the test conditions and B) pictures of a specimen during elongation; C) stress-strain graphs for LCNs analysed in the direction parallel to the director; D) stress-strain graphs for LCNs analysed in the direction perpendicular to the director; E) graph reporting the relationship between stress at break (σ*) against strain at break (ε*) for all samples; F) graph reporting the relationship between stress at break (σ*) and Young modulus (E) for all samples.

During the tensile test (**Figure 3.10B**) the material is stretched until breakage, which occurs by formation of a small crack, followed by its expansion until material failure. Representative engineering stress-strain curves are reported in **Figure 3.10C** and 3.**10D** for films analysed in the parallel and in the perpendicular direction, respectively. For the sake of clarity, a magnification of the stress-strain curve for LCN6-triMe tested in the perpendicular direction is reported in **Figure 3.11**.

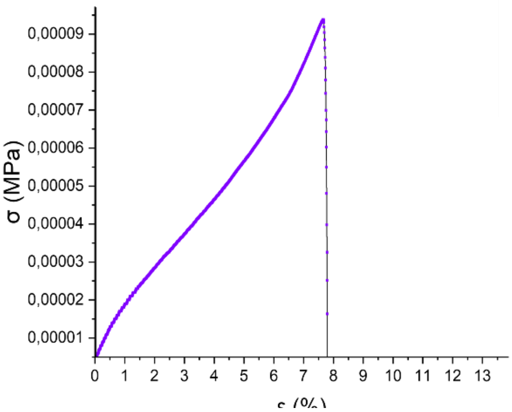

Figure 3.11: Stress-strain curve for LCN6-triMe analysed in the perpendicular direction with respect to the director.

From these analyses, different mechanical parameters were retrieved and compared. More specifically, **Figure 3.10E** shows the relationship between the stress at break (σ*) and the strain at break (ε*), while **Figure 3.10F** reports the correlation between stress at break and Young modulus (E). The value of all the mechanical parameters reported in the graphs are also listed in **Table 3.4**, together with the toughness (U) of the materials.

Table 3.4: Average of mechanical parameters extrapolated from three different stress-strain curves for the two different directions parallel and perpendicular to the director. Stress at break σ* (MPa), strain at break ε* (MPa), Young modulus E (MPa) and Toughness U (J/mm^3).

LCN//	$\overline{\sigma^*}$ [MPa]	$\overline{\varepsilon^*}$ [%]	E [MPa]	U [J/mm^3]	**LCN⊥**	$\overline{\sigma^*}$ [MPa]	$\overline{\varepsilon^*}$ [%]	E [Mpa]	U [J/mm^3]
LCN3-Me$_{10}$	3±1.5	19±3.8	26±7	3300± 100	LCN3-Me$_{10}$	4±1.3	54±6	32±11	18000 ± 7000
LCN6-Me$_{10}$	6±1	19±2	73±12	6600± 1000	LCN6-Me$_{10}$	3±1.4	70±13	25±21	16000 ± 7200
LCN6-diMe$_{10}$	8±0.5	20±3	70±29	8400 ± 920	LCN6-diMe$_{10}$	1±0.1	31±5	2±0.5	1100±7 7
LCN6-triMe$_{10}$	1.7±0.2	24±6	3±1	1400 ± 400	LCN6-triMe$_{10}$	3x10^{-3} ± 3x10^{-4}	8±0.2	0.03± 0.001	0.04 ± 0.006
LCN6-tBu$_{10}$	1±0.4	27±5	5±2	1300± 450	LCN6-tBu$_{10}$	0.7±0.2	61±15	4±3	2300± 540
LCN6-Ph$_{10}$	0.4±0.1	18±2	1±0.5	300± 185	LCN6-Ph$_{10}$	0.7±0.2	51±11	4±0.5	2300± 570

As expected for LC networks and elastomers, the materials present a strongly anisotropic mechanical behaviour. [125,126,127] When analysed in the parallel direction, the LCNs exhibit a higher stress at break but a lower strain at break with respect to the same formulation in the perpendicular direction (**Figure 3.10E**). Interestingly, the molecular structure of the crosslinker has a major effect on the stress at break of the resulting LCN film when tested in the parallel direction, while the elongation at break is essentially unaffected (reference to the guide for the eye in **Figure 3.10E**). With respect to the reference LCN film, indeed, a longer spacer in the crosslinker (LCN3-Me vs LCN6-Me) causes a twofold increase in the average value of σ*, which further increases up to about 8 MPa when using the crosslinker with two methyl in the rigid core (LCN6-diMe). On the other hand, a higher steric hindrance in the mesogenic core has a detrimental effect on the stiffness of the LCN films (LCN6-triMe, LCN6-tBu, and LCN6-Ph). When focusing on the mechanical properties in the perpendicular direction (reference to the guide for the eye in **Figure 3.10E**), instead, it clearly emerges that weaking the interactions among LC cores inside the material by introducing bulky substituents in the crosslinker determines a significant reduction in the film strength, and in some cases also a lowering of the elongation at break (LCN6-diMe and

LCN6-triMe). Regarding the Young modulus, a general trend can be observed for all the LCNs, for which high values of E are also accompanied by a high value of stress at break, as evidenced by the track highlighted in **Figure 3.10F**. Looking more in detail, as noticed also for the stress at the break, simply increasing the spacer length (LCN3-Me vs LCN6-Me) and slightly acting on the steric hindrance of the substituent (LCN3-Me vs LCN6-diMe) markedly improve the Young modulus in the parallel direction from about 25 MPa up to 70 MPa. However, while for the reference film the value of E is essentially the same in both directions, the LCN6-Me and LCN6-diMe are significantly less stiff when tested in the perpendicular one. Further increasing the bulkiness of the substituents dramatically softens the films, which exhibited a Young modulus well below 10 MPa irrespective of the testing condition. Overall, the data in **Figure 3.10E-F** indicate that acting on the molecular structure of the crosslinker is a powerful tool for tuning the mechanical response both in the parallel and in the perpendicular direction. The same analysis described in **Figure 3.12A-B** was made for LCNs with increased content of crosslinker. At least 5 tests have been performed on strips of the films having a thickness of 50 μm and a width and a length of about 7 and 15 mm, respectively. The comparison of the data with the previous analysis was possible due to the ratio between the force developed and the surface of the material considered. Each composition was measured in the two different directions with respect to the main director of the alignment (parallel and perpendicular) as shown in the stress-strain graphs reported in **Figure 3.12A-B** for the LCN6-Me$_Y$ and Figure 3.**12C-D** for the LCN6-Ph$_y$.

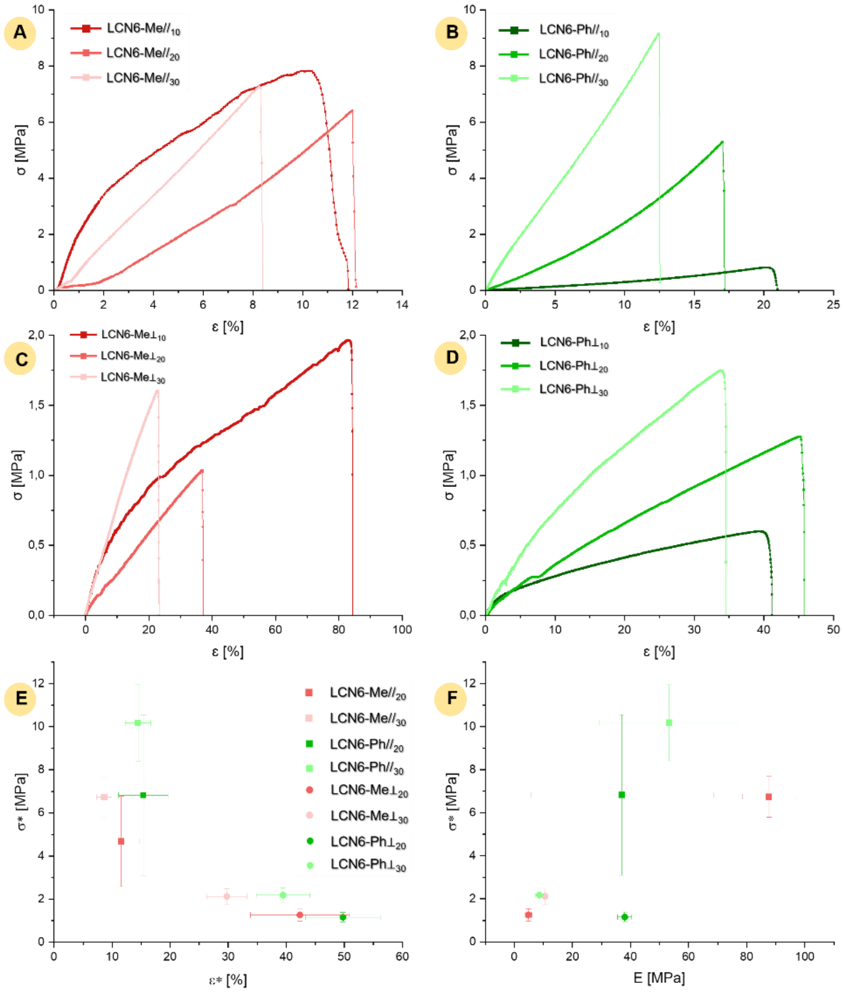

Figure 3.12: Tensile tests on LCN6-Me and LCN6-Ph for different content of crosslinker. A) stress-strain graphs for LCN6-Me analysed in the direction parallel to the director; B) stress-strain graphs for LCN6-Ph analysed in the direction parallel to the director; C) stress-strain graphs for LCN6-Me analysed in the direction perpendicular to the director; D) stress-strain graphs for LCN6-Ph analysed in the direction perpendicular to the director E) graph reporting the relationship between stress at break (σ*) against strain at break (ε*) for all samples; F) graph reporting the relationship between stress at break (σ*) and Young modulus (E) for all samples.

Where Y indicates the content of the crosslinker used to produce the LCN. LCN6-Me in both the direction of analysis have not showed a linear trend as the stress at break (σ*) did not increase under the increasing content of the crosslinker (6-8 MPa parallel direction). While the strain at break results decreased (from 12 to 8% parallel direction) in the case of LCN-Me$_{30}$. Otherwise LCN6-Ph$_{Y}$ showed a linear trend in both directions. **Figure 3.12B** collected the stress-strain curves of parallel direction analysis of the three materials showing how increasing the content of the crosslinker percentage in the mixture provide an increase in the stress at break and a consequent decrease in the strain at break (ε*) (from 20% to 12%). This same trend was observed in **Figure 3.12D** regarding the analysis of the strips in the perpendicular direction with respect to the main director. The anisotropy was once again evident from the stress-strain graphs reported as already demonstrated for those kinds of elastomeric polymers. Regarding the Young modulus and the toughness of the materials, extrapolated from the stress-strain graphs, all the data collected are reported in **Table 3.5.**

Table 3.5: Average of mechanical parameters extrapolated from three different stress-strain curves for the two different directions parallel and perpendicular for different percentages of CL6-Me and CL6-Ph. Stress at break σ* (MPa), strain at break ε* (MPa), Young modulus E (MPa) and Toughness U (J/mm^3).

LCN//	$\overline{\sigma^*}$ [MPa]	$\overline{\varepsilon^*}$ [%]	E [MPa]	U [J/mm^3]	**LCN⊥**	$\overline{\sigma^*}$ [MPa]	$\overline{\varepsilon^*}$ [%]	E [MPa]	U [J/mm^3]
LCN6-Me$_{10}$	6±1	19±2	73±12	6600±1000	LCN6-Me$_{10}$	3±1.4	70±13	25±21	16000±7200
LCN6-Me$_{20}$	5±2	12±3	22±9	1927±1170	LCN6-Me$_{20}$	1.3±0.3	42±9	5±1.1	2945±1189
LCN6-Me$_{30}$	7±0.9	9±1.3	88±9	2599±726	LCN6-Me$_{30}$	2±0.4	30±4	11±1	3465±1008
LCN6-Ph$_{10}$	0.4±0.1	18±2	1±0.5	300±185	LCN6-Ph$_{10}$	0.7±0.2	51±11	4±0.5	2300±570
LCN6-Ph$_{20}$	7±4	15±4	37±31	4558±2502	LCN6-Ph$_{20}$	1.2±0.2	50±6	38±2	3167±946
LCN6-Ph$_{30}$	7±0.9	9±1.3	88±9	2599±762	LCN6-Ph$_{30}$	7±0.9	9±1.3	88±9	2599±762

Comparing the results obtained in the previous analysis the same no-linear trend for LCN6-Me was observed obtaining an increase of the Young modulus of the material (E) while the LCN6-Ph shows a linear increase of the E due to the increase of crosslinker in the mixture. Interesting to note that at the same content of crosslinker percentage (30%) in the mixture the two materials showed the same Young modulus of 88 MPa as average value. This means that even using a substituent with a higher steric hindrance it is possible to replicate the same mechanical features of ones possessing a lower steric hindered substituent. Also, in the case of LCN6-Ph$_Y$ it was possible to tune the stiffness properties of the material only increasing the crosslinker percentage from **4 MPa** to **88 MPa** changing completely the behaviour and the applicability of the material. Even more, it is possible to observe that in terms of stiffness the different directions in which the material was analysed haven't affected the results.

Figure 3.12E-F reported also the behaviour of the materials of the stress at break (σ*) with respect to the elongation at break (ε*) and the Young modulus (E). It was evident from **Figure 3.12E** how the two classes of materials, due to the anisotropic behaviour of the LCNs, are completely separated in two regions of the graphs. The strip which had a parallel orientation with respect to the alignment director showed high stress at break (σ*) and lower elongation at break (ε*). Nevertheless, the materials analysed in the perpendicular direction with respect to the main director of the network depicted lower stress at break (σ*) and higher elongation at break (ε*) . This is another demonstration of how the substituent of the crosslinker molecular structure can be a tool to deeply modulate the mechanical behaviour of the final LCN.

Figure 3.12F depicted the behaviour of the stress at break of the materials related to the stiffness measured through the Young modulus. The first information is that the LCN6-Me$_{30}$// and LCN6-Me$_{20}\perp$ had the same behaviour and in **Figure 3.13** has been depicted a zoom of the region of interest.

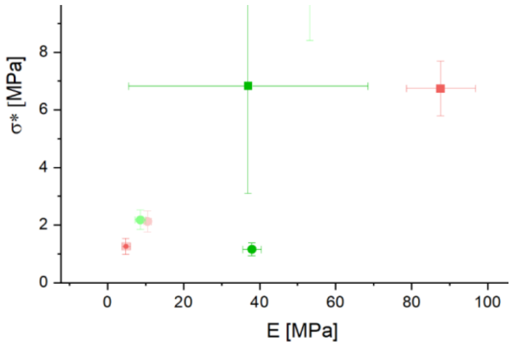

Figure 3.13: Zoom of the region for stress at break (σ*) and Young modulus (E).

LCN6-Ph$_Y$ in both of the directions of the analysis showed the best compromise in terms of stress at break and elasticity of the network. The weaker strength of the materials with bulky substituent in the core of the crosslinker can be modulated by the increasing of the percentage of the crosslinker in the formulation to produce the final LCN and lead to the application of those materials in the field of cardiac tissue engineering due to the mechanical parameters deeply analysed.

3.2.2 Light actuation properties of different acrylate based LCNs

The photomechanical properties of the LCNs were characterised, as previously described, by using a customised set-up to measure the material force production and the corresponding kinetics of force development and relaxation. [121,123] In brief, the LCNs strips were vertically mounted between a force transducer on top and a fixed end on the bottom (**Figure 3.14A**) to measure the force under isometric conditions. The LCN strip was located between two arrays of mini-LEDs (mLEDs). Each array was made by eight independent mLED units emitting at λ= 470 nm with a pixel pitch of 0.75.[121] The LCN films were cut into strips with longer dimensions along the nematic director, i.e., 8 mm in length x 1.6 mm in width x 0.01 mm in thickness. The mLED wavelength was chosen to overlap the maximum absorption region of the dye (**Figure 3.14B**).

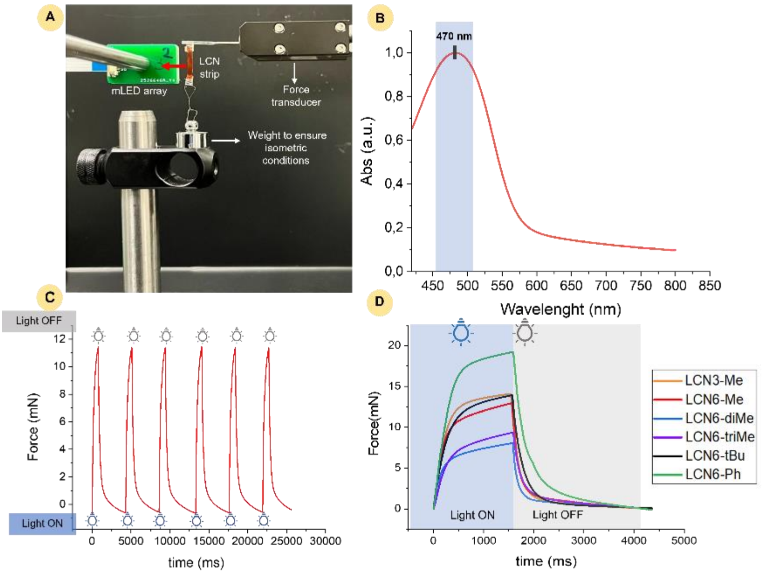

Figure 3.14: Examples of force development under irradiation. A) Images of the setup for force measurement. During the actuation, the sample was positioned in between the two mLED arrays (following the red arrow); B) UV-Vis spectra of a LCN6-Ph film; C) Trace of multiple activation and relaxation cycles of LCN6-Me under pulsed irradiation by the mLED (14.2 mW/mm^2); D) Force/time graph for the determination of the force developed by the materials under blue light. Data reported are referred to representative traces obtained by irradiation of the material with 14.2 mW/mm^2 power and pulsed t_{ON}= 1500 ms and t_{OFF}= 3000 ms.

As already described,[119] the force production greatly depends both on the material composition and on the illumination conditions, influencing in a not obvious way both, the maximum tensions reached and the kinetics of force development. For this reason, light activation has been tested in different illumination conditions. First, the mechanical performances of the LCNs strips were characterised during long-lasting light pulses (that allow the material to reach a nearly-plateau level of force production) under a light power of 14.2 mW/mm^2. This activation and relaxation pulse of the materials is cyclable and will continue over time without resulting in changes to the force trace obtained. This is evidence of the dye resistance to photobleaching, and of its stability as shown in **Figure 3.14C.** LCN6 materials were compared to the reference one (LCN3-Me). For each material, a representative trace is reported in **Figure 3.14D** while the medium values of maximum force

(F) and tension (T) (expressed as the ratio of maximum force developed per area of illumination), are provided in **Table 3.6**.

Table 3.6: Force production under light- irradiation. F: Maximum force developed under the light irradiation (14.2 mW/mm^2) on the plateaux of the trace; T: tension development determined dividing the force by the illumination cross-section (0.01 mm thickness x 1.6 mm width) of the material; Values are medium of 3 samples.

LCN	F [mN]	T [KPa]
LCN3-Me$_{10}$	14 ± 1	896 ± 68
LCN6-Me$_{10}$	14 ± 3	870± 192
LCN6-diMe$_{10}$	9 ± 1	559 ± 67
LCN6-triMe$_{10}$	10 ± 2	643 ± 150
LCN6-tBu$_{10}$	16 ± 1	951 ± 120
LCN6-Ph$_{10}$	24 ± 3	1480 ± 220

Upon light illumination, tension initially rises in a nearly linear way, as demonstrated by the analysis of the linear fitting of the curves between 0-100 and 0-200 ms (reported in **Figure 3.15**).

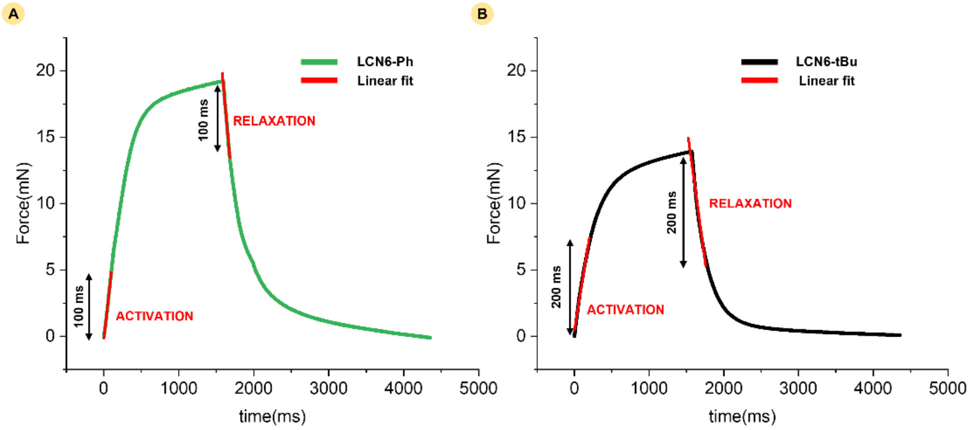

Figure 3.15: Activation and relaxation linear fit for 100 ms and 200 ms. A) Example of the linear fit used on LCN6-Ph on activation and relaxation for 100 ms. B) Example of the linear fit used on LCN6-tBu on activation and relaxation for 200 ms.

In **Table 3.7** a comparison of the kinetic actuation parameters in these ranges is also shown.

Table 3.7: Kinetic actuation parameter under light- irradiation in the "linear" range. Va 100: Rate of activation of the material determined with a linear fit on the first 100 ms; Va 200: Rate of activation of the material determined with a linear fit on the first 200 ms; Vr 100: Rate of relaxation of the material determined with a linear fit on the first 100 ms; Vr 200: Rate of relaxation of the material determined with a linear fit on the first 200 ms.

	Rate [KPa/ms]			
LCN	Va$_{100}$	Va$_{200}$	Vr$_{100}$	Vr$_{200}$
LCN3-Me$_{10}$	2 ± 0.6	2± 0.2	4 ± 0.3	1 ± 0.2
LCN6-Me$_{10}$	4± 1	3± 0.7	5± 0.6	3± 0.5
LCN6-diMe$_{10}$	2 ± 0.5	2 ± 0.3	3 ± 0.7	2 ± 0.3
LCN6-triMe$_{10}$	1 ± 0.1	1 ± 0.1	2 ± 0.2	2 ± 0.6
LCN6-tBu$_{10}$	4± 0.6	3 ± 0.4	4 ± 1	4 ± 0.7
LCN6-Ph$_{10}$	3± 0.6	2 ± 0.2	4 ± 0.2	3 ± 0.4

First, we observed that maximal tension is reduced in LCN6-diMe and LCN6-triMe strips if compared to the other materials. Furthermore, the rate of activation and relaxation decreases from LCN3-diMe to LCN6-triMe, demonstrating that as the number of methyl grows, the tension buildup and the response to activation worsens.

On the other hand, LCN6-Ph and LCN6-tBu showed maximal tension levels that were similar or even higher than the reference one (LCN3-Me), while LCN6-Me demonstrated high features for the activation time, and they were chosen for further mechanical characterizations. In this case, the recordings were performed at a much lower light intensity (3.5 mW/mm^2), mowing toward the threshold level for the material activation. This choice was driven by the need to approach intensity levels more suitable for biological applications towards the application of such materials to develop artificial muscles. In this condition, the 3 materials analysed showed all similar tension levels after 2 second illumination, but the slope of the force trace (measured during the first 200 ms of activation that presents a nearly linear phase) was significantly higher in LCN6-Ph and LCN6-tBu, underling a faster kinetics. (**Figure 3.16**). Therefore, the LCN6-Ph and the LCN6-tBu, results as the more suitable, among the investigated materials, to be applied in the cardiac tissue engineering field as active contractile layers. The reported light actuation tests are made in collaboration with the Department of Experimental and Clinical Medicine of the University of Florence.

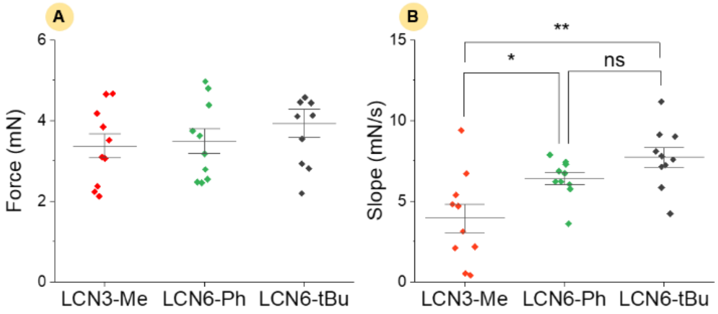

Figure 3.16: Force development at low intensity irradiation. Maximum force developed at the plateau (a) and slope of the force trace in the first 200 ms of activation for different materials under irradiation at 3.5 mW/mm^2. Statics analysis: one-way analysis of variance (ANOVA) test was used to compare features between the three materials (N = 10). For the comparison of means between each material the Tukey's post hoc analysis was used. A p value of < 0.05 was considered as indicative of a statistically significant difference between means (NS: $p > 0.05$; *$p < 0.05$; **$p < 0.01$). Statistical analysis was performed using GraphPad Prism, version 8.4.3.

3.2.3 Light actuation properties of materials containing different percentage of CL6-Me and CL6-Ph

Considering the behaviour of different materials during the activation phase, at the moment when the light stimulus is switched on, it appears that the material containing CL6-Me has the highest activation rate (on the millisecond scale), followed immediately by the material with CL6-Ph, which is also able to provide higher tension at longer activation times (2 seconds of irradiation). Both materials were studied with only 10% mol/mol crosslinker, and modulation of this parameter could be exploited to also improve passive mechanical strength properties in addition to influencing tension development. In this paragraph we focused on the optimization of mixtures containing CL6-Me and CL6-Ph at different crosslinker contents in order to optimise their properties and develop photo-responsive artificial muscles. The LED illumination in this case was kept at low power (2.4 mW/mm^2) compared to previous studies to facilitate their use in *in vivo* biological applications. This preliminary characterization will be completed in further developments screening the tension, developed by the materials, with different (increasing) power lights. For each test, at least 3 strips were cut from 3 different LCNs with dimensions of 8 mm length (along the nematic director) x

1.5 mm width x 0.02 mm thickness. The measurement is based on the application of a pulsed light for a certain period of time (t_{ON}), which can be changed like in the previous case. In the present case, t_{ON} was varied from 250 to 5000 ms in order to evaluate in the first case, a cardiac activation up to the last case in which the durability of the material over long activation times was analysed. An example of the different force development trace during 250 ms of activation times is shown in **Figure 3.17**, in which the LCN6-Ph_{10} strip was activated several times over time.

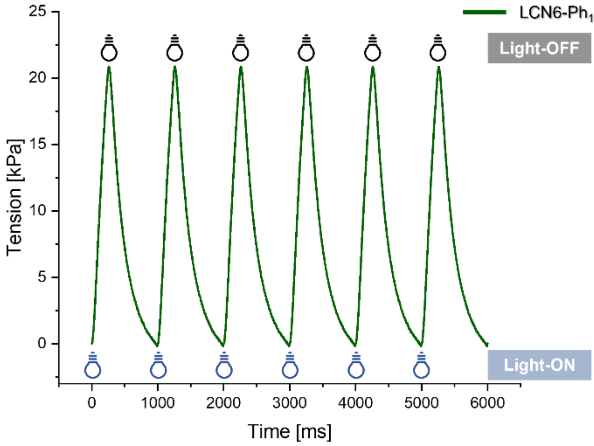

Figure 3.17: Tension trace under light-irradiation for LCN6-Ph_{10}.

The force traces indicate how the force development remains constant over time and the good reproducibility of the mechanical work during different activation cycles. This demonstrates the reversibility of the process and durability properties over time.

The highest tension has been depicted for LCN6-Ph_{20} (around **38 kPa)**, while for short activation times the trend is completely reversed. As can be seen in **Figure 3.18A**, for mixtures containing LCN6-Me, the maximum tension produced falls from 30 kPa to 8 kPa by increasing cross-linking from 10% to 20%, while it increases slightly (12 kPa) for LCN6-Me_{30}. For the mixtures containing LCN6-Ph (**Figure 3.18B**), the maximum tension values remain almost comparable: for LCN6-Ph_{10} and LCN6-Ph_{20}, the tension increases to values of 31 kPa and 40 kPa respectively. For the 30% crosslinker mixture, it decreases to 27 kPa. For mixtures containing the phenyl group, we can see a greater difference between the tension values produced when going down to t_{ON} values of 250 ms. In this case, as we move from the lowest to the highest crosslinker concentration, the maximum tension value produced decreases to the respective values: **18** kPa, **14** kPa and **5** kPa.

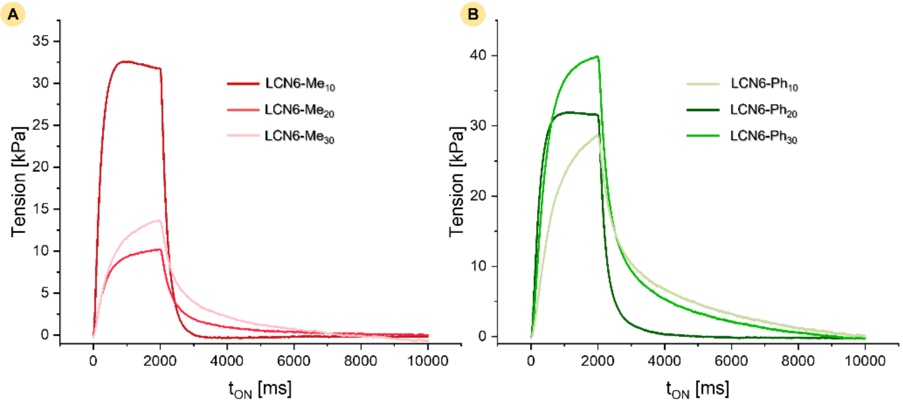

Figure 3.18: Tension development under light- for different percentage of CL6-Me and CL6-Ph. A) Tension/time graph for the determination of the force developed by the LCN6-Me$_Y$ under blue light. Data reported are referred to representative traces obtained by irradiation of the material with 2.4 mW/mm^2 power and pulsed t$_{ON}$= 0 ms and t$_{OFF}$=2000 ms. B) Tension/time graph for the determination of the force developed by the LCN6-Ph$_Y$ under blue light. Data reported are referred to representative traces obtained by irradiation of the material with 2.4 mW/mm^2 power and pulsed t$_{ON}$= 0 ms and t$_{OFF}$= 2000 ms.

Furthermore, as shown in **Figure 3.19**, the behaviour under light activation of the two material families considered (LCN6-Me and LCN6-Ph) was compared. By comparing only the central substituent of the crosslinker, it can be seen that at long activation times, phenyl produces a higher tension than methyl, whereas for short activation times (250 ms), the difference in values tends to narrow (**Figure 3.19**). If we also consider the percentage of crosslinker present in the material, on the other hand, it is interesting to observe that for long activation times, LCN6-Ph$_{20}$ is the best material in terms of tension developed. On the other hand, considering all the times of activation tested for the series of methyl substituent, LCN6-Me$_{10}$ shows the best tension development.

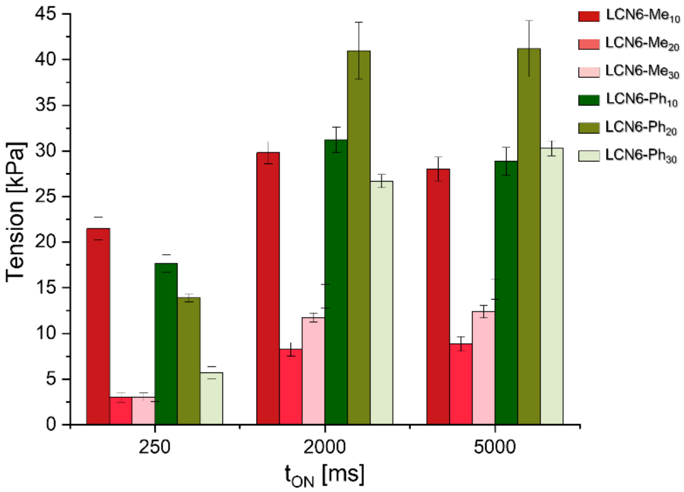

Figure 3.19: Tension/time bar graph for the comparison of LCNs with different percentages of CL6-Me and CL6-Ph analysed.

In order to be usable, the LCN must possess a certain tension value over a certain time range. For this purpose, average activation and relaxation kinetics data were extrapolated from four tension curves obtained for each material. The standard deviation (σ) of each value was then calculated using the following equation:

Equation 3.4

$$\sigma = \sqrt{\frac{\Sigma(x-\underline{x})^2}{2(n-1)}}$$

where x is the observable to be analysed, $\bar{x}$ is its mean value and n is the numerosity of the observable.

The half-activation time (time required to achieve the development of 50% of the maximum activation) was considered as an indicator of the activation rate of the material. As shown in **Table 3.8**, it can be seen that as the percentage of the crosslinker increases, regardless of the crosslinker considered, the activation time increases for both materials. Increasing the content of the crosslinker should reduce the rate of activation and relaxation of the materials.

Table 3.8: Tension and kinetic parameters under light- irradiation. F: Maximum force developed under the light irradiation on the plateaux of the trace; T: tension development determined dividing

the force by the illumination cross-section (0.01 mm thickness x 1.6 mm width) of the material; $t_{1/2}$act: semi-activation time; $t_{1/2}$rel: semi-relaxation time. Values are mediums of at least 3 strips of 3 samples.

LCN	F [mN]	T [kPa]	$t_{1/2}$ act [ms]	$t_{1/2}$rel [ms]
LCN6-Me$_{10}$	1 ± 0.2	30 ± 1	189±13	126±21
LCN6-Me$_{20}$	0.3± 0.05	8± 1	323±35	331±7
LCN6-Me$_{30}$	0.4 ± 0.02	12 ± 1	353±16	394±16
LCN6-Ph$_{10}$	1 ± 0.2	31 ± 1	238±14	214±14
LCN6-Ph$_{20}$	1.3 ± 0	40 ± 2	333±1	333±1
LCN6-Ph$_{30}$	1 ± 0.1	27 ± 1	463±23	511±34

If, on the other hand, LCN6-Me and LCN6-Ph are to be compared, although the latter produces a higher tension, it is kinetically slower. On the other hand, when considering relaxation, the same behaviour is observed, making LCN6-Ph the material to be used for tension generation on the one hand. Methyl (only in the case of LCN6-Me$_{30}$) is kinetically favoured on the other. In conclusion, LCN-Ph$_{20}$ represents the best compromise between tension generation and kinetic performances. Furthermore, a second kinetic evaluation was made in the linear region of the tension development on time (first 100-200 ms) and the complete table of parameters is reported in **Table 3. 9**.

Table 3.9: Kinetic actuation parameter under light- irradiation in the "linear" range for different percentage of CL6-Me and CL6-Ph. Va 100: Rate of activation of the material determined with a linear fit on the first 100 ms; Va 200: Rate of activation of the material determined with a linear fit on the first 200 ms; Vr 100: Rate of relaxation of the material determined with a linear fit on the first 100 ms; Vr 200: Rate of relaxation of the material determined with a linear fit on the first 200 ms.

	Rate [KPa/ms]			
LCN	Va$_{100}$	Va$_{200}$	Vr$_{100}$	Vr$_{200}$
LCN6-Me$_{10}$	2 ± 0.1	2 ± 0.1	2 ± 0.1	2 ± 0.1
LCN6-Me$_{20}$	6 ± 0.9	5± 2	5 ± 2	4 ± 2
LCN6-Me$_{30}$	7± 0.5	9± 0.6	10± 0.1	9± 0.2
LCN6-Ph$_{10}$	6± 1	7± 1	8± 1	8± 1
LCN6-Ph$_{20}$	3 ± 1	4 ± 1.7	6 ± 1	6 ± 1.6
LCN6-Ph$_{30}$	2 ± 0.8	4 ± 0.4	8 ± 0.4	6 ± 0.6

It shows that for both series increasing the content of the crosslinker in the molecular structure of the LCN should reduce the rate of activation of the materials. In the case of LCN6-Ph this behaviour is even less marked, for the relaxation kinetics, than the LCN6-Me.

3.3 Conclusions

In this chapter, we approached the implementation of liquid crystal based light responsive smart materials by the modification of the crosslinker chemical structure towards LCNs able to mimic the mechanical cardiac function. A palette of liquid crystalline crosslinkers, bearing different hindered substituents and an acrylate containing benzoic acid was prepared, and used to prepare new LCNs by photopolymerization. About the mechanical properties, the introduction of bulky substituents in the crosslinker core led to an increased elasticity, with Young modulus lower than 4 MPa but with a consequent break at stresses below 2 MPa. The addition of methyl groups (from 1 to 3) in the crosslinker core, not only lead to a very low stress at break but also to lower force production during illumination, demonstrating as this modification leads to a general worsening of the mechanical ad actuation properties. LCN6-

Ph, LCN6-tBu and LCN6-Me demonstrated the best photo-actuation capabilities in terms of tension development and rate of activation. These materials still demonstrated a Young's modulus of approximately 1 MPa, significantly higher if compared to cardiac muscles (5-20 kPa) but lower if compared to LCN3-Me, and faster kinetics with respect to the other materials. This would provide an advantage for applications that require a fast contraction relaxation cycle, like those regarding the mechanical assistance of the cardiac muscle. In fact, for instance, if the contraction time course is in the order of 200-400 ms (as in the case of human myocardium), given the slopes that we measured for LCN6-Ph and LCN6-tBu, we expect that both materials would produce 30-40% tension more than the reference LCN3-Me. Changing the crosslinker molecular structure, even on confined parts of the molecule, demonstrates to be a powerful tool to modulate the materials mechanical and photoactivation properties, with a defined trend highlighted for the increased number of methyl groups (decreased force production, increased rigidity and slower kinetics) and an interesting increased contraction kinetics for LCN6-Ph and LCN6-tBu. The two series also behave differently about tension development under irradiation when a change in the content of the crosslinker was done. In the case of the crosslinker CL6-Ph, irradiated with a 2.4 mW/mm^2 light source, tension values ranging from **30** to **40** kPa are recorded for long activation times (2000 ms), with semi-activation times decreasing with the percentage of crosslinker (from 236 ms to 463 ms). In this case, tension development was significantly decreased by the increase of the content of crosslinker. In the case of the CL6-Me crosslinker, on the other hand, there is both a strong decrease in tension and a considerable increase in activation time. Under this test condition, the materials with CL6-Ph result in the highest force. For short activation times (250 ms), LCN6-Me$_{10}$ undoubtedly represents the best compromise between tension development and kinetic timing, demonstrating the best force development rate of the series analysed. In general, LCN-Ph$_{20}$ represents the best compromise between tension generation and kinetic performances. This study enables the identification of these last crosslinkers for the further development of photo-responsive films with applications in cardiac tissue engineering. Further studies will be concentrated on the modification of the formulation composition to obtain material with higher resistance to mechanical load and more efficient force development under light irradiation. Moreover, a careful evaluation of the tension developed under different light powers will be done. Overall, the results of this research show that LCNs may be suitable for assisting cardiac contraction as they exhibit fast activation/inactivation kinetics and adjustable tension capable of mimicking muscle function.

3.4 Experimental section

Materials: liquid crystalline components C6BP (4-Methoxybenzoic acid 4-(6-acryloyloxyhexyloxy) phenyl ester), CL3-Me (1,4-Bis-[4-(3-acryloyloxypropyloxy)benzoyloxy]-2-methylbenzene, also known as RM257) , CL6-Me 1,4-Bis-[4-(6-acryloyloxyhexyloxy)benzoyloxy]-2-methylbenzene also known as RM82) and Irgacure 369 were purchased from Sigma-Aldrich as received and listed in **Table 3.10**. Crosslinkers were synthesised as described in **Chapter 2**.

Table 3.10: Data information for the reagents used for the synthesis of diacrylate substituted crosslinkers.

Product	**Cas number**	**Supplier**
Polyvinylalcohol (PVA)	9002-89-5	Sigma-Aldrich
Dispersed red 1-Acrylate (DR1-A)	13695-46-0	Sigma-Aldrich
C6BP	130953-14-9	Sigma-Aldrich
Irgacure 369	119313-12-1	Sigma-Aldrich

LCN preparations: all monomer mixtures contain the mesogen C6BP (88% mol/mol), one of the crosslinker CLX-Y (10% mol/mol), Irgacure 369 (1% mol/mol) and the acrylate dye DR1 (1% mol/mol). To prepare the LC cells, microscope cover slides were coated with an aqueous solution of polyvinyl alcohol (5% wt) and rubbed unidirectionally with a velvet cloth. The cell was assembled by two cover slides separated by 10 µm microspheres as spacers.

To prepare the LCN film, the mixture was melted in the isotropic phase and infiltrated by capillary in a LC cell treated to obtain a homogeneous planar alignment. The material was cooled to room temperature to reach a monodomain nematic texture and photopolymerized at 25 °C for 10 minutes under UV-light (385 nm, M385LP1-C4 lamp Thorlabs, 1.2 mW/cm^2). A post-curing step was applied by UV irradiation for further 10 minutes at 45 °C.

Mesomorphic properties characterization: phase transition temperature of monomers and LCNs were measured using a DSC TA Instruments Calorimeter Q-2000 (TA Instruments, Milan, Italy) in a nitrogen atmosphere (heating and cooling rate: 20 °C/min). Polarised Optical microscopy was performed with an inverted microscope (Zeiss Axio Observer A1) in cross-polarized mode equipped with a Linkam PE120 hot stage and an Axio camera to obtain pictures of the LC textures.

Mechanical tensile test: a Tensometer 2020 (Alpha Technologies) was used to examine the mechanical behaviour of the films during a quasi-static tensile test. The specimen was secured in between two custom-made clamps (**Figure 3.10A-B**), and then the mobile upper crosshead started to move at a constant speed of 0.5 mm/min, stretching the film until breakage. The force was monitored throughout the test by a load cell (max force 10 N, 0.02 N accuracy). The engineering stress (σ=force/initial specimen section) and strain (ε=displacement/initial film length) were calculated from the measured force and displacement data. From the stress-strain data shown in Figure 20 C-D, it was possible to determine the stress at break (σ*), strain at break (ε*), Young's modulus (E), and toughness (U) of the various materials. Young's modulus (E) was calculated from the stress-strain curves in the initial region where the material demonstrated an analytically linear mechanical response. The modulus was extrapolated using **Equation 3.5**, which describes the elastic characteristics of the various LCNs, by using a linear fit of the curve.

Equation 3.5

$$E = \frac{d\sigma}{d\varepsilon}\Big|_{\varepsilon=\varepsilon_l}$$

In addition, the energy required to fracture the material per unit volume, defined as Toughness (U) was determined by the area under the stress-strain curve using **Equation 3.6**:

Equation 3.6

$$U = \int_{\varepsilon_0}^{\varepsilon^*} \sigma \, d\varepsilon$$

Active tension characterization: The force developed under irradiation by the LCNs were recorded in a custom-made setup previously described.[119,121] Briefly, the apparatus consists of a force transducer (WPI KG4, 0-50 mN scale) to which a LCN strip was attached (and held in isometric condition by a weight of approximately 5g). Two micro-LED arrays, each composed of eight micro-LEDs emitting blue light (470 nm), were used to irradiate the materials simultaneously on both sides. The activation was controlled by a LabVIEW program with a multichannel driver. Data reported are obtained by irradiation of the material with pulsed light at 14.2 mW/mm^2 (**Figure 3.14**) or 3.5 mW/mm^2 (**Figure 3.18**).

Chapter 4

Liquid Crystalline Network microstructures for stimuli responsive labels with multi-level encryption

4.1 Introduction

During the last century, various technological processes for three-dimensional printing have been brought to light due to the great commercial demand and the impact of possible real-world applications. Common 3D printing technologies (such as stereolithography) offer a resolution in the hundred micrometre range, whereas Direct Laser Writing (DLW) offers the possibility, among other lithographic techniques, to produce 3D structures with typical 100-150 nm resolution. Besides the extraordinary resolution, the size of the printed objects can be millimetres in all three dimensions. The difference is in the process of producing the desired 3D structure. In the field of 2D printing, the term 'pixel' refers to a two-dimensional element, while the term 'voxel', introduced for TP-DLW, denotes the smallest printed volume of the 3D object. The first demonstration of TP-DLW dates to 1997[128] and has subsequently been used for the realisation of objects with different fields of application. The application areas include Micro-optics, micro-fluidics, photonics, biomedical applications, micro-mechanical systems (MEMS), 3D scaffold for cell cultures, micro-robotics and micro-actuators. [129,130] In addition, commercially available DLW printing systems have been available since 2007 and this has led to an intensification of academic as well as commercial use. One of the most important changes made after 2014 was the increase in system speed in the printing parameters with the advent of a mirrored galvanometric scanning system. The technical details of the tool and the fabrication of 3D structures will be provided in the following sections of this Introduction. Despite all the innovations and improvements to the printing system and resolution, limitations related to the photo-printed materials, which are referred to as photo-chemical resolution limitations, are still present and yet unclear. [131] The different chemical and physical mechanisms that determine the printing process makes the system increasingly complex and difficult to interpret. Among the different printing technologies (e.g., stereolithography, digital light processing, continuous liquid interface production etc), this technique remains one of the best and unique choices in the fabrication of 3D and 4D micrometric structures.

4.1.1 Direct Laser Writing instrument

A common schematic for the DLW system, referring to the Nanoscribe system (Nanoscribe Photonics Professional), is shown in **Figure 4.1**.

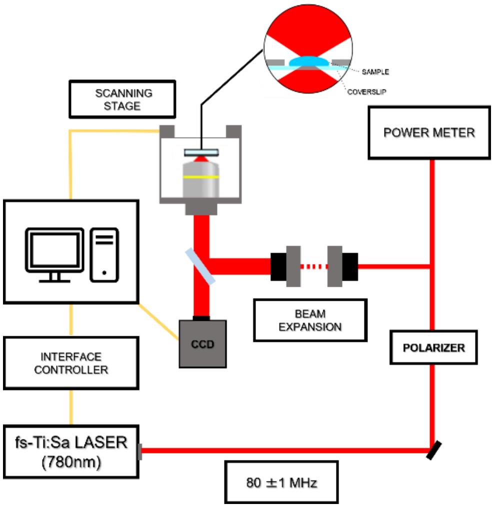

Figure 4.1: General scheme of a Direct laser writing (Nanoscribe (GmbH)) set up.

It is equipped with a fibre laser (Erbium doped fibre) at a wavelength of 780 nm and a pulse duration of less than 120 fs at a repetition rate of 80 MHz. In addition, the usability is increased by some additional elements such as the camera, which allows the reaction process to be followed in real-time. An automatic 'interface finder', a piezo-electric motorised stage for automated displacement of the sample. The entire set-up is automated to allow maximum reproducibility and resolution of the printed objects.

As far as focusing conditions are concerned, high resolution is achieved by using objectives with high numerical aperture (NA= nsinα), with n the refractive index of the photoresist and α the aperture angle). A common objective used for production is the 100x which has a numerical aperture of 1.4 and an aperture angle of 70°. This has a focus with a lateral dimension of 330 nm (full width at half maximum, FWHM) and an axial dimension of 800 nm (FWHM).

4.1.2 Multi-photon absorption and two-photon polymerisation (TPP)

For the realisation of 3D micrometric structures, direct laser writing involves a multi-photon absorption process. Therefore, the choice of resist must meet ultralow single-photon absorption and make the multiphoton absorption process dominant. In general, resist polymerisation is a free radical polymerisation involving the breaking of chemical bonds and the formation of radicals by means of three steps, which are discussed in detail in the Introduction. A typical value of the dissociation energy is in the order of 3 eV. To reach this value, an absorption of at least two photons in the near IR range is necessary. In fact, the process demonstrated as predominant during direct laser writing is a two-photon absorption (2PA).[128] This was first introduced in 1931[132] and is based on the simultaneous absorption of two photons, given by the excitation of the molecule in contact with electromagnetic radiation, without the presence of due intermediate states. The difference between the two absorption processes, one-photon and two-photon absorption, is shown in **Figure 4.2** and analysed in detail later.

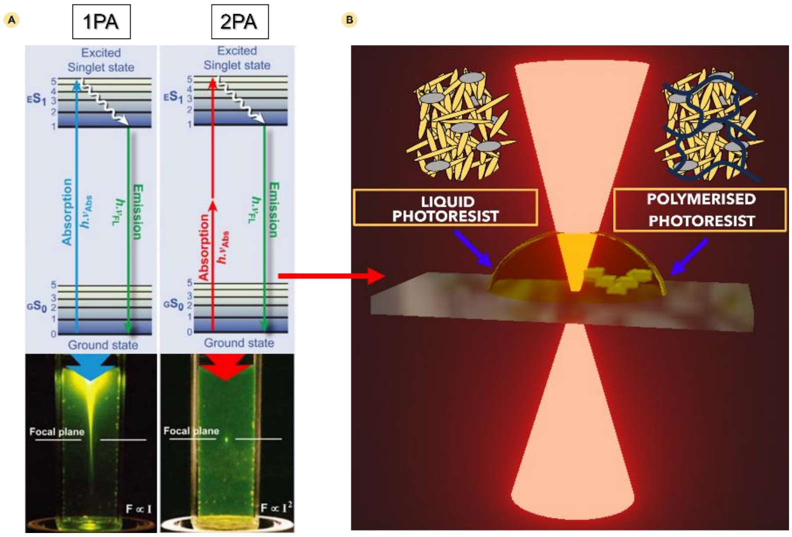

Figure 4.2: Difference between one photon absorption and two photon absorption. A) Absorption pathway for the two different processes.[133] B) Two-photon polymerization process with liquid photoresist.

In one-photon absorption (OPA), the single photon passes from the ground to the excited state and the corresponding polymerisation involves the entire illuminated volume of material. In the case of two-photon absorption, two photons involved in the process are brought into the excited state up to a so-called 'virtual' state in which their lifetime is of the order of femtoseconds. If during this time the energy transferred to the system exceeds the polymerisation threshold, the polymerisation of the voxel (which is the polymer volume involved in the process) and the formation of a rigid material is obtained. This happens only in the focal spot of a focused high-power laser where the light intensity is high enough to compensate for the small two photon cross section. This process can be repeated point by point until the desired 3D micrometric structure is completely defined.

4.1.3 Photo-initiator and Photo-resist

In general, a material that is suitable for the formation of 3D structures by two photon DLW includes at least two components: a monomer or a mixture of monomers or oligomers (with reactive functionalities for the formation of the final polymer), and a photo-initiator that absorbs the laser light to form reactive species that activate polymerisation. Both the photo-initiator and the monomer/oligomer are transparent at the laser wavelength used, so that the laser beam can be focused within the volume of the material without being absorbed at the surface. The photo-initiator must not only absorb at the wavelength of the two photons but must also have a high cross-sectional area of the two photons, which means a high quantum yield of radicals and highly active radical species generated. If these elements are sufficiently strong, the initiator will normally be efficient for two-photon polymerisation.[134] The initiation step of radical chain polymerisation only takes place after the radicals formation that can then proceed to the propagation step. The photo-initiator appropriately inserted into the resit must therefore include a photo-cleavage reaction. The initiators currently on the market can provide two types of photo-cleavage: a Norrish type 1 mechanism and a Norrish type 2 mechanism. The initiators discussed here after (Irgacure 369 or 2-Benzyl-2-dimethylamino-1-(4-morpholinophenyl)-butanone and TPO or Diphenyl(2,4,6-trimethylbenzoyl)phosphine oxide) follow a Norrish 1 type mechanism. Their molecular structure is reported in **Figure 4.3**.

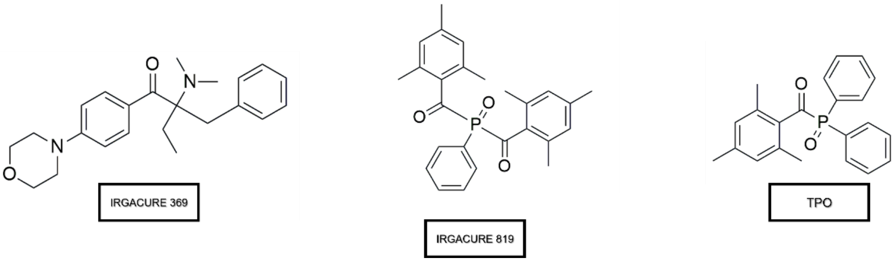

Figure 4.3: Chemical structure of different photo-initiator considered. Examples of Irgacure 369, Irgacure 819 and TPO.

This mechanism involves a homolytic rupture of the C-C bond in the excited triplet state (photo-induced-alpha-cleavage). [135,136,137,138] Many of the initiators that follow this mechanism are aromatic carbonyl systems that form two fragments upon interaction with light. Both fragments, and radicals, take part in the polymerisation process. A diagram of the homolytic break-up for this class of compounds is shown in **Figure 4**.

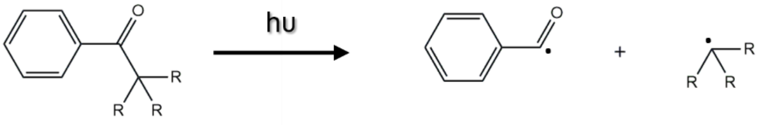

Figure 4.4: General scheme of the photo-dissociation and generation of radical for a carbonyl compound.

Once the radicals have been created, polymerisation then creates a solid resist (initially a liquid) by reaction of the reactive monomer. In the case of an acrylate monomer, which is discussed extensively in the manuscript, the different steps of the reaction mechanism have been shown in the previous sections. The two-photon absorption process and the corresponding two-photon polymerisation begins if there is sufficient energy in the voxel to overcome the threshold and initiate the radical process. This parameter has been quantified and expressed as a light dose reported in **Equation 4.1**:

Equation 4.1

$$D \propto t_{exp} R E_p^N$$

where t_{exp} is the exposure time, R is the laser exposure rate, E_P is the energy of the pulsed laser and N the non-linearity of the absorption process.

In the early stages of polymerisation, the polymer formed is not completely solid but retains a liquid character. This would lead to its removal from the substrate on which it was laid in the subsequent development process by organic solvents. Despite this a certain degree of crosslinking is necessary to create a 'rigid' structure. The family of photoresists that has shown the best performance in two photon DLW, based on a radical polymerisation mechanism, are the acrylate-based compounds. In the field of lithography, this family is referred to as negative-tone, i.e. they have the ability to remain solid once polymerisation is complete and the unreacted monomer can be removed (typically through the use of a photo-resist solvent). One of the resists produced directly by Nanoscribe GmbH and widely used in the field of lithography is IPL-780, which is based on multifunctional acrylates with a controlled refractive index to increase the resolution of the technique.

Although all experiments in this thesis refer to the aforementioned class of acrylate-based photoresists, a wide range of other photoresist systems have also been successfully used for TP-DLW. These include other negative-tone photoresist systems, also based on free-radical polymerisation, hydrogels,[128] SU-8 epoxy-based photoresists, hybrid materials. [139,140]

4.1.4 Stimuli-responsive polymers as photo-resist in TPP-DLW

Miniaturisation of responsive polymers is currently gaining attention due to its potential application in a variety of fields.[141] Smart materials, which respond to external stimuli with a reversible shape-change, are essential elements of new actuators to be employed in microfluidics, [142,143,144]photonics[145] and micro-robotics.[146.147,148,149] These functional devices exploit the so-called 4D printing in which three-dimensional architectures are able to change their properties under a proper stimulus.[150]In this context, Direct Laser Writing (DLW) by two-photon polymerization (TPP) represents a versatile solution for 4D additive manufacturing at length scales ranging from nano to micrometers.[151,152,153] Recently, this technology has been adapted for the fabrication of stimuli-responsive materials, such as hydrogels, at the microscale.[154,155] These materials can generate actuation by reversible swelling and deswelling in aqueous media in response to a physical[156,157] (e.g. above or below a low critical solution temperature) or chemical stimuli (e.g. in response to solvent polarity or sugar concentration).[158,159] However, for a wider range of applications, materials that can actuate themselves in a programmable way, both in dry and in liquids environment, would enlarge the application field. Additionally, achieving anisotropic deformation would enable controllable deformation with particular functionality. Both these aspects find a solution in the use of Liquid Crystalline Networks (LCNs)[160,161] which represent one of the most suitable candidates for smart artificial devices.[162] The first LCNs 3D patterned with DLW were based on nematic monomers,[47] specifically acrylate-based reactive mesogens, that have been demonstrated to generate simple robotic operations. Our research group reported some examples on micro-robots printed by DLW (such as for micro-hands [163], micro-walkers[47] or micro-swimmers[164]), photonic devices (such as diffraction gratings[165] or elastic woodpiles[166]) and opto-mechanical metamaterials. [167] Fabrication of free-standing structures with maximum resolution of 160 nm have been demonstrated.[168] In all the examples, LCN actuation by light[145] has been controlled thanks to an azobenzene dye inserted in the polymeric chains before the polymerization reaction[47] or after it by post functionalization method.[156] Additionally, LC microstructures with structural colour using cholesteric photoresists were demonstrated.[169,170] Among them, interestingly DLW was demonstrated for the preparation of a micro-walker (**Figure 4.5A-B**). Its contractile properties are provided by the liquid crystal mixture used in its production, its own muscle, combined with unresponsive supports (conical legs) that have a certain inclination (produced with IP-Dip) as shown in **Figure 4.5C-D**.

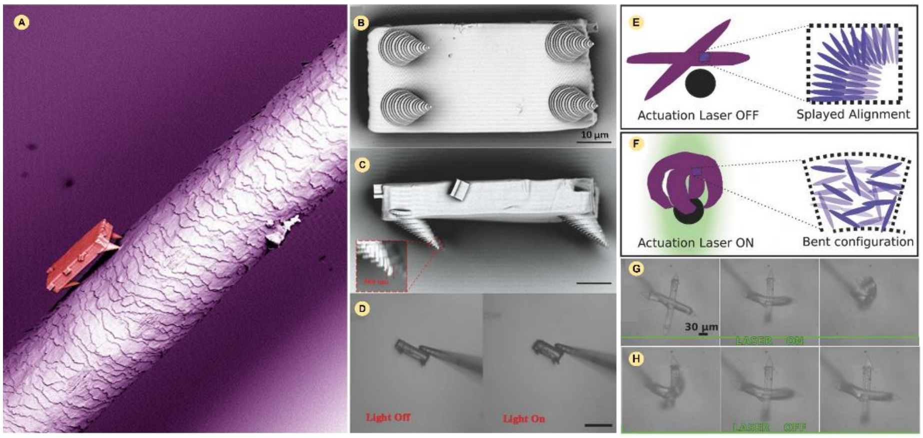

Figure 4.5: Light-fueled micro-walker and micro-gripper based on LCNs. A) Picture of the micro-walker on a human hair. B) Optical microscope image of the design of the legs. C) Optical images of the Micro-walker and the inclination of the legs. D) Light-responsiveness properties of the microstructures. E) Splayed aligned LCNs micro gripper; F) Light-actuation of the gripper. G) Time evolution of the gripper under the light irradiation; H) Reversibility of the actuation when the light is switched off. [47,163] Copyright Wiley-VCH Verlag GmbH & Co. KGaA. Adapted with permission.

Its automation capabilities (walking, jumping or rolling) can be influenced by both the size and geometry (inclination of the conical legs) of the walker and the external environment (i.e., patterned surfaces) with which it interacts.

The possibility of grasping microscopic objects was opened up for the first time with the creation of a light-powered LCN-based micro-gripper. This micro-gripper consists of four 'fingers' capable of bending towards the same point, thanks to a splayed alignment (**Figure 4.5E-F**). Once irradiated by an appropriate stimulus, the fingers switch to a bent configuration, allowing the micro-hand to close and grasp microscopic objects (**Figure 4.5G-H**). The ability to grasp objects can also be made autonomous. Depending on the absorption spectrum of the microscopic object to be grabbed, the micro-gripper performs autonomously tasks grabbing only objects that absorb light thus locally enhancing the temperature that triggers the deformation too (**Figure 4.6**).

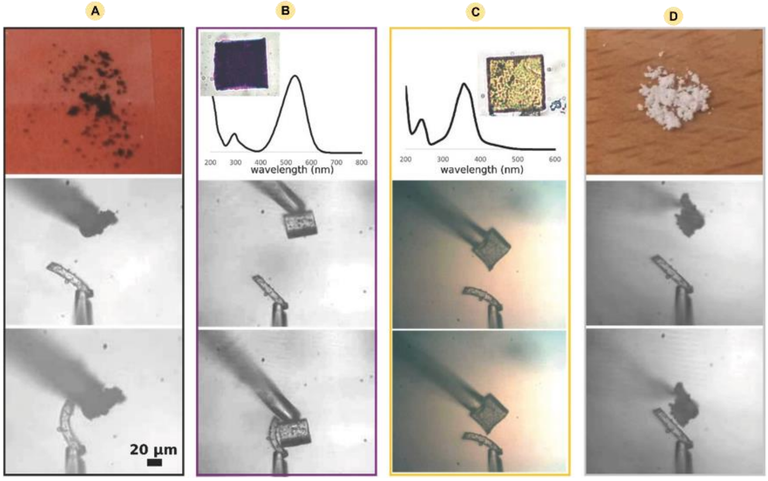

Figure 4.6: Autonomous response of only on finger when in contact with different types of micro-objects. The top panels represent the different objects used: A) carbon nanoparticles, B) purple polymeric block (40 µm × 40 µm × 20 µm), C) yellow polymeric block (40 µm × 40 µm ×20 µm), and D) white TiO_2 nanoparticles. Below, frames of video recorded during the gripping under illumination.[163] Copyright Wiley-VCH Verlag GmbH & Co. KGaA. Adapted with permission.

Photonic tunable structures can be created from polymer matrices. A clear and well-defined example of this has been manufactured from diffraction gratings, produced via DLW-TPP, based on LCN. These manufactured gratings possess a pitch of 1.5 µm and are photo-responsive (**Figure 4.7A and B**). The optical response of the photonic material produced is controlled by a pumping light that deforms the structure anisotropically (because of the homogenous planar alignment).

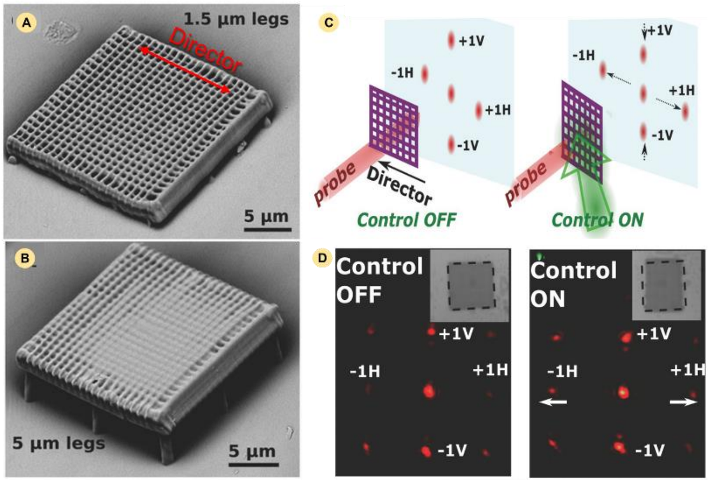

Figure 4.7: 2D LCN grating produced by DLW-TPP. A) Grating with pedestal of 1.5 µm height; B) Grating with pedestal of 5 µm height; C) Design of the beem stereer; D) Diffraction pattern in absence and in presence of the control beam.[165] Copyright Wiley-VCH Verlag GmbH & Co. KGaA. Adapted with permission.

This material behaviour demonstrates a photo-responsive deformable beam steerer fully controlled by light in **Figure 4.7C and D.** The response was estimated in the sub-millisecond time scale.In the field of photonic materials, photonic crystals have the great optical peculiarity of inhibiting the propagation of light over a certain frequency range (stop-band in the case of refractive index differences below 1.9, and full band-gap for high refractive indices).[171] This peculiarity can be exploited in a responsive LCN-based woodpile printed by DLW to create an elastic photonic crystal (**Figure 4.8 A, B and C**).

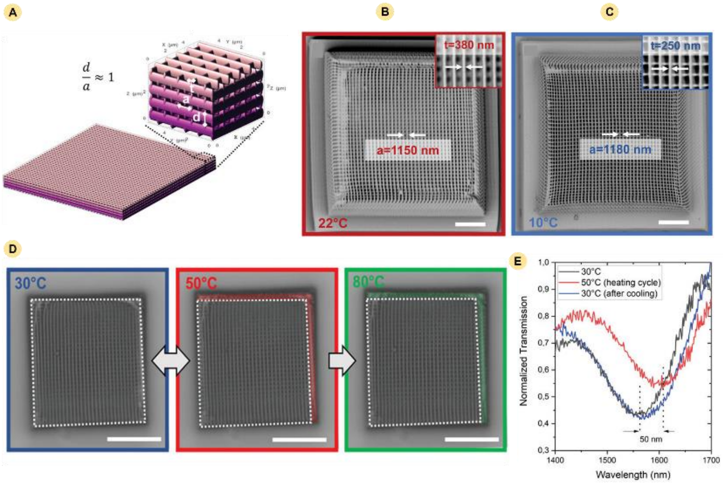

Figure 4.8: Woodpile design and characterization. A) Rendering of the woodpile PC. B) SEM images of the PC woodpiles printed at room temperature C) and at 10 °C; D) Optical images of the woodpile at different temperatures; E) Transmission spectra of the PC woodpile at room temperature (black line), heating the structure at 50 °C (red line) and when cooling down to room temperature (blue line).[171]

The 3D material thus controls the frequency range of the stop-band by a reversible temperature induced mechanical contraction. **Figure 4.8D** shows how these three-dimensional photonic crystals can operate in the telecom range with a 60% attenuation in the stopband and provide, through a change in temperature, a 50 nm shift from this band (**Figure 4.8E**).

To design the properties of LCN microstructures, DLW requires a careful evaluation of two fundamental aspects related to the monomer formulation and printing parameters. Regarding the former, for example, the use of crosslinkers having different steric hindered substituents allows to modulate the weak interaction among LC cores, therefore affecting the actuation and mechanical performances of the polymeric systems.[172] At present, this aspect is barely analysed for 3D printed microstructures, whereas a more common way to control the deformation (extent of contraction, and speed of the response) is to change the crosslinker percentage.[173]

On the other hand, an additional convenient route to modify the microstructures properties is the use of a grey-scale lithographic approach that consists in a careful spatial modulation of the light dose during printing.[174] Lower laser powers lead to a decrease of the crosslinking degree and consequently enable a larger deformation under stimuli.[118] This method has been successfully demonstrated also for hydrogels where, combining regions with different crosslinking density in a single fabrication step led to complex motions under deswelling conditions.[175,176]

In this work, we describe both a chemical approach (changing the crosslinker substituent) and a lithographic one to modulate the shape-changing properties of LCN microstructures. In this way, we found a simple method to combine active deformable elements with different responses (under a constant stimulus) using only one optimised monomer formulation. This combination represents an efficient way to realise, in one lithographic step, reconfigurable pixelated arrays based on a single photoresist. We believe that this advancement will be fundamental in broadening the application of active microstructures, to encode information using physical and miniaturised labels. [177

As a first simple prototype, we demonstrated a micrometric tag with a code that is invisible except under certain environmental conditions. [178,179] During the DLW, hidden information (in this case a letter) has been encoded in LCN elementary units assembled in a 2D array. The elements are indistinguishable from the outside and only using an appropriate reading mechanism, e.g., applying a certain stimulus (e.g light or temperature), they respond differently to show the physical (hidden) data. A second decoding mechanism is possible by observation with polarised light exploiting the birefringence of LCN pixels, allowing to create a multi-level reading of the proposed encryption array. This work was conducted in Trinity College of Dublin under the supervision of Prof. Larisa Florea and Dr. Colm Delaney.

4.2 Result and discussion

Different LCN microstructures were prepared by DLW with a two-photon polymerization (TPP). In this technique, a near-infrared laser (780 nm) is directly focused into a photoresist inserted in a LC cell, as illustrated in **Figure 4.9A**. When the laser intensity exceeds a certain threshold, the photo-polymerization reaction begins, leading to the formation of a solid nano-volume with an ellipsoidal shape (voxel with minor axis dimension around 150 nm and major axis of 400 nm).

The structure of the mesogenic monomers used is reported in **Figure 4.9B**. A mono-acrylate mesogen (C6BP), a diacrylate crosslinker, a photo-initiator (PBPO) and an azobenzene dye have been included in each formulation. All the mixtures contained 20% mol/mol of a crosslinker, 1% mol/mol of photo-initiator and 1 % mol/mol of dye.

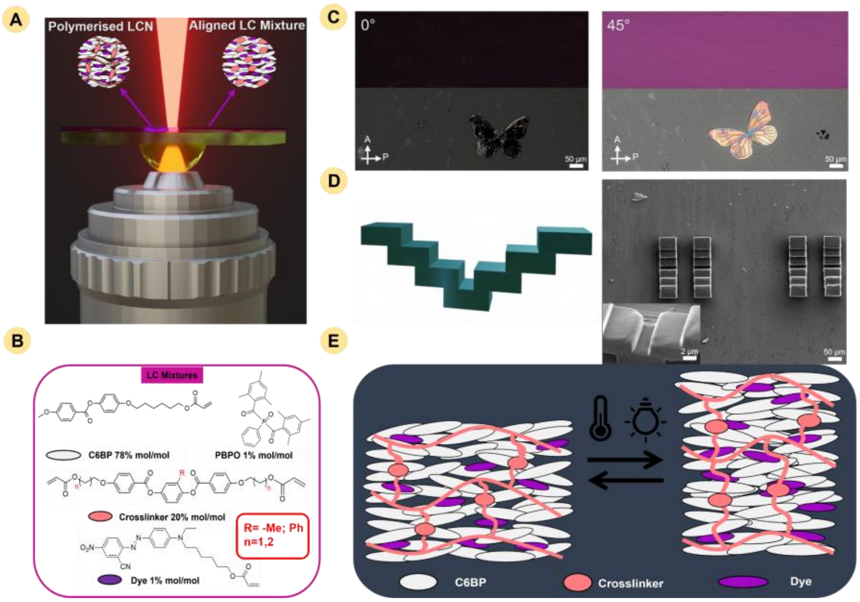

Figure 4.9: DLW-TPP of LCN-microstructures. A) Scheme of DLW two-photon polymerization in oil immersion configuration for a LC cell; B) Chemical structures of the acrylate monomers exploited; C) Observation of the homogeneous planar alignment in LC cells and polymeric structures analysed by POM. Images are taken at 0° and 45° with respect to the main alignment director; D) Example of a design used and SEM images of 4 step-stair microstructures; E) Schematic illustration of the resulting network and its reversible contraction under temperature or light irradiation.

The structure of the reactive crosslinker has been changed in order to optimise the polymer mechanical properties, while the other components remained unchanged. Crosslinkers and material used are the same described in **Chapter 2**. Previous research on macroscopic LCN films revealed that the presence of sterically hindered substituents in the crosslinker weakened the energy between the LC cores, impacting the actuation performance of systems.[78,79,172] The mixture components are homogeneously mixed and infiltrated by capillary force inside a LC cell to obtain the desired alignment at room temperature. The cells were assembled as reported in **Chapter 2** and used to obtain a monodomain planar alignment in the final material.

The good quality of the alignment was confirmed by Polarised Optical Microscopy (POM) as shown in **Figure 4.9C**. Using different mixtures, we explored the fabrication of free-standing 3D micrometric objects as reported in **Figure 4.9D**. The structures were fabricated using DLW on one surface of the aligned cell and subsequently developed in isopropanol to remove the unpolymerized monomers. Scanning Electron Microscope (SEM) images in **Figure 4.9D** show different 4-step stairs printed using LCN3-Me photoresist, demonstrating the possibility to obtain suspended features using the selected monomer mixtures.

For the microstructures, a gradual disordering of the mesogenic units can be triggered under application of stimuli, generating a reversible shape-change and therefore 4D microstructures. The innate temperature sensitivity of the liquid crystal materials results in reversible contractions under heating (**Figure 4.9E**). Alternatively, deformation can be achieved by light irradiation when azobenzene dyes are inserted in the polymer. In this case, the shape-change is driven by the *trans-cis* isomerization of the chromophore and/or light dissipation into heat. [48,87,123,180]

To begin, the mesomorphic properties of the photoresists were investigated using Differential Scanning Calorimetry (DSC) and POM, as previously done in the Chapters **2** and **3**. More information can be found in the Appendix. All photoresists showed a monotropic behaviour (with nematic phase observed only on cooling) and exhibited a LC phase at room temperature, with no crystallisation recorded for several days after the first melting. This property enables easy processing of the material at room temperature and integration into 3D printing and lithographic techniques.[46] All the mixture showed similar enthalpies associated with the LC to isotropic phase transition and were collected in **Table 4.1**.

Table 4.1: **Thermal properties of LC mixtures.** Phase transition temperatures are obtained during the second heating (h) – cooling (c) cycle of DSC experiments (20 °C min^{-1}). Cr: crystalline phase; N: nematic phase; I: isotropic phase. All Temperatures are taken at the maximum of the transition peak. H_m: enthalpy related to the melting peak in the first heating cycle; H_{I-N}: enthalpy related to the isotropic to nematic phase transition in the first cooling cycle.

LC mixture	Crosslinker percentage [%]	Phase transition temperature [°C]	H_m [J/g]	H_{I-N} [J/g]
LCN3-Me	20	H: N 59 I C: I 57 N	72	1.2
LCN3-Me	30	H: N 64 I C: I 61 N	62	0.29
LCN6-Me	20	H: N 65 I C: I 63 N	72	1.3
LCN6-Me	30	H: N 75 I C: I 73 N	70	0.32
LCN6-Ph	20	H: N 42 I C: I 39 N	47	1.2
LCN6-Ph	30	H: N 44 I C: I 40 N	37	0.34

According to **Chapter 3** we verified how the crosslinker structure affects the thermomechanical properties. As demonstrated in **Chapter 3**, increase of flexible spacer in the crosslinker had a negligible effect on glass transition temperature (T_g), while increasing the steric hindrance on the aromatic core (from methyl to phenyl group) lowered the T_g. To better highlight the effect of this central substituent, a Dynamic Mechanical Analysis on LCN6-Me and LCN6-Ph is reported. Storage modulus (E') and loss factor (tan δ) for LCN6-Me and LCN6-Ph films are reported in **Figure 4.10** and representative mechanical parameters are summarised in **Table 4.2**. For the storage modulus (**Figure 4.10A**), the curves showed a sigmoidal trend over temperature. The first plateau of the graph was used to define the modulus in the glassy state while, during the glass transition, the modulus presented a sharp decrease until it reached a second plateau that characterised the rubbery state. For both samples, E’ followed a typical downwards passing from a glass state to a rubber one by increasing the temperature. At room temperature, E' decreased from approximately 1900 MPa to 400 MPa by increasing the steric hindrance. In all the temperature ranges investigated, LCN6-Me presented higher E’ values. The loss factor (tan δ), reported in **Figure 4.10B**, is the ratio between the storage modulus and the loss modulus. The glass transition temperature was defined in this case as the maximum of the tan δ peaks. Differences with the T$_g$ measured by DSC are observed, as normally expected, but also in this case the value decreased increasing the steric hindrance (from LCN6-Me to LCN6-Ph).

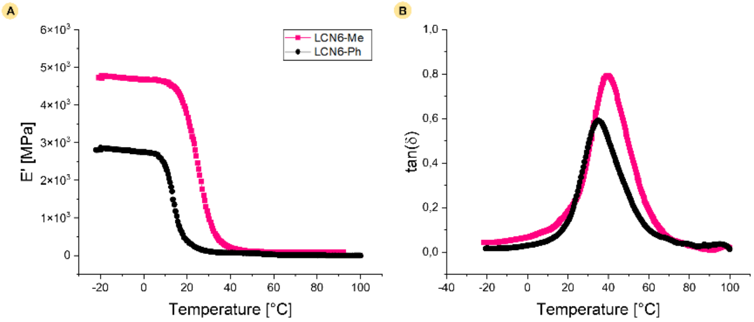

Figure 4.10: Dynamic mechanical analysis on LCN (20% of crosslinker) films (3 °C min^{-1}). A) Trend of the dynamic storage modulus (E′) as a function of temperature. B) Trend of the loss factor (tan δ) as a function of temperature.

Table 4.2: Mechanical properties of LCN films as a function of temperature. E’$_{glass}$: storage modulus in the glass state (determined at -20 °C); E’$_{r.t}$: storage modulus at room temperature (determined at 25 °C); E’$_{rubber}$: storage modulus in the rubbery state (determined at 60 °C); T$_g$: glass transition temperature taken at the maximum of the tan δ. The analytical determination reports the average of the values and the standard deviation made on three different samples for each formulation.

Material	E’$_{glass}$ [MPa]	E’$_{r.t.}$ [MPa]	E’$_{rubber}$ [MPa]	T$_g$ [°C]
LCN6-Me	3328 ± 1980	1925 ± 512	82 ± 20	34± 1
LCN6-Ph	1758± 1488	394± 290	20± 9	29± 3

The mixtures were then employed to realise microstructures with different 3D architectures and increasing complexity. Some design examples are presented in **Figure 11A**.

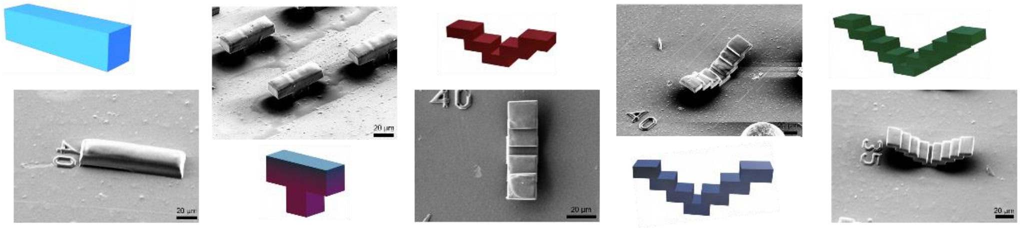

Figure 4.11: Examples of LCN microstructures design and SEM images for different geometries (blocks, tables and stairs).

The structures included a bulk planar structure (directly linked to the surface), a suspended block on a cubic pedestal (called later table) and more complex suspended elements (e.g stairs with different number of suspended steps). For each photoresist, a careful evaluation of the optimised printing conditions was performed. All the designs shown in **Figure 4.11A** were printed in all the mixtures. The fidelity between the design and the resulting structure was evaluated by SEM and Atomic Force Microscopy (AFM). The height profile measure for the case of a 3-step stair design is contained in **Figure 4.12** showing good reproducibility of the design during the printing.

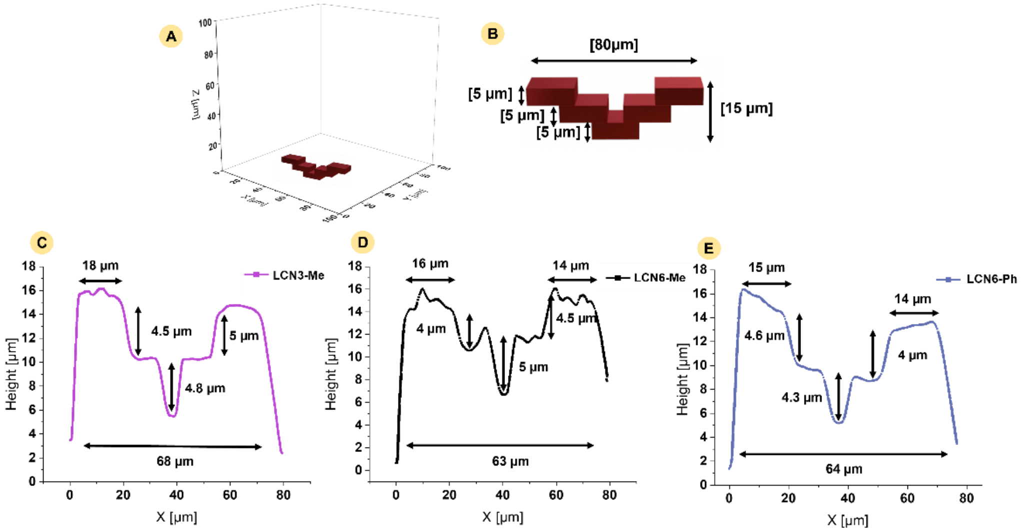

Figure 4.12: AFM characterization for micro-stairs. A) 3D model of microstructures. B) Scheme reporting the theoretical dimensions of 3-step-stair. C) Graph reporting the heights of 3-step-stair printed by LCN3-Me mixture. C) Graph reporting the heights of 3-step-stair printed by LCN6-Me mixture. D) Graph reporting the heights of 3-step-stair printed by LCN6-Ph mixture.

In general, we observed that the change of slicing (from 0.1 to 0.5 µm) and hatching distances (from 0.1 to 0.5 µm) (that are respectively the separation between two consecutive layers and two consecutive beam scans in the plane) during the writing have a smaller effect on the final structures than that of laser power, scan speed, and geometry design. Height of the structures was screened (from 10 to 20 µm) as proof of the great influence that can have on the morphology of microstructures. An example was reported in **Figure 4.13**.

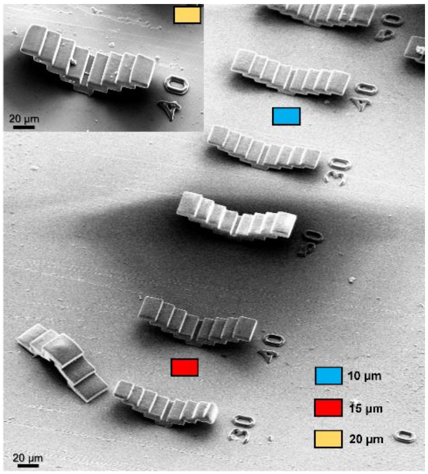

Figure 4.13: Height influence on microstructures morphology (blocks and stairs).

The optimised parameters to obtain well defined microstructures were 40 mW as laser power (LP) and 10 mm s^{-1} as scan speed (SS), for LCN3-Me and LCN6-Me, and 50 mW and 10 mm s^{-1} for LCN6-Ph. For the latter, a slightly higher power was needed as suggested also by its softness with respect to the other mixture. The degree and reproducibility of the shape-change, owed to thermal-actuation, was investigated across several heating-cooling cycles. An example of the thermo-actuation of a micro-stair prepared by LCN3-Me is reported in **Figure 4.14**.

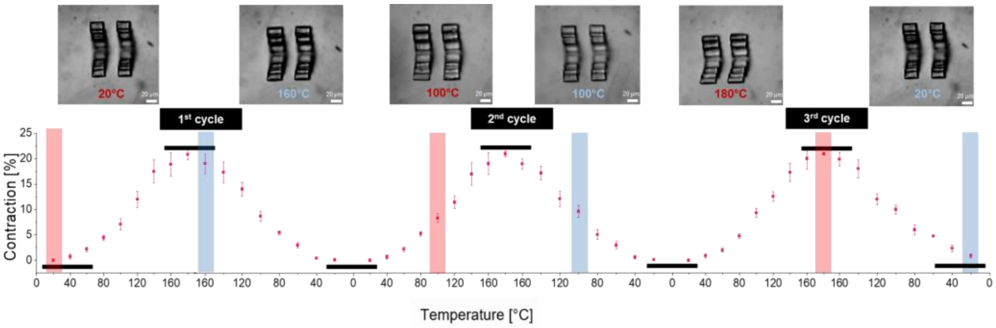

Figure 4.14: Optical microscopy images and graphs of contraction during a thermal actuation test (from 20 °C to 180 °C). Test reported refers to a 4-step-stairs fabricated from LCN3-Me. Error bars indicate the standard deviation for each point.

The graph reports the contraction (C_T) at different temperatures, as defined by the following **Equation 4.2**:

Equation 4.2 $$C_T[\%] = \left(\frac{(L_0 - L_f)}{L_0}\right) * 100$$

where L_0 and L_f are the lengths measured respectively at room temperature and at a specific temperature (during heating or cooling) of the object considered. Each L_0 and L_f was measured for different structures in three different positions (centre and both sides) as shown for a 4-step-stairs and a table respectively made of LCN3-Me and LCN6-Ph in **Figure 4.15.**

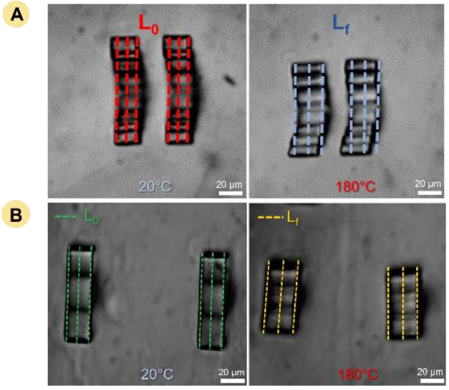

Figure 4.15: Example of contraction analytical determination during the thermal actuation. A) Pictures report the measure of the initial and final length of a LCN3-Me 4-step stair at room temperature and at 180 °C. Each length is taken as an average of the three values and their standard deviation. B) Pictures reporting the initial and final length reached under thermal stimuli of a LCN6-Ph table. Each length (L_0 and L_f) used in the **Equation 4.2** is an average of three different measurements (centre and sides of the structures) made for three different structures.

As expected, during heating, a gradual contraction was obtained along the nematic director. According to the graphs, a contraction was obtained starting from 40 °C and, at 180 °C, a maximum shrinkage of 21±1% was obtained. As it cooled, the structure followed the reverse evolution of shape, with the length of the scale gradually increasing until it recovered its original shape around 40 °C. By repeating the heating and cooling cycles (3 cycles are shown in **Figure 4.14**), the process was demonstrated to be fully reversible. To be noted that the actuation data reported in this paragraph (**Figures 4.14 and 4.16**) are given as a medium contraction measured on 10 structures printed with the same parameters, demonstrating the high reliability of the fabrication process and material chosen.

Engineering the material deformation under stimuli is one of the most important parameters to develop application in soft robotics and photonics where a precise control on the (3D) shape under stimuli is needed. In general, improving contraction (under the same stimuli), decreasing the temperature needed for the actuation and combining parts that deform differently are the three main goals in developing new polymeric actuators. Towards these objectives, an investigation of thermally-induced contraction of suspended microstructures has been reported in **Figure 4.16** trying to understand possible contributions due to the different mixtures and printing parameters. The study has been conducted on structures with less complexity than the stairs but still preserving suspended elements. In particular, we analysed "tables" consisting of a simple block suspended on one cubic central pedestal. The printing parameters were again screened, as in the previous case, and evaluated both via imaging and deformation capability. **Figure 4.16A** depicts optical microscope (bright field) images of a micro-table taken at specific temperatures during the heating cycle of actuation, while **Figure 4.16B** shows the graph comparing the thermal-actuation of structure written under the same conditions (40 mW as laser power and 10 mm s^{-1} as scan speed, where slicing and hatching distance were set at 0.1) but using the different mixtures. This finding demonstrates that LCN6-Ph has considerably superior actuation qualities than the other materials with a maximum contraction at 180 °C of 27±1% (with respect to 15 ±1% for LCN3-Me and 14 ± 2% for LCN6-Me). Interestingly, the graph demonstrated that we are able to print the same micron-sized structure in all the photoresist but obtaining differences in shape under temperature actuation. This should allow the production of LCN microstructures with different deformation under a constant stimulus (e.g. a certain temperature of the sample) by sequential fabrication steps of LC photoresists.[75] However, this preparation method employed multiple writing steps, multiple solvent developments and multiple alignment procedures. Avoiding these fabrication steps, still achieving differential deformations in structures made by a unique writing step [176] will open to easier integration of parts that deform differently in the same device.

For this reason, we studied a grey-scale actuation (i.e., a different contraction under the same flat stimulus) of the microstructures prepared from a single resist. The micro tables have been prepared within the photoresist that offers the greatest contraction (LCN6-Ph), employing different writing parameters (grey-scale lithography approach). Examples of the thermal contraction for micro tables produced by the grey-scale approach have been reported in **Figure 4.16C**.

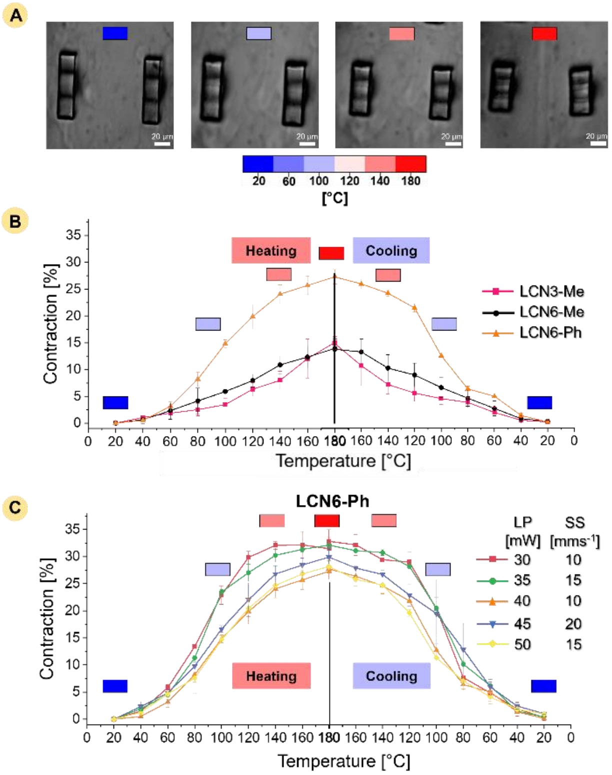

Figure 4.16: Comparison of thermal deformation for LCN microstructures prepared with different monomer mixtures and printing parameters. A) Bright field images of LCN6-Ph tables at different temperatures to demonstrate the thermal actuation. B) Comparison of contraction reached by micro tables realised with different photoresists (printed using 40 mW LP, 10 mm s^{-1} SS, 0.1 µm for slicing and hatching distance) C) Comparison of contraction reached by micro tables realised with LCN6-Ph mixture at various laser powers and scan speeds. Error bars shown in the graphs are referred to the standard deviation of the data represented for the same structure (same parameters) printed several times.

As can be observed, the curve trends are all comparable, but the extent of the contraction can be programmed using the printing parameters. In particular, the tables produced with 30 mW laser power and 10 mm s^{-1} scan speed exhibited the maximum shrinkage of the series (32 % at 180 °C) with the most notable difference being observed above 120 °C. This means that to obtain an appreciable grey-scale actuation a certain temperature threshold has to be overcome. Analysing only one writing parameter, we observed as the maximum contraction decreased by increasing the laser power (at the same laser scan speed) probably due to an increased crosslinking density.[118,141] Even if the contraction difference within this approach is smaller than the one obtained by combining different photoresist, the easy integration of these structures should be applied in devices that need multiple shape-changing elements in an integrated system. An example should be physical encoding devices where a digital information is hidden in the material pixel properties (e.g., shape, colour). For a clearer comparison of the actuating properties, other details related to the effect of the crosslinker percentage (**Figure 4.17** and **Table 4.3**), and microstructure shape (**Table 4.4**) are reported.

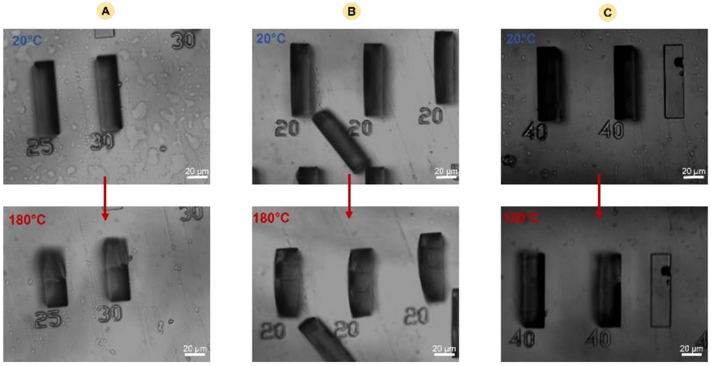

Figure 4.17: Actuation under temperature variation for blocks printed using monomer mixtures containing the crosslinker CL3-Me at different concentrations. A) Optical images of blocks prepared with 20% of crosslinker and their thermal contraction; B) Optical images of blocks prepared with 30% of crosslinker and their thermal contraction; C) Optical images of blocks prepared with 40% of crosslinker and their thermal contraction.

Table 4.3: Comparison of contractions obtained for microstructures prepared using mixtures with different crosslinker concentration and different laser powers (mW). The contraction percentage has been measured at 180 °C on block design (e.g. **Figure 4.17**). The average value and its standard deviation have been determined by three different measurements for three different samples. Scan speed was set 10 mm s^{-1}; Slicing and hatching distance set 0.1 μm for all the data. NP indicates the limit of printability of the photoresist. In all cases, the analysis demonstrates that increasing the crosslinker content or increasing the laser power lead to a decrease in the microstructure deformation. In accordance with data reported also, the molecular parameters (in this case Figure, the crosslinker content) play a bigger role than the fabrication parameter for the optimization of the shape-changing behaviour.

Crosslinker percentage	**Contraction percentage [%] @ Printing laser power [mW]**			
	20	**30**	**40**	**50**
CL3-Me				
20%	22 ± 2	15±1	13 ± 1	NP
30%	7 ± 1	5 ± 1	4 ± 1	NP
40%	4 ± 0.4	3 ± 1	2 ± 0.5	NP
CL6-Me				
20%	7 ± 2	6 ± 1	4 ± 2	NP
30%	5 ± 1	4 ± 1	2 ± 1	NP
CL6-Ph				
20%	9 ± 1	14 ± 4	23 ± 2	22 ± 6
30%	5 ± 2	12 ± 4	24 ± 1	25 ± 2

Table 4.4: Comparison of contractions obtained for different structures prepared by LCN6-Ph mixture. All the structures were printed in the same condition (50 mW as laser power, 10 mm s^{-1} as scan speed, 0.1 as slicing and 0.1 as hatching distance) and the contraction was determined 180°C. The average value and its standard deviation have been determined by three different measurements for three different samples. The analysis demonstrates how the substrate anchoring can limit the material deformation, with the suspended table giving the maximum contraction in the series.

Structure	**Maximum Contraction [%]**
Block	23% ± 3
First stair step	28%±4
Table	33%±1

In general, a higher crosslinker content leads to smaller deformation, while the substrate strain can influence the contraction of structures prepared by the same material and parameter. For this reason, all the comparisons already presented have been made using the same geometry and dimension of a suspended design (to reduce the strain and increase the possible deformation). A proof-of-concept for encryption and physical decoding of basic information (in this case a letter) using the shape-changing behaviour of LCN microstructures is reported in **Figure 4.18**. The letter was codified in a matrix of 20 pixels (5 columns by 4 rows) that are initially indistinguishable (the letter was hidden) as depicted in **Figure 4.18A**. However, the binary elemental units can be differentiated by their response to thermal stimuli. For example, the array can be prepared with materials that have different contraction under temperature variation, thus the thermal stimulus can be used to obtain different shapes between the pixels to reveal an identifiable letter. The pixels in **Figure 4.18** are called as “1” with larger or “0” with minor or no deformation.

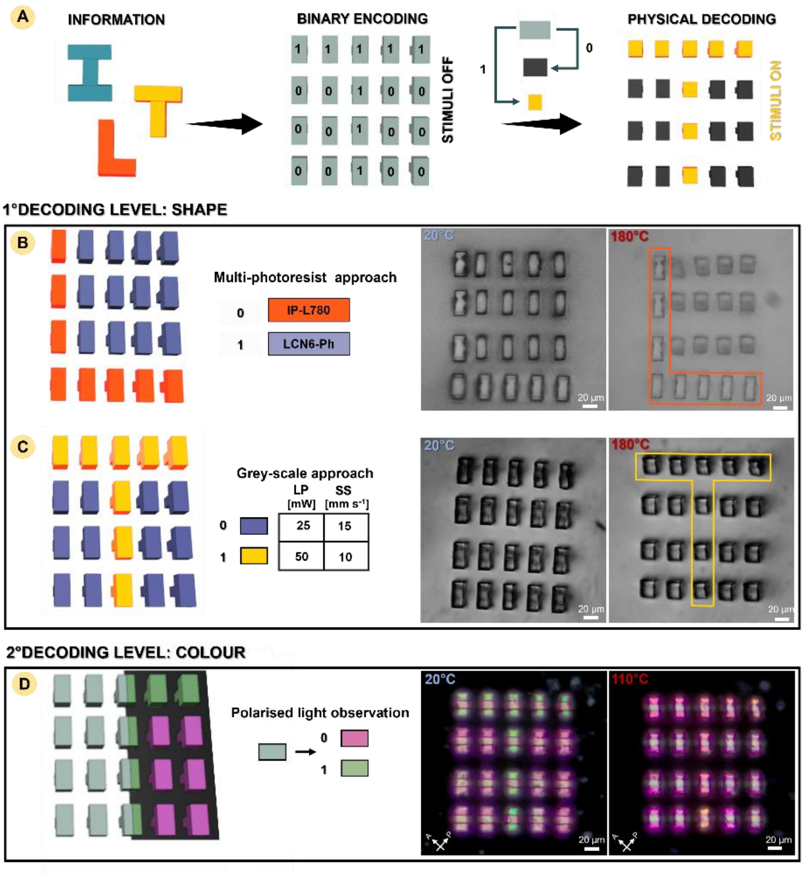

Figure 4.18: Hidden physical information encoding into a microstructure pixel array. A) Concept for the realisation of encoding information as binary code in a pixelated array. Physical revelation is possible under external stimuli. B) Scheme of fabrication of a pixel array by a multi-resist approach and optical images of its realisation. LCN6-Ph and IP-L-780 have been used to prepare the pixels that are printed in the same conditions (50 mW and 10 mm s^{-1} ; slicing and hatching distance 0.1 µm. Under thermal revelation, only the LCN pixels undergo a shape deformation; C) Scheme of fabrication of an LCN pixel array by a grey-scale approach and optical images of its realisation. LCN6-Ph mixture was printed with different parameters for different pixels (50 mW and 10 mm s^{-1}; 25 mW and 15 mm s^{-1}). Under thermal revelation, the two types of pixels contract in a different way; D) Scheme of physical decoding by observation with polarised light and optical images of its realisation and variation of pixel colour under thermal stimuli.

In the first example (**Figure 4.18B**), a letter has been encrypted in the array of pixels prepared by a multi-material fabrication to combine LCN microstructures with a non-responsive commercial photoresist (IP-L 780) in a two-step protocol. The micro table design has been taken as basic elements and the two materials are printed under the identical experimental conditions (50 mW LP and 10 mm s^{-1} SS). In the first step, the LC microstructures were printed and developed. Afterwards, the other pixels were fabricated using IPL-780. As shown, the final array was composed of multi-material structures without any discernible difference between pixels. During the heating stage, the selective shrinking of the LCN components (with the others that do not change shape) allows for the pattern to be clearly revealed. However, toward a further miniaturisation and higher scalability of similar smart tags, the use of a simpler and more reliable fabrication protocol is desirable. To this end, a second example of letter encoding was realised with a grey scale approach using LCN6-Ph in a single fabrication step as shown in **Figure 4.18C**. The micro tables have been printed using two different writing parameters to maximise the different length under actuation (pixels "0" were printed with 25 mW LP and 15 mm s^{-1} SS, and pixels "1" with 50 mW LP and 10 mm s^{-1} SS). Also in this case, at room temperature, all the pixels were completely indistinguishable, and the letter "T" cannot be recognized. Upon heating the array, all the pixels contracted but with a different extent (as effect of different light dose applied in the fabrication) and making the letter identifiable. An enlarged image of different pixel responses created by the grey scale approach is reported in **Figure 4.19**.

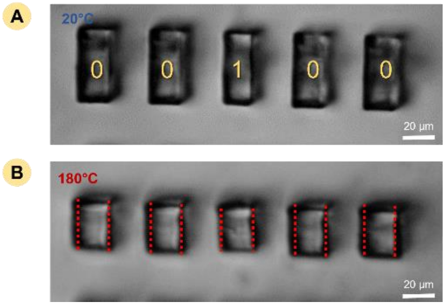

Figure 4.19: Comparison of contraction in a binary encoded array. A) Picture of 5 LCN pixels used for binary encoding by grey scale approach at room temperature (A) and at 180 °C (B). At high temperature, the contraction difference can be used for the revelation of "1" pixels.

For both approaches, once the temperature was cooled down, the letter was hidden again thanks to the process reversibility, as previously discussed. This represents a first decoding level which is based on the physical shape variation of the responsive pixels. Therefore, other examples are reported in **Figure 4.22 and 4.23** in the experimental section.

Additionally, when the arrays are observed by POM, another level of identification can be built thanks to the pixel birefringence opening to a multi-level reading of the responsive tag. In this case, the pixel structural difference can also be appreciated by POM using a different detection/encryption mechanism (**Figure** 4.**18D**). Observing the sample at 45° with respect to the analyzer, the two kinds of pixels show different colours based on writing parameters. This is a result of the refractive index and block height variation during the fabrication.[125,182] Here, the letter was completely visible at room temperature, but as the temperature rose, the information was hidden, displaying the opposite behaviour than in the prior situation. So, for each kind of pixel, it is possible to associate different colours at different temperatures as an additional level of information or secure identification. For the array prepared by the multi-photoresist approach, only the LCN pixels present birefringence (and so the possibility to show different colours) and the letter can be recognized both at room temperatures and at higher ones. Combining the 3D geometry, its variation with time depending on an external stimulus and consequently the variation of intrinsic material properties such as the molecular alignment, also the birefringence varies resulting in differently coloured structures at the polarised optical microscope. This interconnected variation of 5 (geometry+time+birefringence) expands the field of 4D microstructures to 5D functional actuators. An overall observation is that the pixelated array can have two different levels of encoding, that are based on two physical mechanisms, one optical (using no polarised or polarised light) and the other due to shape adaptation in response to the environmental stimuli such as heating. Finally, decoding based on physical deformation has also been tested using light. The azo-dye showed a maximum of absorption around 535 nm, thereby enabling deformation by green light irradiation. Using this stimulus for the letter decoding, it was possible to obtain an average of contraction of 33±1% and 22±1%, respectively for the pixels “1” and “0” (**Figure 4.20)**.

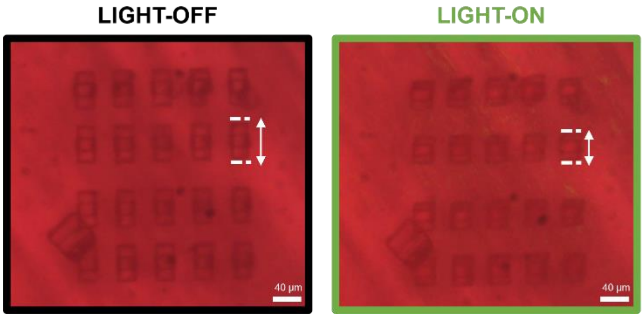

Figure 4.20: Example of light-induced deformation. Optical image of LCN microstructures before (on the left) and during (on the right) irradiation with a green laser.

After switching off the light, the pixels recovered the original shape. The use of light allows us to improve the response time of the realised system from seconds or minutes (such as in the case of temperature, depending on the heating system used) to milliseconds. Another example was reported in **Figure 4.21.**

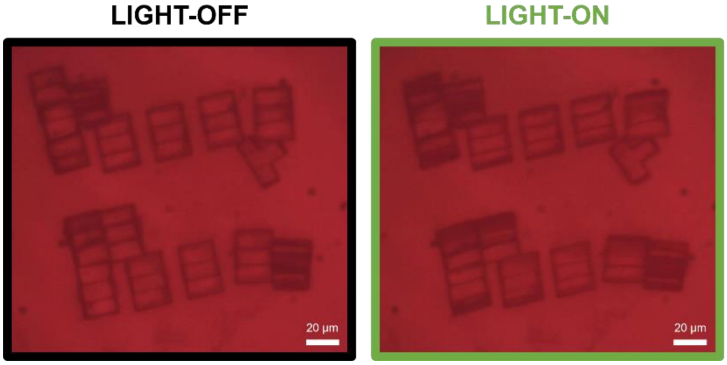

Figure 4.21: Example of light-responsiveness of LCN microtag. Contraction average: 28%±2

In our case, the light actuation rate has been estimated as 0.25±0.03 µm ms^{-1} and 0.23±0.02 µm ms^{-1} respectively for the pixels “1” and “0” during the contraction stage and 0.19±0.03 µm ms^{-1} and 0.17±0.03 µm ms^{-1} during the recovery stage. Comparing the label with other examples of information storage devices, the use of LCN presents some innovative features. In addition to the aforementioned reversibility of the micro-pixel contraction (to enable multiple reading and hiding cycles), we demonstrated how the double encryption mechanism allows us to store more rich information in the same label. We can encrypt both a letter and a colour, not being limited to only one of the two as reported in many other responsive labels, based on emission phenomena or structural colour.[183] The dual encryption mechanism can also improve the trustworthiness of labels for multi-level identification. The system speed is in the millisecond scale (using light). Moreover, the few known examples of information encryption based on material shape-change are based on solvent swelling or vapour absorption [184,185] therefore needing a specific environment. In the case of LCN deformation, the decoding could be triggered both in air or liquid since it depends only on the material properties and on the external stimulus.

4.3 Conclusion

We reported on the realisation of materials with micrometric resolution and programmable actuation that can be controlled by varying fabrication parameters, such as the laser power and the scan speed. We demonstrated the possibility to obtain 3D and suspended micro-objects with increasing degree of complexity and fully reversible contraction under temperature variation or irradiation with light. First, different reactive LC crosslinkers have been used in the photoresist to determine their impact on the final material properties. During heating, materials containing CL6-Ph presented the best shape-changing properties (with an average maximum contraction of 33%). Moreover, modulating the writing parameters, the maximum deformation achieved starting from the same LC mixture can be tuned. This opens the way to one-step fabrication of composite devices having parts that respond in a different way to the same stimulus.

This concept has been applied for a simple system of physical information encryption based on the different shape-change of two kinds of pixels (prepared with a grey-scale approach or using two photoresists), so the letter is hidden at room temperature and shown under a proper external stimulus. Moreover, the colours that arise from the different pixels by illumination with polarised light can be exploited as a second level of information encoding. In this case, the letter is visible at room temperature and a colour difference is decreased by heating. All these effects can be combined together to realise multi-level reading of a responsive tag. In practice this is achieved by combining the mechanical response of the pixels containing the written information with their different colour obtained at different temperatures. Even if this encoding strategy needs further development (e.g., by improving the differences in contraction or by decreasing the actuation temperature), our first demonstration enlarges the range of possible applications of liquid crystalline network microstructures in the field of robotics, photonics, and beyond. These DLW microstructures will allow the building of more sophisticated physical information storage devices and opto-mechanical structures with improved functionalities, e.g., microrobots that respond with complex motion under constant stimuli through appropriate engineering of the local degree of crosslinking in 3D space.

4.4 Experimental Section

Materials: Monomer mixtures contains mesogen C6BP (78% mol/mol), one of the crosslinker CLX-Y (20% mol/mol), Phenylbis(2,4,6-trimethylbenzoyl) phosphine oxide (PBPO, 1% mol/mol) and the acrylate dye (E)-6-((4-((2-Cyano-4-nitrophenyl) diazenyl) phenyl)(ethyl)amino)hexyl acrylate (1% mol/mol). C6BP (4-Methoxybenzoic acid 4-(6-acryloyloxyhexyloxy)phenylester),CL3-Me (1,4-Bis-[4-(3-acryloyloxypropyloxy)benzoyloxy]-2-methylbenzene, also known as RM257) and CL6-Me (1,4-Bis-[4-(6-acryloyloxyhexyloxy)benzoyloxy]-2-methylbenzene also known as RM82) were purchased from were purchased from Merck. CL6-Ph was previously synthesised by our group and used as synthesised. [172]

LC cell preparation: microscope cover slips (170 µm thick) were spin coated with a polyimide (grade 5291, type 062B Nissan polyimide Varnish, Nissan Chemical Industries), heated at 90 °C for 1 minute and subsequently at 180 °C for 30 minutes. Then, the coverslips were rubbed unidirectionally with a velvet cloth. Two slides (one circular with a diameter of 24 mm and one square with a width of 16 mm) separated by 50 µm microspheres as spacers were used to build the LC cell. The mixture was heated to the isotropic phase, infiltrated by capillarity in the LC cell, and then cooled to room temperature to achieve a monodomain homogeneous planar alignment.

Direct Laser Writing Fabrication: the 3D structures were created using a commercial DLW workstation, Photonic Professional Nanoscribe GmbH, by a two-photon polymerization process. The system employs a 780 nm, 170 mW femtosecond solid-state laser that generates 120 fs pulses with an 80 MHz ± 1 MHz repetition rate. A 63x objective (NA = 1.4, WD = 190 µm (Zeiss, Plan Apochromat) was used in oil-immersion configuration. A 3D galvo translation stage was used to manage sample location. The LC cell filled with the aligned monomer mixture was placed on the sample holder and a drop of oil (Zeiss Immersol 518F) was applied in the centre of the round glass. For all structures, the scan speed (SS) was varied between 10 and 20 mm s^{-1}, the laser power (LP) was modulated between 20 and 50 mW. Laser power listed in the Chapter are related to the power voltage measured by the photodiode. We should affirm that, given that this value does not take into account losses in the system, the sample plane should have a lower value. Slicing distances ranging from 0.1 to 0.5 µm and hatching distances ranging from 0.1 to 0.4 µm were explored. Slicing and hatching distance variation has a minor impact on the actuation property of the microstructures produced compared to one observed for the variation of the LP and SS. For the fabrication it was decided to set hatching distance and slicing at 0.1 µm, which gave the best results in terms of morphology and actuation obtained, and vary only LP and SS. After fabrication, structures were developed in isopropanol (70 °C) to remove remaining unpolymerized photoresist. The 3D structures were designed in Blender and then imported into DeScribe software.

Material characterization: A thin film for each photoresist was produced by infiltrating LC cells with the mixture followed by polymerization by UV irradiation of the whole cells for 10 minutes at 25 °C, and 10 minutes at 45°C to ensure a complete polymerization. Phase transition temperatures of mixtures were measured by DSC TA Instruments Calorimeter Q-2000 (TA-Instruments, Milan, Italy) in a nitrogen atmosphere (heating and cooling rate: 20 °C min^{-1}). Polarised Optical Microscopy was performed with a Zeiss Axio Observer A1 microscope in cross-polarized mode equipped with a Linkam PE120 hot stage and an Axio camera. DMA was carried out using a Perkin Elmer DMA 8000 in tensile mode.

Mechanical characterization of bulk LCN films: Dynamic Mechanical Analysis (DMA) was carried out using a Perkin Elmer DMA 8000 analyzer in tensile mode. The measurements were performed in the parallel direction with respect to the LC alignment as a function of temperature. A scanning rate of 3 °C min^{-1} was chosen. The analyzer was equipped with a rectangular tension geometry and specimens with the size of 8x2x0.015 mm^3 were employed. A strain amplitude of 0.25% (linear viscoelastic range) and 1 Hz of frequency were chosen.

Microstructures characterization: SEM was performed using Zeiss Ultra scanning electron microscope, operating at 5 kV under SE2 mode. Prior to imaging, a Au-Pd nano-scale thin layer (~20 nm) was coated on the polymer structure as a conductive layer under argon atmosphere by sputter coating (Cressington sputter coater 208HR). The Ag-Pd target was purchased from TED PELLA INC. AFM was performed on a commercial SPM system (MFP-3D, Asylum Research, USA) on the micro-fabricated 3D structures. Imaging in air was performed in contact mode at 25 °C.

Thermal-actuation of the microstructures: deformations under temperature variation were observed on an Olympus Microscope combined with a hot stage. A Thorlabs checking temperature system with a thermocouple was directly connected to the glass. Pictures in the Bright Field (BF) were acquired every 20 °C and used to estimate the contraction along the nematic director. 3 cycles of heating and cooling for each structure were acquired to underline the reversibility of the actuation.

Light-actuation of the microstructures: Microstructures were irradiated with a chopped (10 Hz) DPSS 532 nm laser through a 10x, 0.25 NA (Plan Achromat, Olympus) objective placed above the sample. A flat illumination (round area of 400 μm radius) over the microstructure array was employed. The light intensity was measured by a power meter after the objective and a movie was recorded by a CCD camera.

Other examples of micro-tags LCN based

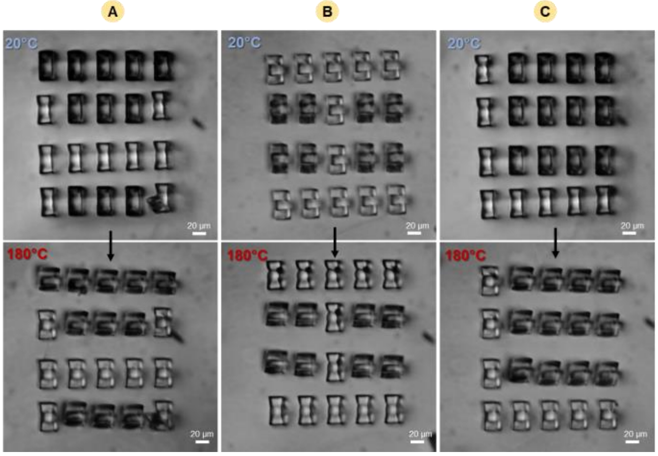

Figure 4.22: Examples of micro-tags made in two different steps (multi-resist approach) based on LCN and IPL-780. A) Hidden letter (H) at 20°C and revealed 180°C. B) Hidden letter (I) at 20°C and revealed 180°C. C) Hidden letter (L) at 20°C and revealed 180°C.

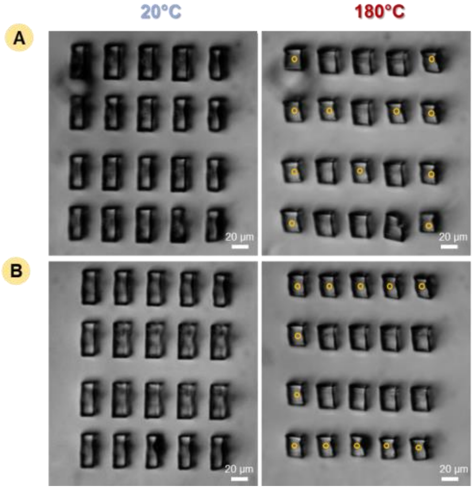

Figure 4.23: LCN microtags with greyscale approach. A) Letter M before thermal stimuli and under heating (180°C). B) Letter C before thermal stimuli and under heating (180°C).

Chapter 5

Conclusions

This work shows how the molecular structure of mesogenic crosslinkers represents a key parameter to modulate both mechanical properties and light response in Liquid Crystalline Networks prepared by free radical polymerization of acrylate-based monomers. These materials are among the most promising smart polymers to develop biomedical applications and microrobots.

Regarding the chemistry chosen for the LCN preparation, the use of light-induced free radical polymerization ensures the realisation of both macroscopic thin films and microstructures by the use of DLW, opening to different scales and therefore applications.

In the first part of the thesis, the synthesis of a small palette of new mesogenic crosslinkers is reported showing how the modification of the crosslinker cores (by the use of steric hindered substituents) can play a crucial role in determining the mesomorphic behaviour of such molecules. In particular, using different substituents (different numbers of methyls, phenyl or tert-butyl units) it is possible to decrease the nematic to isotropic phase transition temperature and to enlarge the range of thermal stability of the LCs phase. The synthetic strategy reported is based on a common benzoic acid derivative that is employed for esterification with different hydroquinones to modify the aromatic rigid core of the crosslinkers. The common building block was prepared starting from the 4-hydroxybenzoic acid in two steps, comprising a Williamson reaction to introduce the flexible spacers and treatment with acryloyl chloride to introduce the polymerizable group. Different conditions were also screened in order to optimise the production of the various molecules, that are all prepared in only three steps with high yield and purity.

In the following parts of the work, the new molecules have been studied for the preparation of different monomer mixtures to possibly identify a correlation between the molecular structure of the crosslinker and the thermo-mechanical and actuation properties of the LCNs.

In terms of the mechanical characteristics of thin films (to be used as artificial muscles), bulky substituents added to the crosslinker core typically result in a higher degree of elasticity (Young modulus less than 4 MPa for LCN6-Ph_{10}) while playing with the content of the cross linker leads to increase the stiffness in some cases (Young modulus up to 88 MPa for LCN6-Me_{30}). Also, the highest photo-actuation capacities were shown by LCN6-Ph, LCN6-tBu, and LCN6-Me in terms of tension generation and activation rate. LCN6-Ph and LCN6-tBu, create greater tension than the reference LCN3-Me if the contraction time course is in the range of 200–400 ms (as in the case of the human myocardium). Interestingly, LCN6-Ph and LCN6-tBu exhibit similar contraction kinetics compared to the reference one. When the content of the crosslinker was increased, materials exhibit distinct behaviours in terms of tension generation under irradiation and, in general, the activation kinetics was lowered demonstrating a detrimental effect for the application as artificial muscles.

Comparing all the analyses proposed, we can conclude that LCN6-Me_{10} represents the best compromise in terms of tension developed and time of contraction. Such materials will be further tested for the development of application in the field of tissue engineering and within the already mentioned REPAIR project.

Regarding the 3D printing process by two-photon DLW, we demonstrated 2D and 3D LCN structures with sub-micrometer resolution. The high power of laser used to achieve the two-photon absorption is compatible with the LC mixture used and the final structures maintain the liquid crystalline properties and the possibility to be activated by light performing deformations. We demonstrated that DLW can be used to integrate microstructures based on different materials on the same surface as well as a free form design of 3D LCN structures. Combining different crosslinker molecular structures with a screening of the printing parameters (e.g., laser power and printing speed) leads to improvement of the quality of the produced suspended microstructures and their fidelity to the CAD design used. Also in this case, the material deformation is greatly influenced by the choice of the crosslinker, with bigger thermal contraction from microstructures prepared by CL6-Ph with respect to the ones having the methyl substituents. Interestingly, starting from the same LC mixture, we investigated how the deformation under stimuli can be modulated by adjusting the writing parameters, which affect the crosslinking degree of the systems. Indeed, the application of different writing parameters during the same printing step can be used to fabricate composite devices, with parts that deform differently under the same flat stimulus.

In the last part, a new possible application of DLW microstructures prepared by LCNs has been described. In particular, a basic physical information encryption system based on the distinct shape-change of two kinds of pixels has been implemented. This allows, for basic information (in our case, a letter), to be hidden at room temperature and revealed when the appropriate external stimulus is provided. By exploiting the birefringent properties of LCNs a second level of information encoding can be used taking advantage of the colours that result from pixels when observed with polarised light. Multi-level reading of a responsive tag is possible by combining both effects. Although this encoding strategy should need further improvement (e.g., by increasing the contraction differences or lowering the actuation temperature), we believe that through appropriate engineering of the local degree of crosslinking in 3D space, these LCN microstructures will enable the construction of opto-mechanical structures with improved functionalities and more sophisticated physical information storage devices.

Appendix

Mesomorphic properties of liquid crystalline crosslinkers

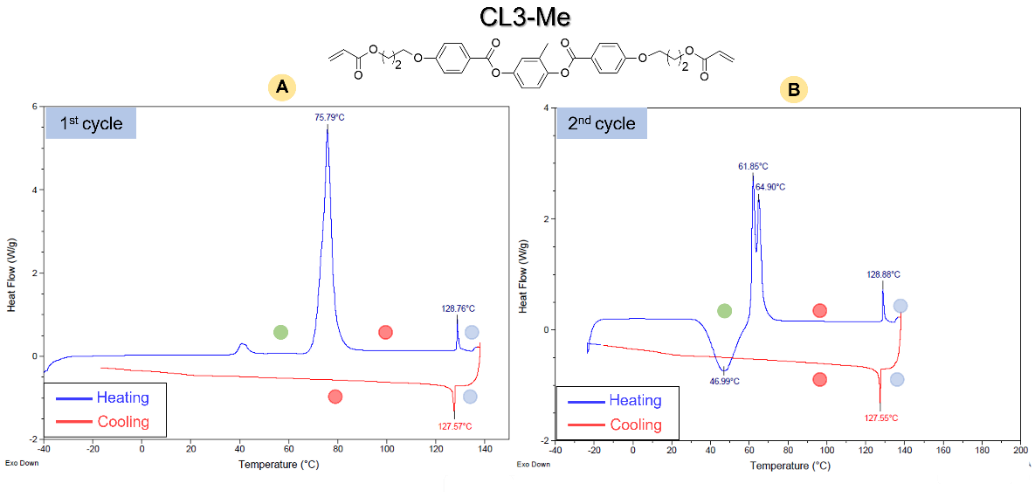

Figure A1: Mesomorphic properties of the CL3-Me. A) DSC trace related to the first heating and cooling scan (20 °C/min); B) DSC trace related to the second heating and cooling scan (20 °C/min). During the second heating cycle the exotherm peak around 47 °C is attributed to cold crystallisation from the nematic phase

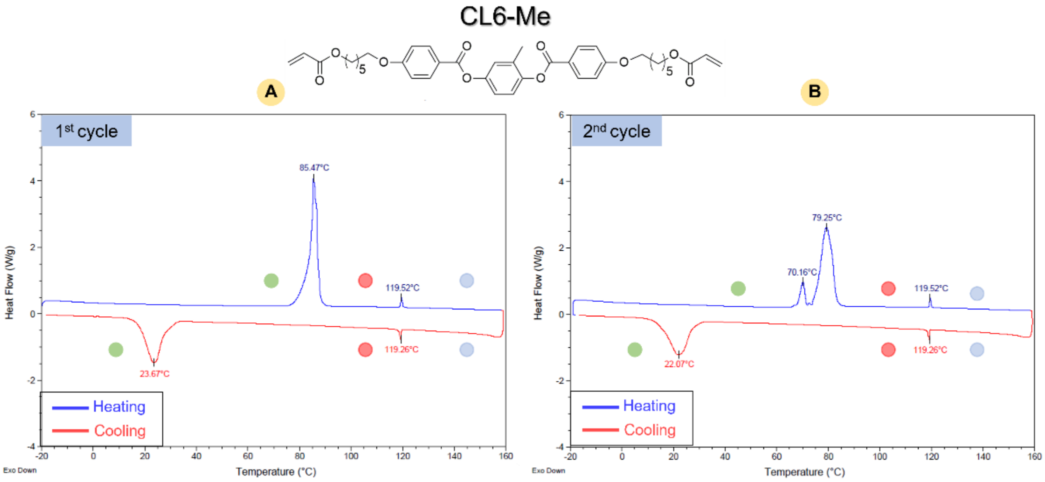

Figure A2: Mesomorphic properties of the CL6-Me. A) DSC trace related to the first heating and cooling scan (20 °C/min); B) DSC trace related to the second heating and cooling scan (20 °C/min).

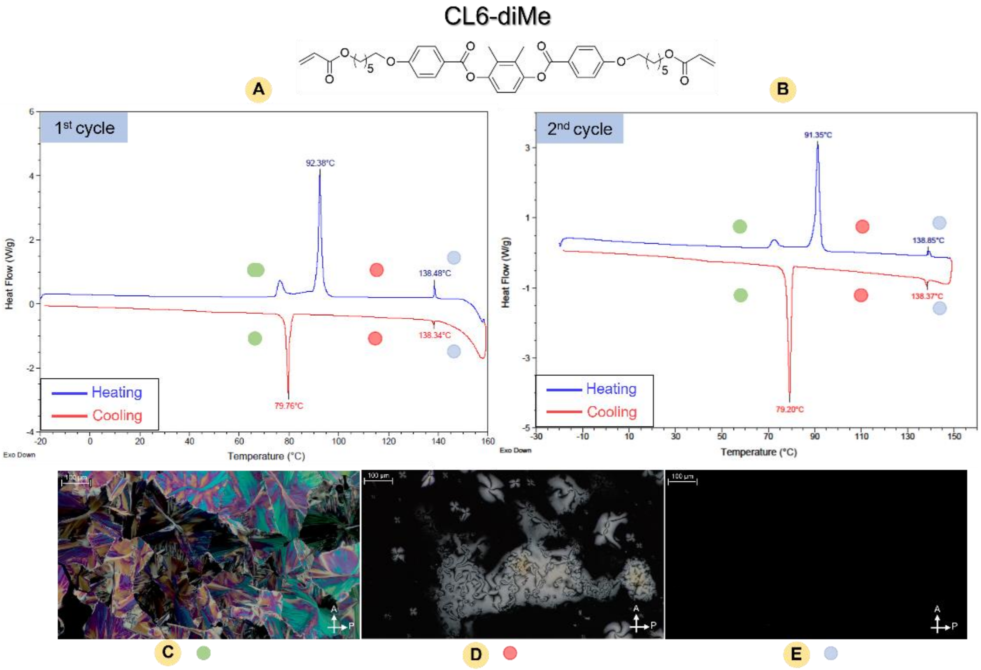

Figure A3: Mesomorphic properties of the CL6-diMe. A) DSC trace related to the second heating and cooling scan (20 °C/min); B) POM image of the crystal phase at 50 °C on cooling; C) POM image of nematic phase at 110 °C on cooling; D) POM image of the isotropic phase at 120°C on cooling.

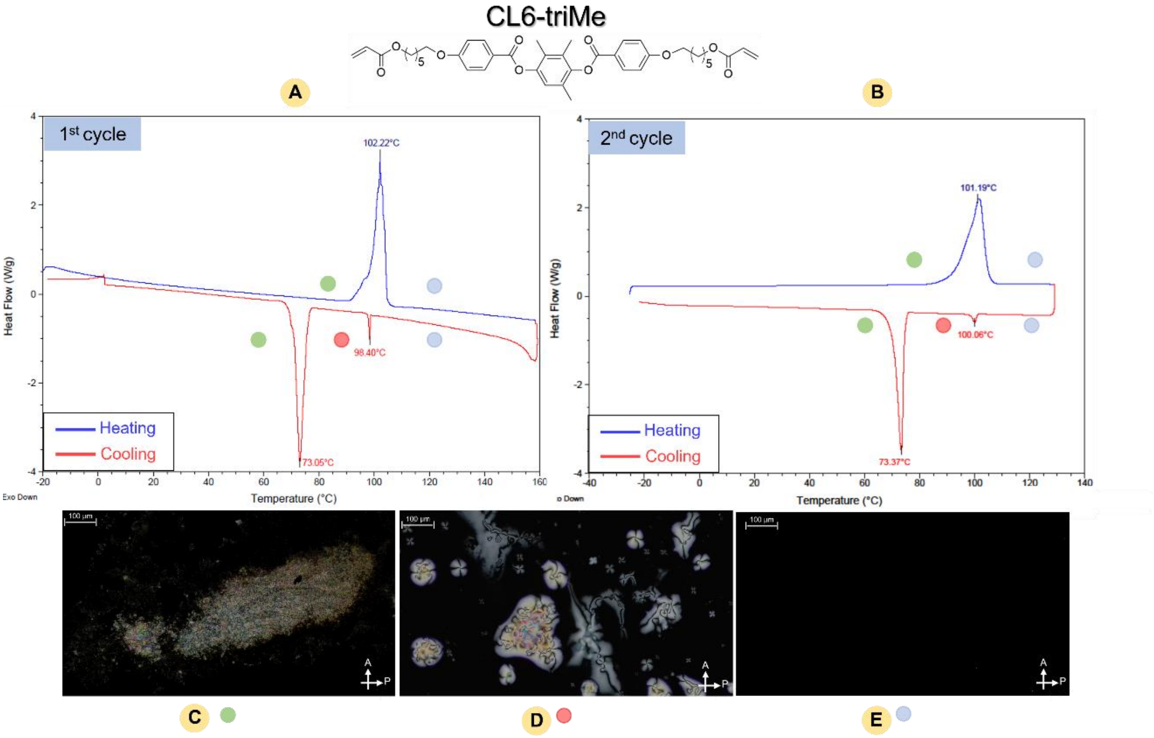

Figure A4: Mesomorphic properties of the CL6-triMe.A) DSC trace related to the second heating and cooling scan (20 °C/min); B) POM image of the crystal phase at 50 °C on cooling; C) POM image of nematic phase at 80 °C on cooling; D) POM image of the isotropic phase at 97°C on cooling.

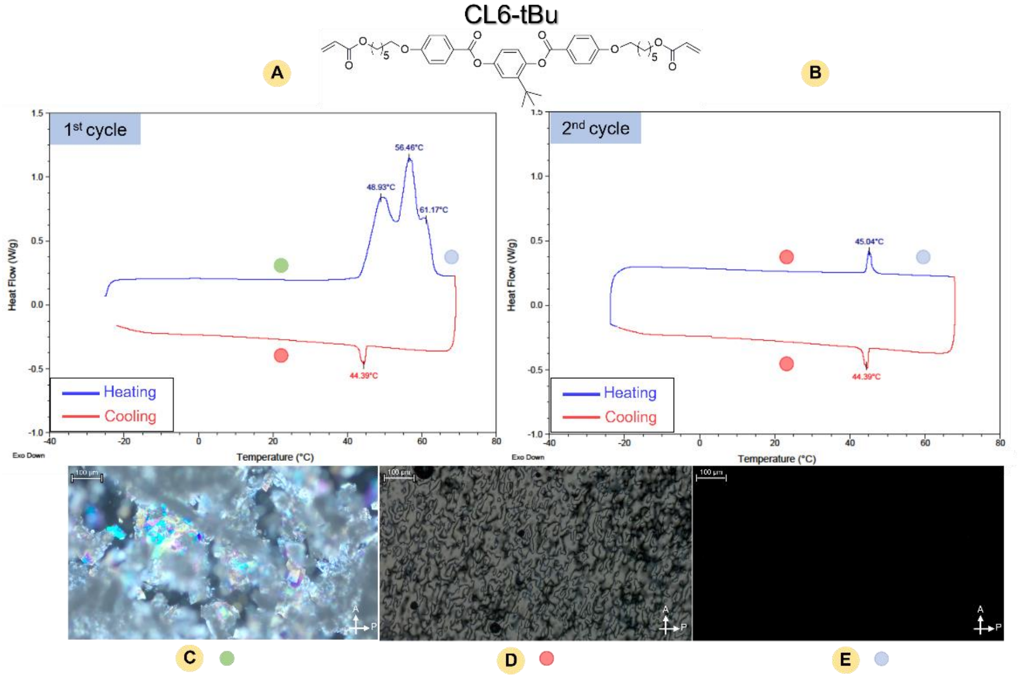

Figure A5: Mesomorphic properties of the CL6-tBu. A) DSC trace related to the first heating and cooling scan (20 °C/min); B) DSC trace related to the second heating and cooling scan (20 °C/min); C) POM image of the crystal phase at 35 °C on cooling; D) POM image of nematic phase at 40 °C on cooling; D) POM image of the isotropic phase at 65 °C on cooling.

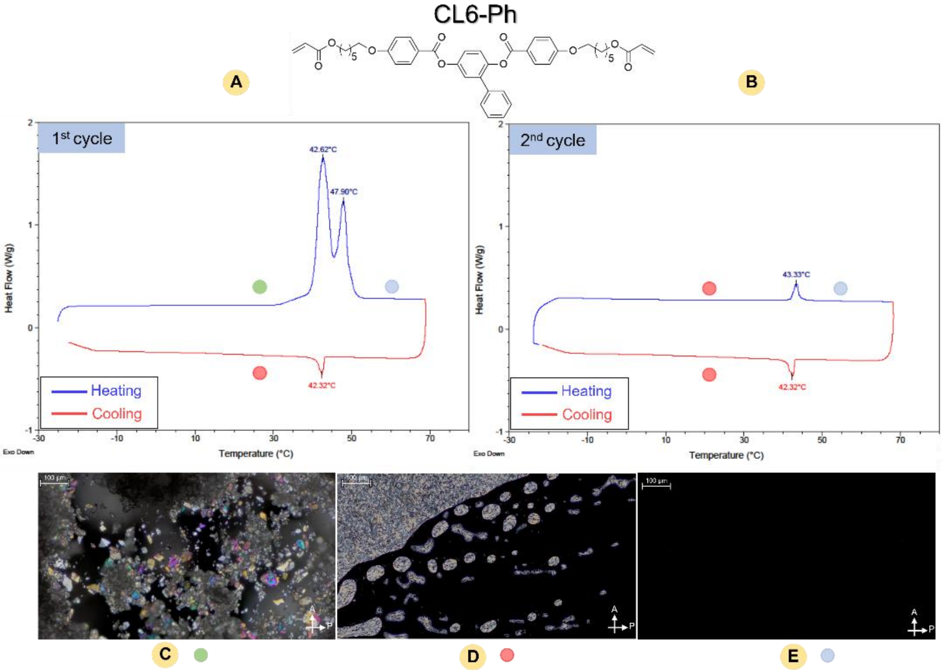

Figure A6: Mesomorphic properties of the CL6-Ph. A) DSC trace related to the first heating and cooling scan (20 °C/min); B) DSC trace related to the second heating and cooling scan (20 °C/min); C) POM image of the crystal phase at 35°C on cooling; D) POM image of nematic phase at 30 °C on cooling; D) POM image of the isotropic phase at 55 °C on cooling.

Mesomorphic properties of monomer mixtures

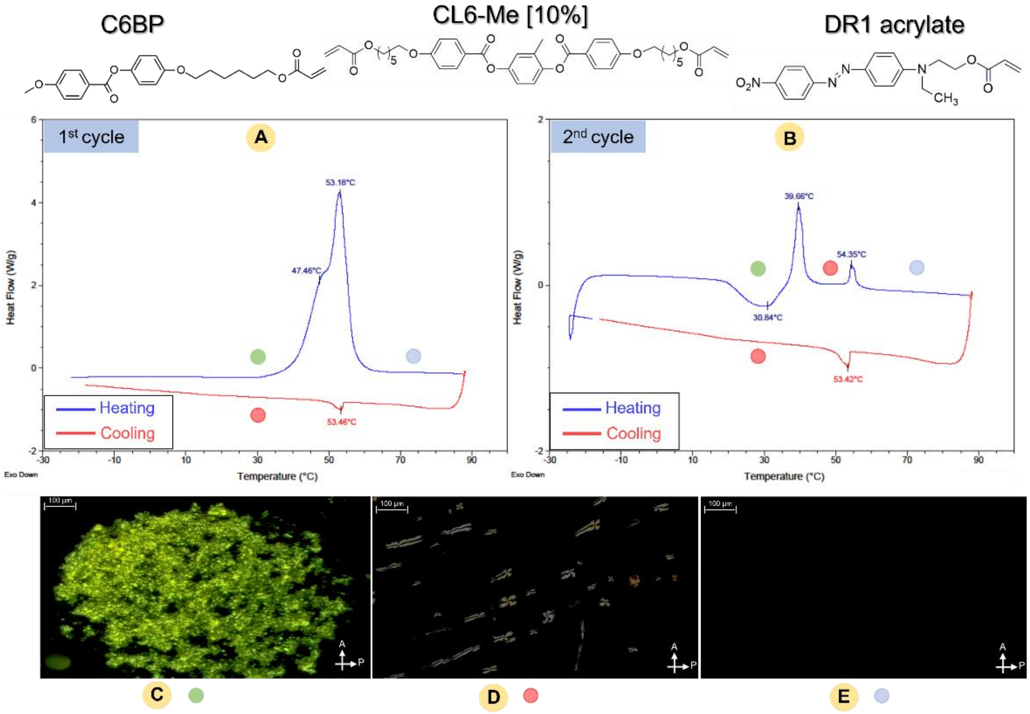

Figure A7: Mesomorphic properties of the mixture containing CL6-Me [10%]. A) DSC trace related to the first heating and cooling scan (20 °C/min); B) DSC trace related to the second heating and cooling scan (20 °C/min). During the second heating cycle the exotherm peak around 30 °C is attributed to cold crystallisation from the nematic phase; C) POM image of the crystal phase at 45 °C on cooling; D) POM image of nematic phase at 45 °C on cooling; D) POM image of the isotropic phase at 65 °C on cooling.

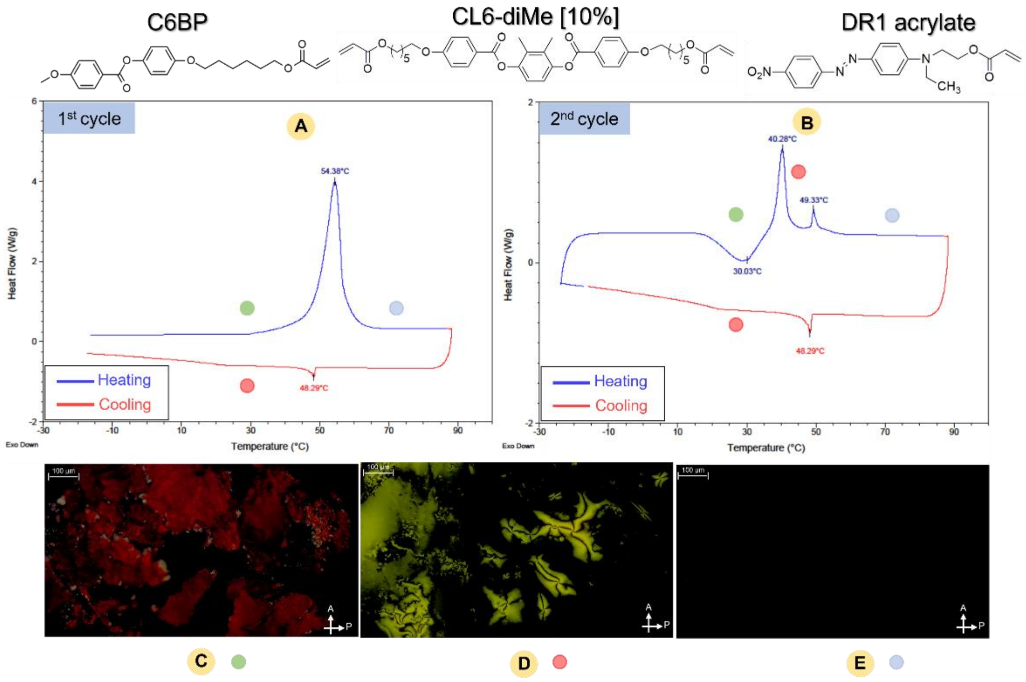

Figure A8: Mesomorphic properties of the mixture containing CL6-diMe [10%]. A) DSC trace related to the first heating and cooling scan (20 °C/min); B) DSC trace related to the second heating and cooling scan (20 °C/min). During the second heating cycle the exotherm peak around 30 °C is attributed to cold crystallisation from the nematic phase; C) POM image of the crystal phase at 40 °C on cooling; D) POM image of nematic phase at 45 °C on cooling; D) POM image of the isotropic phase at 65 °C on cooling.

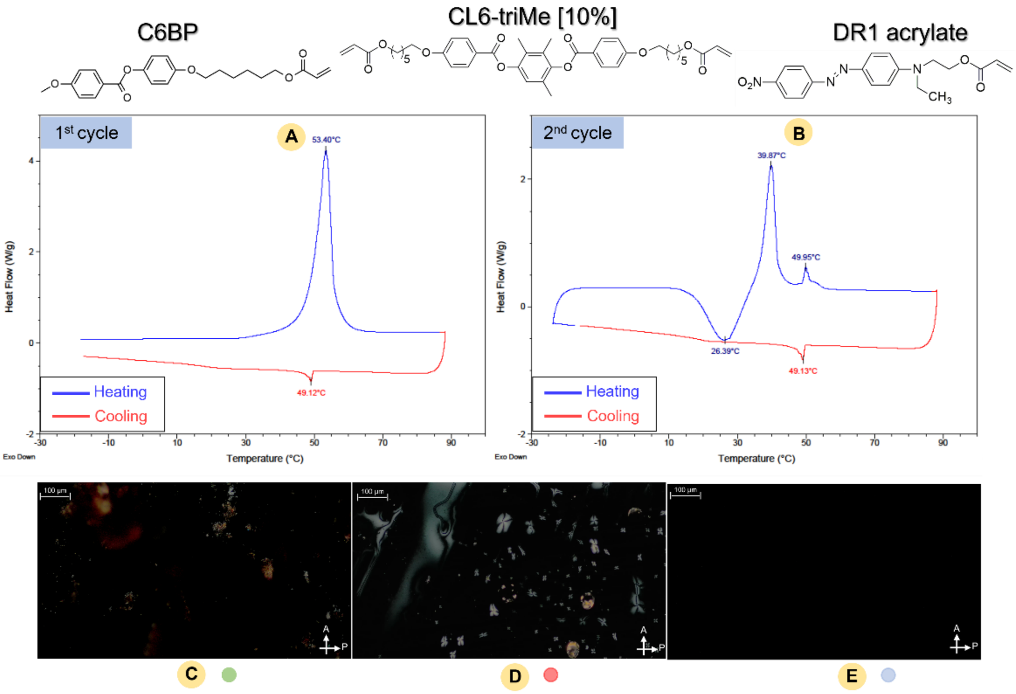

Figure A9: Mesomorphic properties of the mixture containing CL6-triMe [10%]. A) DSC trace related to the first heating and cooling scan (20 °C/min); B) DSC trace related to the second heating and cooling scan (20 °C/min). During the second heating cycle the exotherm peak around 26 °C is attributed to cold crystallisation from the nematic phase; C) POM image of the crystal phase at 35 °C on cooling; D) POM image of nematic phase at 45 °C on cooling; D) POM image of the isotropic phase at 60 °C on cooling.

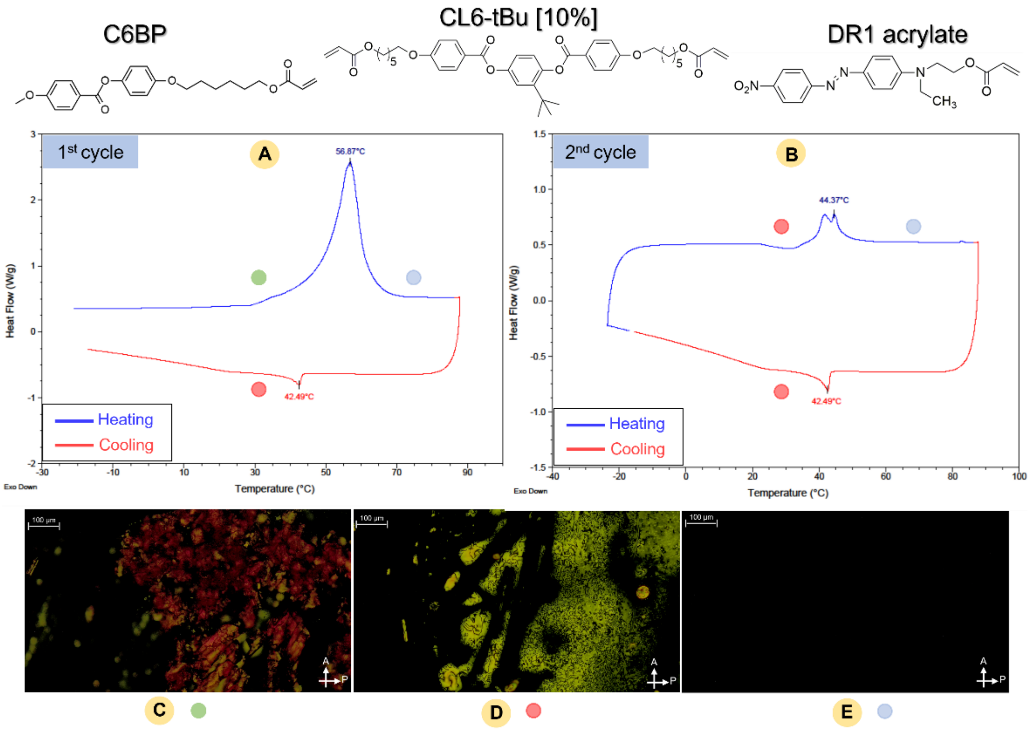

Figure A10: Mesomorphic properties of the mixtures containing CL6-tBu [10%]. A) DSC trace related to the first heating and cooling scan (20 °C/min); B) DSC trace related to the second heating and cooling scan (20 °C/min); C) POM image of the crystal phase at 45 °C on cooling; D) POM image of nematic phase at 35 °C on cooling; D) POM image of the isotropic phase at 60 °C on cooling.

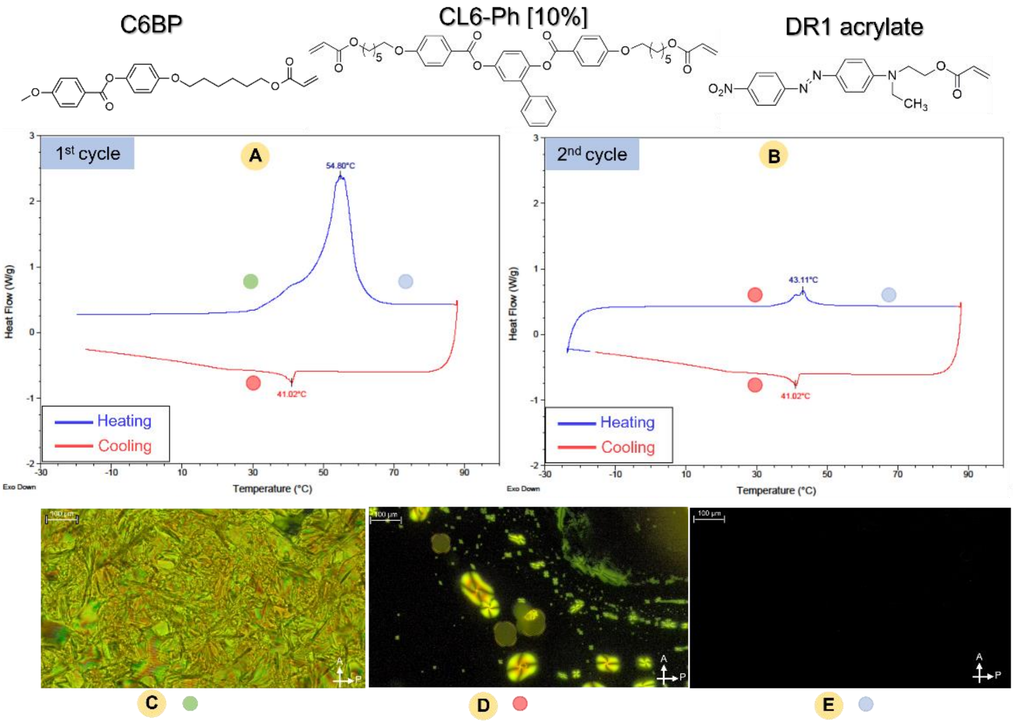

Figure A11: Mesomorphic properties of the mixture containing CL6-Ph [10%]. A) DSC trace related to the first heating and cooling scan (20 °C/min); B) DSC trace related to the second heating and cooling scan (20 °C/min); C) POM image of the crystal phase at 45°C on cooling; D) POM image of nematic phase at 30 °C on cooling; D) POM image of the isotropic phase at 60 °C on cooling.

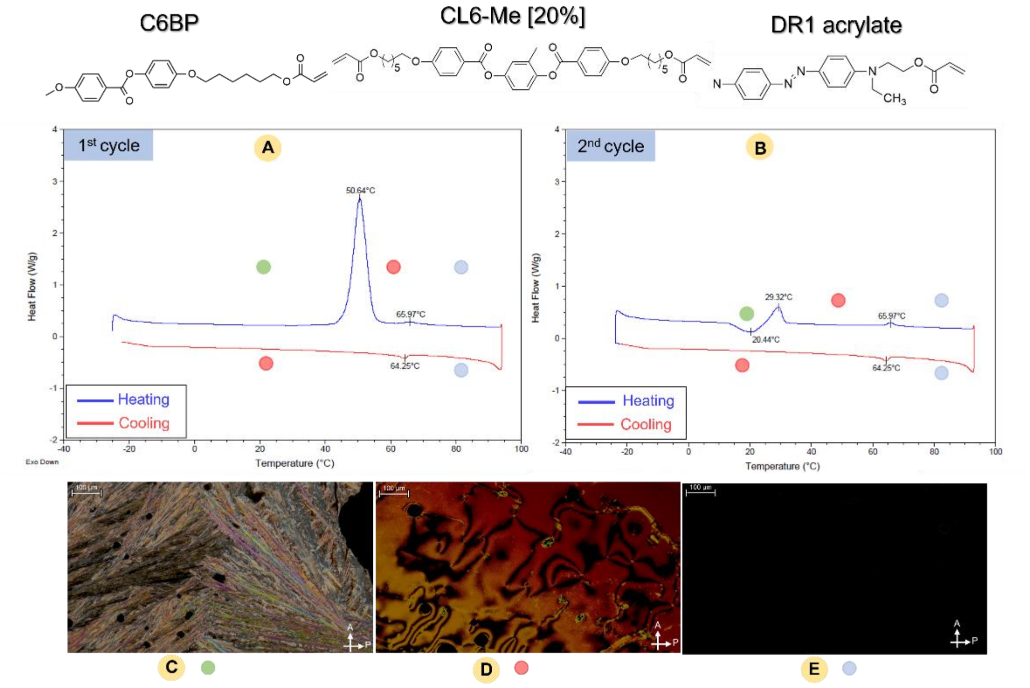

Figure A12: Mesomorphic properties of the mixture containing CL6-Me [20%]. A) DSC trace related to the first heating and cooling scan (20 °C/min); B) DSC trace related to the second heating and cooling scan (20 °C/min); C) POM image of the crystal phase at 40°C on cooling; D) POM image of nematic phase at 30 °C on cooling; D) POM image of the isotropic phase at 67 °C on cooling.

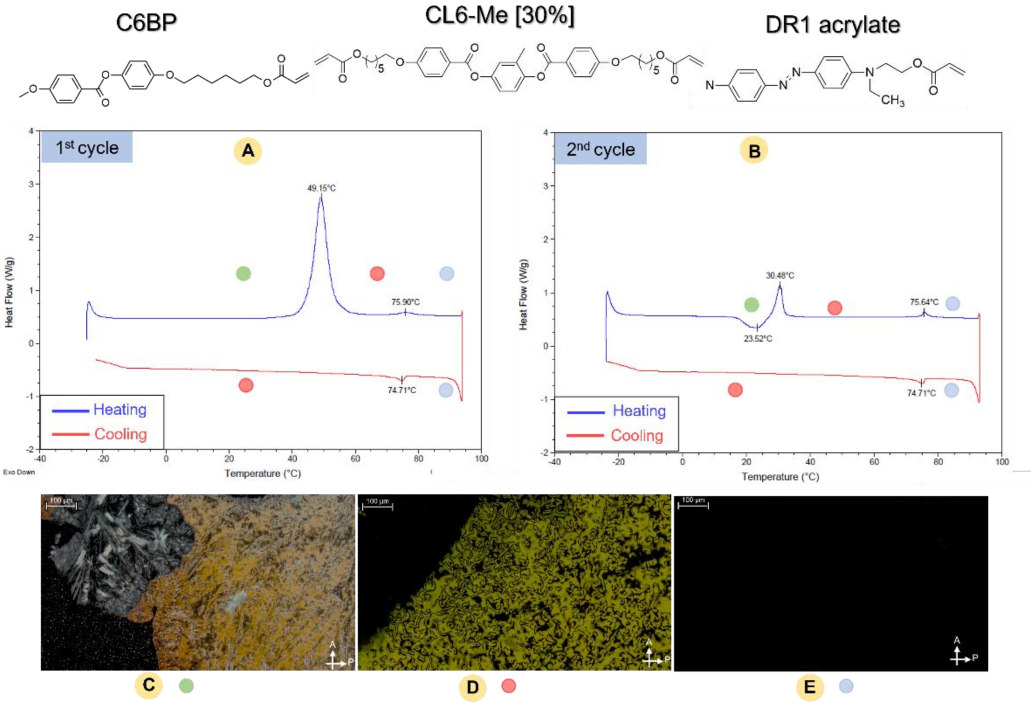

Figure A13: Mesomorphic properties of the mixture containing CL6-Me [30%]. A) DSC trace related to the first heating and cooling scan (20 °C/min); B) DSC trace related to the second heating and cooling scan (20 °C/min); C) POM image of the crystal phase at 40°C on cooling; D) POM image of nematic phase at 30 °C on cooling; D) POM image of the isotropic phase at 80 °C on cooling.

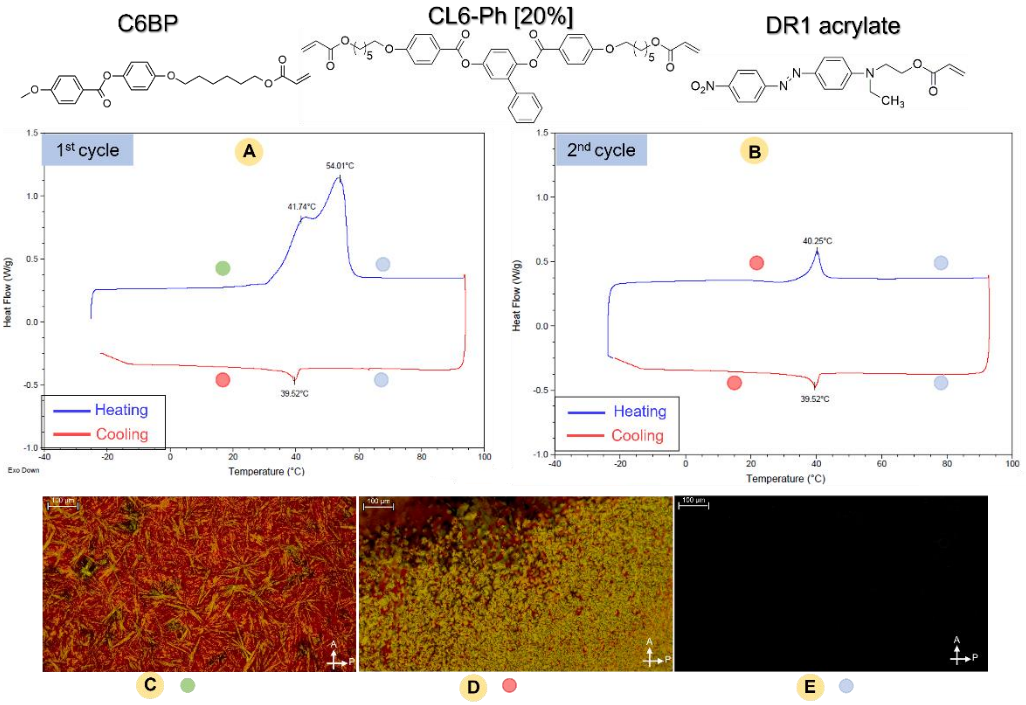

Figure A14: Mesomorphic properties of the mixture containing CL6-Ph [20%]. A) DSC trace related to the first heating and cooling scan (20 °C/min); B) DSC trace related to the second heating and cooling scan (20 °C/min); C) POM image of the crystal phase at 35°C on cooling; D) POM image of nematic phase at 30 °C on cooling; D) POM image of the isotropic phase at 60 °C on cooling.

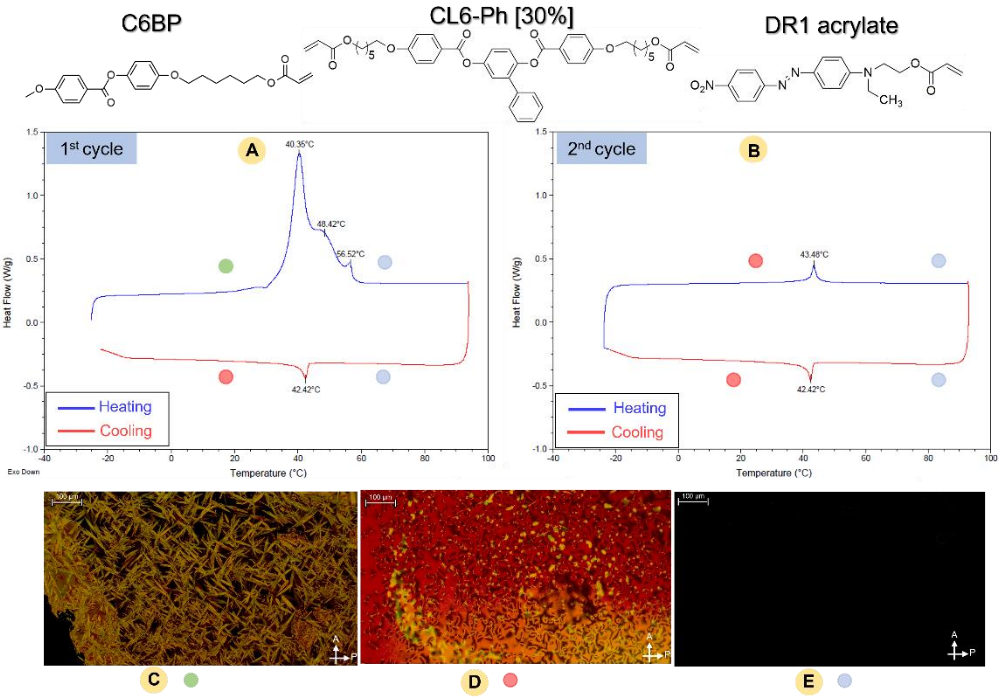

Figure A15: Mesomorphic properties of the mixture containing CL6-Ph [30%]. A) DSC trace related to the first heating and cooling scan (20 °C/min); B) DSC trace related to the second heating and cooling scan (20 °C/min); C) POM image of the crystal phase at 35°C on cooling; D) POM image of nematic phase at 30 °C on cooling; D) POM image of the isotropic phase at 60 °C on cooling.

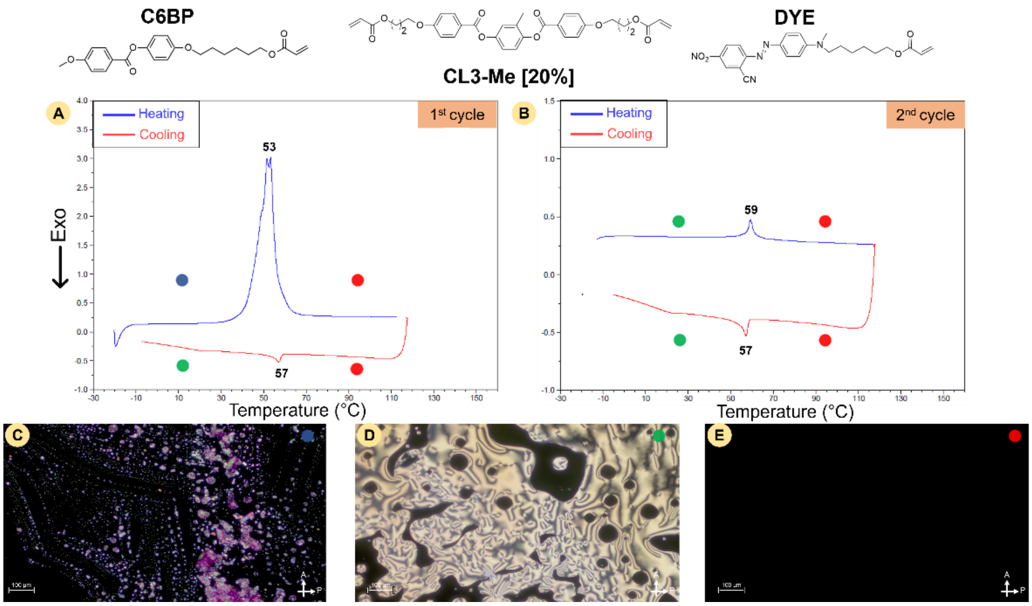

Figure A16: Mesomorphic properties of the monomer mixture LCN3-Me [20%]. A) DSC trace related to the first heating and cooling cycle (20 °C min^{-1}); B) DSC trace related to the second heating and cooling cycle (20 °C min^{-1}). C) POM image of the crystal phase at 21 °C on heating; D) POM image of nematic phase at 45 °C on cooling; E) POM image of the isotropic phase at 70 °C on cooling.

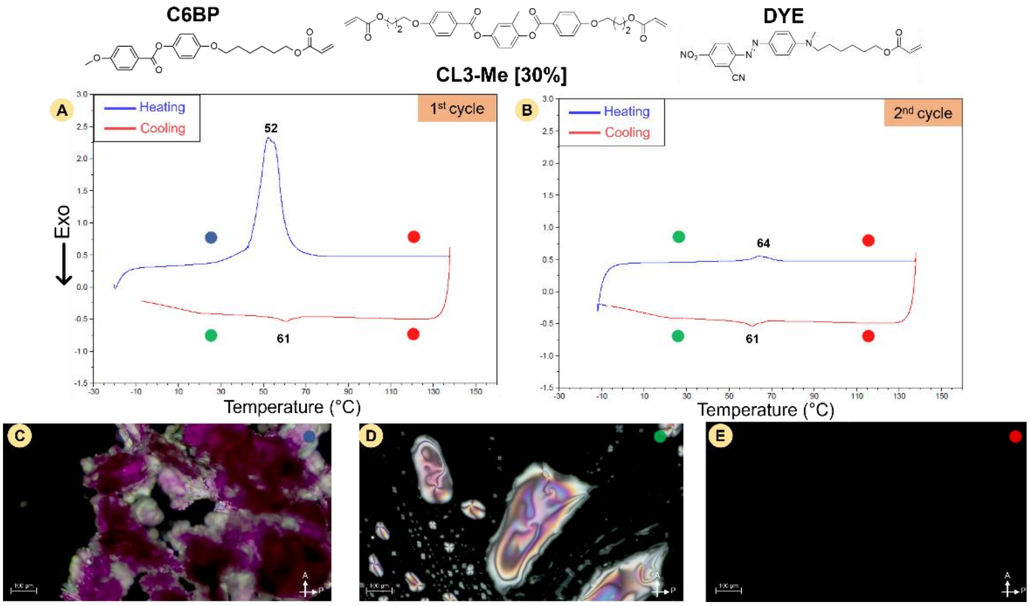

Figure A17: Mesomorphic properties of the monomer mixture LCN3-Me [30%]. A) DSC trace related to the first heating and cooling cycle (20 °C min^{-1}); B) DSC trace related to the second heating and cooling cycle (20 °C min^{-1}). C) POM image of the crystal phase at 21 °C on heating; D) POM image of nematic phase at 45 °C on cooling; E) POM image of the isotropic phase at 70 °C on cooling.

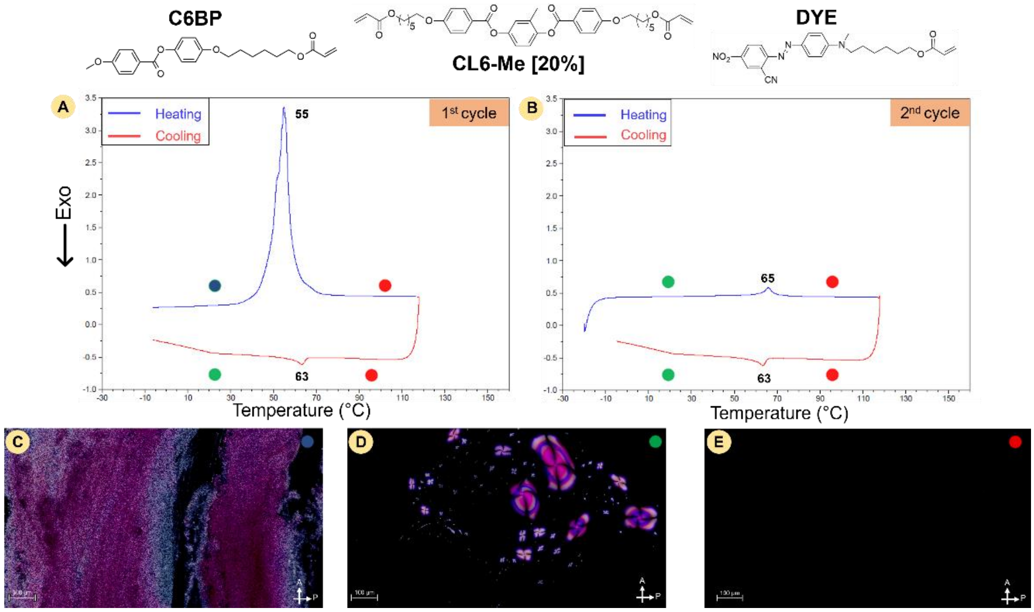

Figure A18: Mesomorphic properties of the LCN6-Me [20%]. A) DSC trace related to the first heating and cooling cycle (20 °C min^{-1}); B) DSC trace related to the second heating and cooling cycle (20 °C min^{-1}). C) POM image of the crystal phase at 30 °C on heating; D) POM image of nematic phase at 70 °C on cooling; E) POM image of the isotropic phase at 45°C on cooling.

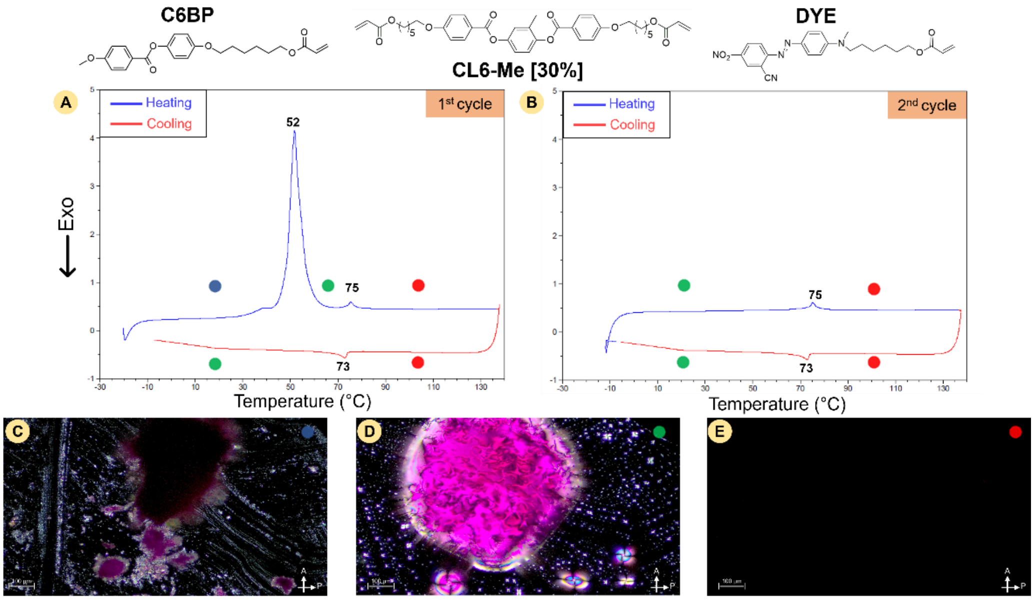

Figure A19: Mesomorphic properties of the LCN6-Me [30%]. A) DSC trace related to the first heating and cooling cycle (20 °C min^{-1}); B) DSC trace related to the second heating and cooling cycle (20 °C min^{-1}). C) POM image of the crystal phase at 30 °C on heating; D) POM image of nematic phase at 60 °C on cooling; E) POM image of the isotropic phase at 80°C on cooling.

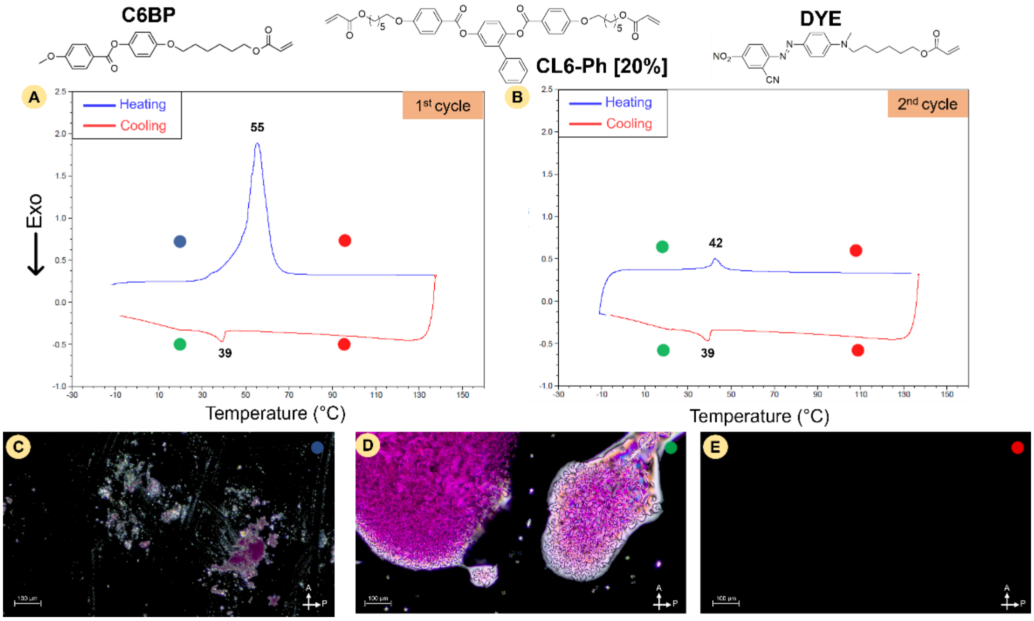

Figure A20: Mesomorphic properties of the LCN6-Ph [20%]. A) DSC trace related to the first heating and cooling cycle (20 °C min^{-1}); B) DSC trace related to the second heating and cooling cycle (20 °C min^{-1}). C) POM image of the crystal phase at 35 °C on heating; D) POM image of nematic phase at 30 °C on cooling; E) POM image of the isotropic phase at 65°C on cooling.

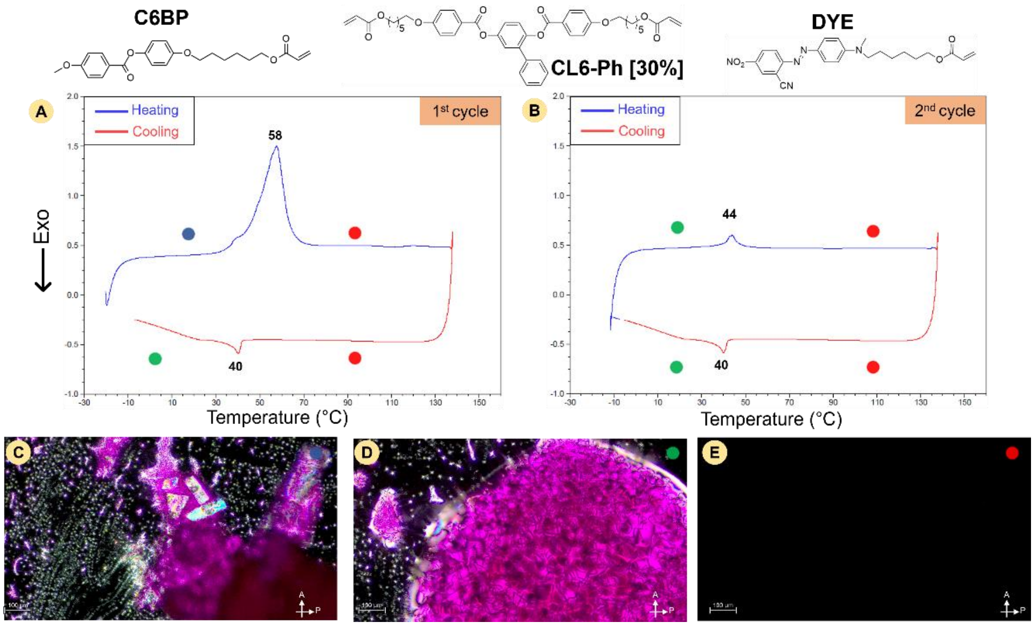

Figure A21: Mesomorphic properties of the LCN6-Ph [30%]. A) DSC trace related to the first heating and cooling cycle (20 °C min^{-1}); B) DSC trace related to the second heating and cooling cycle (20 °C min^{-1}). C) POM image of the crystal phase at 20°C on heating; D) POM image of nematic phase at 31°C on cooling; E) POM image of the isotropic phase at 60°C on cooling.

References

[1] T. Takagi, *J. Intell. Mater. Syst. Struct.* **1990,** *1 (2)*, 149–156.

[2] S.W. Ula, N.A. Traugutt, R. Volpe, R.R. Patel, K. Yu, C. Yakacki, *Liq. Cryst. Rev.*, **2018**,*6*, 107–78.

[3] Jeu, W.H., *Liquid crystal elastomers: materials and applications,* Springer, Berlin,**2012**.

[4] F. Ilievski, A.D. Mazzeo, R.F. Shepherd, X. Chen, G.M. Whitesides, *Angew. Chem. Int. Ed.*,**2011**, *50 (8)*, 1890–1895.

[5] P.G. De Gennes, *C. R. Acad. Sci. Paris*,**1975,** Ser. B, 281, 101–103.

[6] H. Wermter, H. Finkelmann, *E-Polym.*, **2001**,*1 (1)*.

[7] J.W. Goodby, *Handbook of Liquid Crystals*, ISBN 9783527671403 Wiley-VCH Verlag GmbH & Co. KGaA, Weinheim, Germany, **2014**.

[8] F.C. Frank, *Discuss. Faraday Soc.*, **1958**,*25*, 19.

[9] D.Demus, *Mol. Cryst. Liq. Cryst. Inc. Nonlinear Opt.*, **1988**,*165 (1)*, 45–84.

[10] M.J. Stephen, J.P. Straley, *Rev. Mod. Phys.*, **1974**,*46 (4)*, 617–704.

[11] D. Andrienko, *J. Mol. Liq.*, **2018**,*267*, 520–541.

[12] P.S. Pershan, *Phys. Today*, **1982**,*35 (5)*, 34–39.

[13] E.I. Kovshev, L.M., Blinov, V.V Titov, *Russ. Chem. Rev.*,**1987**, *46 (5)*, 395–419.

[14] G. Vertogen, W.H. De Jeu, *Thermotropic Liquid Crystals*, *Fundamentals*, Springer Berlin Heidelberg, Berlin, Heidelberg, **1988**.

[15] A.Ramamoorthy, *Thermotropic liquid crystals: recent advances*, Springer, Dordrecht, **2007**.

[16] T. Wöhrle, I. Wurzbach, J. Kirres, A. Kostidou, N. Kapernaum, J. Litterscheidt, J.C. Haenle, P. Staffeld, A. Baro, F. Giesselmann, S. Laschat, *Chem. Rev.*, **2016**, *116 (3)*, 1139–1241.

[17] G. Pelzl, S. Diele, W. Weissflog, *Adv. Mater.*, **1999**, ***11*** *(9)*, 707–724.

[18] S. Kumar, *Isr. J. Chem.*, **2012**,***52*** *(10)*, 820–829.

[19] H. Takezoe, Y. Takanishi, *Jpn. J. Appl. Phys.* **2006**, ***45*** *(2A)*, 597–625.

[20] H.K. Bisoyi, Q. Li, *Chem. Rev.* **2022**, *122 (5)*, 4887–4926.

[21] R. Williams, *J. Chem. Phys.* **1963**, ***39*** *(2)*, 384–388.

[22] T.C. Lubensky, *Phys. Rev. A*, **1970**, ***2*** *(6)*, 2497–2514.

[23] G. Solladié, R.G. Zimmermann, *Angew. Chem. Int. Ed. Engl.*, **1984**, *23 (5)*, 348–362.

[24] Dierking, *Textures of liquid crystals*, Wiley-VCH, Weinheim,**2003**.

[25] Dierking, *Symmetry*, **2014**, ***6** (2)*, 444–472.

[26] M. Warner, E.M. Terentjev, *Liquid crystal elastomers*, Oxford University Press, Oxford, **2003**.

[27] D. Broer, G.P. Crawford, S. Zumer, S. CRC Press, **2011**.

[28] P.G. De Gennes, *C. R. Acad. Sci. Paris, Ser.* II b, **1997,** 324, 343–348.

[29] C. Mauguin, *C. R. Acad. Sci*., Paris, **1911**, 156, 1246.

[30] Y. B. Kim, H. S. Kim, J. S. Choi, M.Matuszcyk, H. Olin, M. Buivydas, P.Rudquist, *Mol. Cryst. Liq. Cryst*., **1995**,262, 89.

[31] H. Yokoyama, *Mol. Cryst. Liq. Cryst. Inc. Nonlinear Opt.*, **1988**,*165 (1)*, 265–316.

[32] D.W. Berreman, *Mol. Cryst. Liq. Cryst.*, **1973**, *23 (3–4)*, 215–231.

[33] E.F. Luk'yanchenko, V.A., Kozunov, V.I. Grigos, V.I. *Russ. Chem. Rev.*, **1985**, *54 (2)*, 129–143.

[34] B. Lee, N.A. Clark, *Science*, **2001**, ***291** (5513)*, 2576–2580.

[35] K. Ichimura, Y. Suzuki, T. Seki, A. Hosoki, K. Aoki, *Langmuir*, **1988**, *4 (5)*, 1214–1216.

[36] W. Helfrich, *Mol. Cryst. Liq. Cryst.*, **1973**, *21 (3–4)*, 187–209.

[37] M.I. Boamfa, S.V. Lazarenko, E.C.M. Vermolen, A. Kirilyuk, T. Rasing, Adv. *Mater.*, **2005**, *17 (5)*, 610–614.

[38] J. Son, W. Zin, H. Takezoe, J. Song, *Adv. Mater.*,**2012**, *24 (45)*, 6105–6110.

[39] L.T. Creagh, A.R. Kmetz, *Mol. Cryst. Liq. Cryst.*, **1973**,*24 (1–2)*, 59–68.

[40] P.G. De Gennes, *Phys. Lett. A*, **1969**, *28 (11)*, 725–726.

[41] P. G. De Gennes, "No Title," Comptes Rendus l'Académie des Sci.,**1975,** vol. B, no. 281, p. 101.

[42] F. Brömmel, D. Kramer, H. Finkelmann, *Preparation of Liquid Crystalline Elastomers*, Springer edition, **2012**.

[43] B. Reck, H. Ringsdorf, *Makromol. Chem. Rapid Commun.*, **1986**, *7 (6)*, 389–396.

[44] J. Küpfer, H.Finkelmann, *Makromol. Chem. Rapid Commun.*, **1991**, *12*, 717–726.

[45] B. Donnio, H., Wermter, H. Finkelmann, *Macromolecules*, **2000**, *33 (21)*, 7724–7729.

[46] H.Zhao, J.J. Wie, D. Copic, C.R. Oliver, C.R., A.White, S. Kim, A.J. Hart, *ACS Appl. Mater. Interfaces*, **2016**, *8 (12)*, 8110–8117.

[47] H. Zeng, M. Martella, P. Wasylczyk, G.Cerretti, J.-C.G. Lavocat, C.H. Ho, C. Parmeggiani, D.S. Wiersma, *Adv. Mater.*, **2014**,*26 (15)*, 2319–2322.

[48] T. Ikeda, J. Mamiya, Y. Yu, *Angew. Chem. Int. Ed.*,**2007**, *46 (4)*, 506–528.

[49] L.Yang, K. Setyowati, A. Li, S. Gong, J. e Chen, *Adv. Mater.*,**2008**, *20 (12)*, 2271–2275.

[50] M. Chambers, H. Finkelmann, M. Remškar, A. Sánchez-Ferrer, B. Zalar, S. Žumer, *J Mater Chem*,**2009**, *19 (11)*, 1524–1531.

[51] T. Ikeda, *J. Mater. Chem.*, **2003**, *13 (9)*, 2037.

[52] E.Wagner-Wysiecka, N. Łukasik, J.F. Biernat, E. Luboch, *J. Incl. Phenom. Macrocycl. Chem.*, **2018**, *90 (3–4)*, 189–257.

[53] P. Weis, S. Wu, *Macromol. Rapid Commun.*, **2018**,*39 (1)*, 1700220.

[54] A.A. Beharry, G.A. Woolley, *Chem. Soc. Rev.*, **2011**, *40 (8)*, 4422.

[55] P.M. Hogan, A.R. Tajbakhsh, E.M. Terentjev, *Phys. Rev. E*, **2002**, *65 (4)*, 041720.

[56] M. Li, P. Keller, B. Li, X. Wang, M. Brunet, *Adv. Mater.*, **2003**, *15 (7–8)*, 569–572.

[57] M. Camacho-López, H. Finkelmann, P. Palffy-Muhoray, M. Shelley, *Nat. Mater.*,**2004**, *3*, 307–310.

[58] C.L.M. Harvey, E.M. Terentjev, *Eur. Phys. J. E*, **2007**, *23 (2)*, 185–189.

[59] H. Finkelmann, E. Nishikawa, G.G. Pereira, M.A. Warner, *Phys. Rev. Lett.*, **2001**, *87*, 015501.

[60] M. Pilz Da Cunha, E.A.J. Van Thoor, M.G. Debije, D.J. Broer, A.P.H.J. Schenning, *J. Mater. Chem. C*, **2019,***7 (43)*, 13502–13509.

[61] D. Vorlander, Z. Pkys. Ckem. **1923**,105,211

[62] M.A. Osman, *Z. Für Naturforschung A*, **1983**, *38 (6)*, 693–697.

[63] D. Kashyap, S. Patel, V. Prajapat, V. Sharma, D. Vasava, *Mol. Cryst. Liq. Cryst.*, **2019**, *681 (1)*, 58–70.

[64] T.H. Aldahri, M. Alaasar, H.A. Ahmed,*Liq. Cryst.*, **2023**, 1–10.

[65] M.Hird, *Chem. Soc. Rev.*, **2007**, *36 (12)*, 2070.

[66] M. Hird, K.J. Toyne, *Mol. Cryst. Liq. Cryst. Sci. Technol. Sect. Mol. Cryst. Liq. Cryst.*, **323** (1), 1–67.ù

[67] D. Liu, D. Broer, *Langmuir*. **2014**, *30*, 13499.

[68] J. Lub, D. J. Broer, R. T. Wegh, E. Peeters, B. M. I. Van der Zande, *Mol. Cryst. Liquid Cryst.* **2005**, *429*, 77.

[69] T. H. Ware, J. S. Biggins, A. F. Shick, M. Warner, T. J. White, *Nat. Commun.* **2016**,*7*, 10781.

[70] C. M. Yakacki, M. Saed, D. P. Nair, T. Gong, S. M. Reed, C. N. Bowman, *RSC Adv.* **2015**, *5,* 18997.

[71] C. Ohm, M. Brehmer, R. Zentel, *Adv. Mater*. **2010**, *22*, 3366.

[72] D. L. Thomsen, P. Keller, J. Naciri, R. Pink, H. Jeon, D. Shenoy, B. R. Ratna, *Macromol.* **2001**, *34*, 5868.

[73] M. Barnes, S. M. Sajadi, S. Parekh, M. M. Rahman, P. M. Ajayan, R. Verduzco, *ACS Appl. Mater. Interfaces.* **2020**, *12*, 28692.

[74] S. Nocentini, D. Martella, C. Parmeggiani, D. S. Wiersma, *Materials* **2016**, *9,* 525.

[75] D. Martella, D. Antonioli, S. Nocentini, D. S. Wiersma, G. Galli, M. Laus, C. Parmeggiani, *RSC Adv.* **2017**, *7*,19940.

[76] H. F. Lu, M. Wang, X. M. Chen, B. P. Lin, H. Yang, *J. Am. Chem. Soc.* **2019,** *141*,14364.

[77] T. Ube, K. Takado, T. Ikeda, *J. Mater. Chem.* **2015**, *C3*, 8006.

[78] T.S. Hebner, C.N. Bowman, T.J. White, *Polym. Chem.* **2021**, *12*,1759.

[79] G. E. Bauman, J. M. McCracken, T. J. White, *Angew. Chem. Int. Ed.* **2022**,*61*,1433.

[80] F. Lupi, D. Martella, S. Nocentini, D. Antonioli, M. Laus, D. S. Wiersma, C. Parmeggiani, *ACS Appl. Polym. Mater*. **2021**,*3*,1602.

[81] R. K. Shaha, A. H. Torbati, C. P. Frick, *J. Appl. Polym. Sci*. **2021**, *138*,50136.

[82] M. Barnes, S. Cetinkaya, A. Ajnsztajn, R. Verduzco. *Soft Matter*. **2022**,*18*,5074.

[83] M. Bispo, D. Guillon, B. Donnio, H. Finkelmann. *Macromolecules* **2008**, *41*,3098.

[84] B. Bahadur, *Mol. Cryst. Liq. Cryst.*, **1984**, *109 (1)*, 3–93.

[85] C.M. Spillmann, J. Naciri, B.D. Martin, W. Farahat, H. Herr, B.R. Ratna, *Sens. Actuators Phys.*, **2007**, *133 (2)*, 500–505.

[86] M.Yamada, M. Kondo, J. Mamiya, Y. Yu, M. Kinoshita, C. Barrett, T. Ikeda, *Angew. Chem.*, **2008**, *47 (27)*, 4986–8.

[87] M. Yamada, M. Kondo, R. Miyasato, Y. Naka, J. Mamiya, M. Kinoshita, A. Shishido, Y. Yu, C. Barrett, T. Ikeda, *J. Mater. Chem.*, **2009**, *19*, 60–62.

[88] A. Sánchez-Ferrer, T. Fischl, M. Stubenrauch, A. Albrecht, H. Wurmus, M. Hoffmann, H. Finkelmann, *Adv. Mater.*, **2011**, *23 (39)*, 4526–4530.

[89] C.V. Oosten, C. van, Bastiaansen, D.J. Broer, *Nat. Mater.*, **2009**, *8 8*, 677–82.

[90] M. Rojas-Rodríguez, T. Fiaschi, M. Mannelli, L. Mortati, F. Celegato, D.S.Wiersma, C. Parmeggiani, D. Martella, *ACS Appl. Mater. Interfaces*, **2023**, acsami.2c22892.

[91] R. Wei, L. Zhou, Y. He, X. Wang, P. Keller, *Polymer*, **2013**, *54 (20)*, 5321–5329.

[92] N. Satsangi,H.R. Rawls, B.K. Norling, *J. Biomed. Mater. Res.* **2004,** *71B*, 153-158.

[93] J.Kloos,J. Lub,M. Houben, Z. Born eman, K. Nijmeijer, A.P.H.J. Schenning, *Liq. Cryst.* **2022** ,*0*, 1–9.

[94] D. Martella, S. Nocentini, D. Antonioli, M. Laus, D. S. Wiersma, C. Parmeggiani. *Polymers* **2019**, *11*, 1644.

[95] C. J. McAdam, J. Simpson, *Acta Crystall.* **2008**, *64*, 627.

[96] P. Kiefer, V. Hahn, M. Nardi, L. Yang, E. Blasco, C. Barner-Kowollik, M. Wegener, *Adv. Opt. Mater.* **2020,** *8*, 2000895.

[97] J. del Barrio, C. Sánchez-Somolinos, *Adv. Opt. Mater.* **2019,** *7*, 1900598.

[98] G. Savarese, G., P.M. Becher, L.H. Lund, P. Seferovic, G.M.C. Rosano, A.J.S. Coats,*Cardiovasc. Res.*, **2023**, *118 (17)*, 3272–3287.

[99] S.S.Virani, A. Alonso, E.J. Benjamin, M.S. Bittencourt, C.W. Callaway, A.P. Carson, A.M. Chamberlain, A.R. Chang, S. Cheng, F.N. Delling, L. Djousse, M.S.V. Elkind, J.F. Ferguson, M., Fornage, S.S. Khan, B.M. Kissela, K.L. Knutson, T.W. Kwan, D.T. Lackland, T.T. Lewis, J.H. Lichtman, C.T. Longenecker, M.S. Loop, P.L. Lutsey, S.S. Martin, K. Matsushita, A.E. Moran, M.E. Mussolino, A.M. Perak, W.D. Rosamond, G.A. Roth, U.K.A. Sampson, G.M. Satou, E.B. Schroeder, S.H. Shah, C.M. Shay, N.L. Spartano, A. Stokes, D.L. Tirschwell, L.B. VanWagner, C.W. Tsao,On behalf of the American Heart Association Council on Epidemiology and Prevention Statistics Committee and Stroke Statistics Subcommittee *Circulation*, **2020**, 141 (*9*).

[100] E. Braunwald Pathophysiology of heart failure. Heart disease: a textbook of cardiovascular medicine. 4th ed. Philadelphia: W.B. Saunders, **1992**.393-418.

[101] P.A. Heidenreich, B. Bozkurt, , D. Aguilar, , L.A. Allen, J.J. Byun, M.M. Colvin, A. Deswal, M.H. Drazner, S.M Dunlay, L.R. Evers, J.C. Fang, Fedson, S.E. Fonarow, G.C. Hayek, S.S. Hernandez, A.F. Khazanie, P. Kittleson, M.M. Lee, C.S. Link, M.S. Milano, C.A. Nnacheta, L.C. Sandhu, A.T. Stevenson, L.W. Vardeny, O. Vest, A.R. C.W. Yancy, *Circulation*, **2022**, 145 (18).

[102] K.S. Shah, M.M. Kittleson, J.A. Kobashigawa, *Curr. Heart Fail. Rep.*, **2019**,*16 (5)*, 150–156.

[103] J. Stehlik, J. Kobashigawa, S.A. Hunt, H. Reichenspurner, J.K. Kirklin, *Circulation*, **2018**,*137 (1)*, 71–87.

[104] M. Mehra, J. Kobashigawa, R. Starling, S. Russell, P. Uber, J. Parameshwar, P. Mohacsi, S. Augustine, K. Aaronson, M. Barr, *J. Heart Lung Transplant.*, **2006**, *25 (9)*, 1024–1042.

[105] M. Radisic, K. L. Christman, Materials science and tissue engineering: Repairing the heart. in *Mayo Clinic Proceedings* vol. 88 884–898 Elsevier Inc, 133 **2013**.

[106] D. Timms, *Med. Eng. Phys.*, **2011**, *33 (9)*, 1041–1047.

[107] R. Gianluca, S. Francesco, F. Giuseppe, *J. Geriatr. Cardiol.*,**2013**, *9 (4)*, 389–400.

[108] D.R. Higueras-Ruiz, K. Nishikawa, H. Feigenbaum, M. Shafer, *Bioinspir. Biomim.*, 2022,**17** (1), 011001.

[109] C. Greco, P. Kotak, L. Pagnotta, C. Lamuta *Int. Mater. Rev.*,**2022**, *67 (6)*, 575–619.

[110] J. Dong, M. Yang, Z. Zheng, G. Yan*Sheng Wu Yi Xue Gong Cheng Xue Za Zhi J. Biomed. Eng. Shengwu Yixue Gongchengxue Zazhi*, **2008,** *25 (6)*, 1442–1445

[111] A. Weymann, J. Foroughi, R. Vardanyan, P.P. Punjabi, B. Schmack, S. Aloko, G.M. Spinks, C.H. Wang, A. Arjomandi Rad, A. Ruhparwar, *Adv. Mater.*, **2023**, *35 (19)*, 2207390.

[112] S.M. Mirvakili, I.W. Hunter, *Adv. Mater.*, **2018**, *30 (6)*, 1704407.

[113] I.Pirozzi, A. Kight, A.K. Han, M.R. Cutkosky, S.A. Dual, *Adv. Mater.*,**2023**, 2210713.

[114] O.A. Smiseth, H. Torp, A. Opdahl, K.H. Haugaa, S. Urheim, *Eur. Heart J.*,**2016,** *37 (15)*, 1196–1207.

[115] C.F. Guimarães, L. Gasperini, A.P. Marques, R.L. Reis, *Nat. Rev. Mater.*, **2020**, *5 (5)*, 351–370.

[116] E.H. Sonnenblick, *Am. J. Physiol.-Leg. Content*, **1962**, *202 (5)*, 931–939.

[117] R. S. Kularatne, H. Kim, J. M. Boothby, T. H. Ware, *J. Polym. Sci. Pt. B-Polym. Phys.* **2017**, *55*, 395.

[118] D. Martella, S. Nocentini, C. Parmeggiani, D. S. Wiersma, *Faraday Discuss.* **2020**.

[119] C. Ferrantini, J. M. Pioner, D. Martella, R. Coppini, N. Piroddi, P. Paoli, M. Calamai, F. S. Pavone, D. S. Wiersma, C. Tesi, E. Cerbai, C. Poggesi, L. Sacconi, C. Parmeggiani, *Circ. Res.* **2019**, *124*, e44.

[120] D. Martella, P. Paoli, J.M Pioner, L. Sacconi, R. Coppini, L. Santini, M. Lulli, E. Cerbai, D.S. Wiersma, C. Poggesi, C. Ferrantini, C.,Parmeggiani, *Small*, **2017**, *13 (46)*, 1702677.

[121] G. Vitale, B. Grandinetti, S. Querceto, D. Martella, C. Tesi, C. Poggesi, E. Cerbai, D.S. Wiersma, C. Parmeggiani, C. Ferrantini, L. Sacconi, L. (*Macromol. Mater. Eng.*, **2022**, *307 (9)*, 2200187.

[122] H. Zeng, O.M. Wani, P. Wasylczyk, A. Priimagi, *Macromol. Rapid Commun.* **2018**,*39*, 1-6.

[123] D. Martella, S. Nocentini, F. Micheletti, D. S. Wiersma, C. Parmeggiani, *Soft Matter* **2019**,*15*, 1312.

[124] H. F. Lu, M. Wang, X. M. Chen, B. P. Lin, H. Yang, *J. Am. Chem. Soc.* **2019,** *141*,14364.

[125] I. De Bellis, D. Martella, C. Parmeggiani, E. Pugliese, M. Locatelli, R. Meucci, D. S. Wiersma, S. Nocentini, *J. Phys. Chem.* **2019**, *123*, 26522.

[126] T. H. Ware, J. S. Biggins, A. F. Shick, M. Warner, T. J. White, *Nat. Commun.* **2016**,*7*, 10781.

[127] R. A. M. Hikmet, D. J. Broer, *Polymer* **1991**, *32*, 1627.

[128] S. Maruo, O. Nakamura, S. Kawata, *Opt. Lett.*, **1997**, *22 (2)*, 132.

[129] C.N. LaFratta, J.T. Fourkas, T. Baldacchini, R.A. Farrer, *Angew. Chem. Int. Ed.*, **2007**, *46 (33)*, 6238–6258.

[130] G. Von Freymann, A. Ledermann, M. Thiel, I. Staude, S. Essig, K. Busch, M. Wegener, *Adv. Funct. Mater.*, **2010**, *20 (7)*, 1038–1052.

[131] J. Fischer, M. Wegener, *Laser Photonics Rev.*, **2013**,*7 (1)*, 22–44.

[132] M. Göppert-Mayer, *Ann. Phys.*, **1931**, *401 (3)*, 273–294.

[133] H.C. Ishikawa-Ankerhold, R. Ankerhold, G.P.C. Drummen, *Molecules*, **2012**, *17 (4)*, 4047–4132.

[134] A.S. Quick, H. Rothfuss, A. Welle, B. Richter, J. Fischer, M. Wegener, C. Barner-Kowollik, *Adv. Funct. Mater.*, **2014**, *24 (23)*, 3571–3580.

[135] C.S Colley, D.C. Grills, N.A. Besley, S. Jockusch, P. Matousek, A.W. Parker, M. Towrie, N.J. Turro, P.M.W. Gill, M.W. *J. Am. Chem. Soc.*, **2002**, *124 (50)*, 14952–14958.

[136] S. Jockusch, S., Koptyug, P.F. McGarry, G.W. Sluggett, N.J. Turro, D.M. Watkins, *J. Am. Chem. Soc.*, **1997**, *119 (47)*, 11495–11501.

[137] X. Kuang, D.J. Roach, J. Wu, C.M. Hamel, Z. Ding, T.Wang, M.L. Dunn, H.J. Qi, *Adv. Funct. Mater.*, **2019**,*29 (2)*, 1805290.

[138] A.Selimis, V. Mironov, M. Farsari, *Microelectron. Eng.*, **2015**, *132*, 83–89.

[139] S. Juodkazis, V. Mizeikis, H. Misawa, *J. Appl. Phys.*, **2009**, *106* (*5*), 051101.

[140] M. Farsari, M. Vamvakaki, B.N.Chichkov, *J. Opt.*,**2010**, **12** (12), 124001.

[141] I. Bernardeschi, M. Ilyas, L. Beccai, *Adv. Intell. Syst.*, **2021**, *3 (9)*, 2100051.

[142] C. Ohm, E.-K. Fleischmann, I. Kraus,C. Serra, R. Zentel, *Adv. Funct. Mater.*, **2010**, *20* (*24*), 4314–4322.

[143] C.M.B. Ho, S.H. Ng, K.H.H. Li, Y.-J. Yoon, *Lab. Chip*, **2015,** *15* (18), 3627–3637.

[144] B. Zhou, W. Xu, A.A. Syed, Y. Chau, L. Chen, B. Chew, O. Yassine, X. Wu, Y. Gao, J. Zhang, X. Xiao, J. Kosel, X.-X. Zhang, Z. Yao, W. Wen, *Lab. Chip*, **2015,** *15* (*9*), 2125–2132.

[145] S. Nocentini, D. Martella, C. Parmeggiani, D.S. Wiersma, *Adv. Opt. Mater.*, **2018**, *7* (*16*), 1900156.

[146] Z. Liu, M. Li, X. Dong, Z. Ren, W. Hu, M. Sitti, *Nat. Commun.*, **2022**, *13* (*1*), 2016.

[147] M.J. Villangca, D. Palima, A.R. Bañas, J. Glückstad, *Light Sci. Appl.*,**2016**, *5* (*9*), e16148–e16148.

[148] C. Maggi, F. Saglimbeni, M. Dipalo, F. De Angelis, R. Di Leonardo, *Nat. Commun.*, **2015,** 6 (1), 7855.

[149] M. López-Valdeolivas, D. Liu, D.J. Broer, C. Sánchez-Somolinos, *Macromol. Rapid Commun.*,**2018,** *39* (*5*), 1700710.

[150] A. Sydney Gladman, E.A. Matsumoto, R.G. Nuzzo, L. Mahadevan, J.A. Lewis, *Nat. Mater.*, **2016,** *15* (*4*), 413–418.

[151] C.A. Spiegel, M. Hippler, A. Münchinger, M. Bastmeyer, C. Barner-Kowollik, M. Wegener, E. Blasco, *Adv. Funct. Mater.*, **2020**, 30 (*26*), 1907615.

[152] N.Anscombe, *Nat. Photonics*, **2010,** *4* (*1*), 22–23.

[153] A. Selimis, V.Mironov, M.Farsari, *Microelectron. Eng.*, **2015,** *132*, 83–89.

[154] J. Song, C. Michas, C.S. Chen, A.E. White, M.W. Grinstaff, *Macromol. Biosci.*, **2021**, 21 (*5*), 2100051.

[155] J. Song, C. Michas, C.S. Chen, A.E. White, M.W. Grinstaff, *Adv. Healthc. Mater.*, **2020**, *9* (*1*), 1901217.

[156] T. Spratte, S. Geiger, F. Colombo, A. Mishra, M. Taale, L. Hsu, E. Blasco, C. Selhuber-Unkel, *Adv. Mater. Technol.*, **2023**, *8* (*1*), 2200714.

[157] M. Hippler, E. Blasco, J. Qu, M. Tanaka, C. Barner-Kowollik, M. Wegener, M. Bastmeyer *Nat. Commun.*, **2019,** *10* (*1*), 232.

[158] A. Ennis, D. Nicdao, S. Kolagatla, L. Dowling, Y. Tskhe, A.J. Thompson, D. Trimble, C. Delaney, L. Florea, *Adv. Funct. Mater.*, **2023,** 2213947.

[159] J. Qian, S. Kolagatla, A. Pacalovas, X. Zhang, L. Florea, A.L. Bradley, C. Delaney, *Adv. Funct. Mater.*, **2023**, 2211735.

[160] M. Del Pozo, J.A.H.P. Sol, A.P.H.J. Schenning, M.G. Debije, *Adv. Mater.*, **2022**, *34 (3)*, 2104390.

[161] A. Kotikian, R.L. Truby, J.W. Boley, T.J. White, J.A. Lewis, *Adv. Mater.*,**2018**, *30 (10)*, 1706164.

[162] K.M. Herbert, H.E. Fowler, J.M. McCracken, K.R. Schlafmann, J.A. Koch, T.J. White, *Nat. Rev. Mater.*, **2021**, *7* (*1*), 23–38.

[163] D. Martella, S. Nocentini, D. Nuzhdin, C. Parmeggiani, D.S. Wiersma, *Adv. Mater.*, **2017**, *29* (*42*), 1704047.

[164] S. Palagi, A.G. Mark, S.Y. Reigh, K. Melde, T. Qiu, H. Zeng, C. Parmeggiani, D. Martella, A. Sanchez-Castillo, N. Kapernaum, F. Giesselmann, D.S. Wiersma, E. Lauga, P. Fischer, *Nat. Mater.*, **2016**,*15 (6)*, 647–653.

[165] S. Nocentini, D. Martella, C. Parmeggiani, S. Zanotto, D.S. Wiersma, *Adv. Opt. Mater.*, **2018,** *6* (*15*), 1800167.

[166] I. De Bellis, D. Martella, C. Parmeggiani, D.S. Wiersma, S. Nocentini, *Adv. Funct. Mater.*, **2023**, 2213162.

[167] A. Münchinger, L.-Y. Hsu, F. Fürniß, E. Blasco, M. Wegener, *Mater. Today*, **2022**, *59*, 9–17.

[168] I. De Bellis, S. Nocentini, M.G. Delli Santi, D. Martella, C. Parmeggiani, S. Zanotto, D.S. Wiersma, *Laser Photonics Rev.*, **2021**, *15* (*8*), 2100090.

[169] M.Del Pozo, C. Delaney, C.W.M. Bastiaansen, D. Diamond, A.P.H.J. Schenning, L. Florea, *ACS Nano*, **2020,** *14* (*8*), 9832–9839.

[170] T. Ritacco, D.M. Aceti, G. De Domenico, M. Giocondo, A. Mazzulla, G. Cipparrone, P. Pagliusi, *Adv. Opt. Mater.*, **2022**, *10* (*2*), 2101526.

[171] I. De Bellis, D. Martella, C. Parmeggiani, D.S. Wiersma, S. Nocentini, *Adv. Funct. Mater.*, **2023**, 2213162.

[172] S. Donato, D. Martella, M. Salzano De Luna, G. Arecchi, S. Querceto, C. Ferrantini, L. Sacconi, P. Brient, C. Chatard, A. Graillot, D.S. Wiersma, C. Parmeggiani, *Macromol. Rapid Commun.*, **2023**, *44* (*9*), 2200958.

[173] S. Nocentini, D. Martella, C. Parmeggiani, D.S.Wiersma, *Materials*, **2016**, *9* (*7*), 525.A. Grushina, *Adv. Opt. Technol.*, **2019**, *8* (*3–4*), 163–169.

[174] J. Wang, F. Jin, X. Dong, J. Liu, M. Zhou, T. Li, M. Zheng, *Small*, **2023**, 2303166.

[175] G. Decroly, A. Chafaï, G. De Timary, G. Gandolfo, A. Delchambre, P. Lambert, *Adv. Intell. Syst.*, **2023**, 2200394.

[176] Z. Wang, *ACS Nano*, **2023,** *17* (*11*), 10078–10089.

[177] J. Li, R. Liu, H. Lin, S. Ye, M. Ye, X. Wang, X. Zhu, X. *ACS Appl. Mater. Interfaces*, **2021**, *13* (*51*), 61536–61543.

[178] Z. Lao, R. Sun, D. Jin, Z. Ren, C. Xin, Y. Zhang, S. Jiang, Y. Zhang, L. Zhang, *Int. J. Extreme Manuf.*, **2021**, *3* (*2*), 025001.

[179] L. Dong, Y. Zhao, *Mater. Chem. Front.*, **2018**, *2* (*11*), 1932–1943.

[180] D. Martella, S. Nocentini, F. Micheletti, D.S. Wiersma, C. Parmeggiani, *Soft Matter*, **2019**, *15* (*6*), 1312–1318.

[181] Y. Guo, H. Shahsavan, M. Sitti, *Adv. Opt. Mater.*, **2020**, *8* (*17*), 1902098.

[182] W. Hong, Z. Yuan, X. Chen, *Small*, **2020**, *16* (*16*), 1907626.

[183] L. Bai, Z. Xie, W. Wang, C. Yuan, Y. Zhao, Z. Mu, Q. Zhong, Z. Gu, *ACS Nano*, **2014**, *8* (*11*), 11094–11100.

[184] H. Zhang, Q. Li, Y. Yang, X. Ji, J.L. Sessler, J.L. *J. Am. Chem. Soc.*, **2021,** *143* (*44*), 18635–18642.